Laura Resch, BSc

Positronium formation on thin layers and laser excitation of positronium

MASTER THESIS

for obtaining the academic degree

Diplom-Ingenieur

Master Programme of Technical Physics

Graz University of Technology

Supervisor:

Univ.-Prof. Dipl.-Phys. Dr.rer.nat. Roland Würschum

Institute of Materials Physics
in cooperation with AEḡIS (Antimatter experiment), CERN

Graz, September 2016

EIDESSTATTLICHE ERKLÄRUNG

AFFIDAVIT

Ich erkläre an Eides statt, dass ich die vorliegende Arbeit selbstständig verfasst, andere als die angegebenen Quellen/Hilfsmittel nicht benutzt, und die den benutzten Quellen wörtlich und inhaltlich entnommenen Stellen als solche kenntlich gemacht habe. Das in TUGRAZonline hochgeladene Textdokument ist mit der vorliegenden Masterarbeit/Diplomarbeit/Dissertation identisch.

I declare that I have authored this thesis independently, that I have not used other than the declared sources/resources, and that I have explicitly indicated all material which has been quoted either literally or by content from the sources used. The text document uploaded to TUGRAZonline is identical to the present master's thesis/diploma thesis/doctoral dissertation.

23.6.2016
_____
Datum / Date

_____
Unterschrift / Signature

ACKNOWLEDGMENTS

ABSTRACT

Positrons (the antiparticles of electrons) and positronium (the bound state of a positron and an electron) are of interest for fundamental experiments as well as for material characterization. In this thesis both aspects have been investigated. The majority of the presented measurements were conducted within the AEḡIS (Antimatter Experiment: Gravitation, Interferometry, Spectroscopy) collaboration, placed at CERN. The goal of the experiment is to directly measure the effect of the earth's gravitational field on antimatter. To perform this measurement, neutral antihydrogen atoms are an essential component. Antihydrogen will be produced via a charge exchange reaction with Rydberg positronium, which is one of the topics of this thesis.

Within this work, the formation of positronium (Ps) on a p-type(111)-sample, as well as its laser excitation to the n=3 state and subsequently to Rydberg states could be shown, using Single Shot Positron Annihilation Lifetime Spectroscopy (SSPALS). The efficient excitation was monitored via magnetic quenching and photoionization by a IR-pulse (λ_{IR}=1064 nm). For the excitation to the n=3 state, a UV-laser with a wavelength of 205.045 nm was used. The fraction S of excited Ps, for the case of photoionization, was determined to (15.5±1.3)%, while it was only (3.6±1.2)% for magnetic quenching. Consequently, photoionization could be verified as the more effective tool with respect to the detection of Ps excitation.
By varying the UV-wavelength and measuring the corresponding SSPALS spectra, the Doppler broadened linewidth of the transition could be obtained. Thereof the velocity of Ps parallel to the direction of the laser pulse could be found to $\approx 10^5$ m/s.
Positronium excitation to n=3 was independently demonstrated by the production of Ps in Rydberg states via a two-step transition. After excitation to n=3, an IR pulse tunable between 1684-1708 nm (corresponding to the energy levels n=15-17) was used to populate Rydberg levels. The n=15 and n=16 transitions

were clearly distinguishable.

In addition to the work directly related to the AEḡIS experiment, material investigations of carbon particle filters, provided by the company AVL (Anstalt für Verbrennungskraftmaschinen List), were carried out. The samples were examined by the means of Positron Annihilation Spectroscopy at the VEPAS laboratory of Como, a member of the AEḡIS collaboration. Two sets of samples, microstructured nickel and quartz tissue filters, differing in their carbon nanoparticle loadings, were measured via Doppler Broadening and Positronium Formation Spectroscopy.

The data was fitted and analyzed using VEPFIT, a software specially designed for the issues of Positron Annihilation Spectroscopy. In the case of the nickel filter, the thickness of the carbon layer could be calculated to (620 ± 2) nm. Further the positronium formation measurements led to the assumption of carbon nanoparticles diffusing deeply into the sample. The Doppler Broadening Spectroscopy of the quartz tissue filter samples clearly showed the existence of two different layers where the positrons annihilate. The thickness and the density of the first layer and the second layer have been estimated through the fit for all samples.

ZUSAMMENFASSUNG

Positronen (die Antiteilchen von Elektronen) sowie Positronium (der gebundene Zustand eines Elektrons und eines Positrons) spielen nicht nur in der Grundlagenforschung eine wichtige Rolle, sondern können auch zur Charakterisierung von Materialien eingesetzt werden. In der folgenden Masterarbeit wurden beide Aspekte behandelt.

Ein Großteil der präsentierten Messungen erfolgte am CERN im Rahmen der AEḡIS (Antimatter Experiment: Gravitation, Interferometrie, Spektroskopie) Kollaboration. Ziel des Experiments ist es, die Wirkung des Erdgravitationsfeldes auf Antimaterie zu messen. Ein essentieller Bestandteil des Versuchs sind neutrale Antiwasserstoffatome. Diese werden innerhalb einer Ladungsaustausch-Reaktion mit Rydberg-Positronium erzeugt.

Im Rahmen der vorliegenden Arbeit am AEḡIS Experiment wurde mit Hilfe von Single Shot Positron Annihilation Lifetime Spectroscopy (SSPALS) die Produktion von Positronium (Ps) an einem p-Si(111)-Target gezeigt. Das erzeugte Ps wurde durch einen UV-Laser (λ_{UV}=205.045 nm) zum Zustand n=3 angeregt. Dieser Übergang wurde anhand von Quenching im Magnetfeld sowie Photoionisation durch einen geeigneten IR-Laserpuls (λ_{IR}=1064 nm) beobachtet. Durch Photoionisation konnte ein Ps-Anteil S=(15.5±1.3)% angeregt werden. Im Fall von Quenching betrug S nur (3.6±1.2)%. Aufgrund dieser Messergebnisse konnte Photoionisation als die effektivere Methode zur Beobachtung der Laseranregung verifiziert werden.

Durch Variation der UV-Wellenlänge und Analyse der zugehörigen SSPALS-Spektren wurde außerdem die dopplerverbreiterte Anregungslinie zum Zustand n=3 gemessen. Daraus konnte die Geschwindigkeit von Ps parallel zur Einstrahlrichtung des Lasers zu $\approx 10^5$ m/s bestimmt werden.

Weiters konnte die Anregung zu n=3 durch die Produktion von Rydberg Ps über einen Zwischenschritt gezeigt werden. Nach dem Übergang zu n=3 wurde ein

zwischen 1684-1708 nm (entsprechend der Energieniveaus n=15-17) variierbarer IR-Laserpuls verwendet, um Rydberg Niveaus zu besetzen. Dabei waren die Anregungen zu n=15 und n=16 klar zu erkennen.

Zusätzlich zu diesen Messungen am AEḡIS Versuchsaufbau wurden Russpartikelfilter, die von der Firma AVL (Anstalt für Verbrennungskraftmaschinen List) zur Verfügung gestellt wurden, mittels Positronenannihilationsspektroskopie charakterisiert. Die Proben wurden am VEPAS Labor in Como, einem Mitglied der AEḡIS Kollaboration, durch Dopplerverbreiterungs- und Positroniumformationsspektroskopie vermessen. Untersucht wurden mehrere Exemplare zweier Filtertypen, einerseits mikrostrukturiertes Nickel, andererseits Quartzgewebe. Allesamt unterschieden sich diese durch verschiedene Beladungen an Russpartikeln.

Die Daten wurden durch die Software VEPFIT, die speziell für die Anforderungen im Bereich der Positronenspektroskopie entwickelt wurde, gefittet und weitergehend analysiert. Die Dicke der Carbonschicht der Nickelprobe konnte zu (620±2) nm bestimmt werden. Außerdem führten die Ergebnisse der Positroniumformationsspektroskopie zu der Schlussfolgerung, dass die Carbonnanopartikel weit in die Probe hineindiffundieren. Im Fall der Quartzfilter sind zwei Umgebungen, in denen die Positronen annihilieren, anhand der Messergebnisse erkennbar. Durch Fits der Datenpunkte konnte die Dichte und die Dicke der ersten Schicht abgeschätzt werden.

CONTENTS

THEORETICAL PART

FUNDAMENTALS

1.1 ANTIMATTER

In 1928 the existence of antimatter was first predicted by Dirac's equation as an interpretation of the negative energy eigenvalues for particles at rest[1]. In 1932 Carl David Anderson saw a track, left by "something positively charged, and with the same mass as an electron", while studying showers of cosmic particles in a cloud chamber. The outcome of these results was the experimental proof for the existence of positrons[2].

Figure 1 shows a timeline indicating important steps in antimatter research: In 1955 and 1956, the antiproton and the antineutron were discovered at the Bevatron in Berkeley, California. In the following years antimatter has been efficiently stored and produced. In 2011, the ALPHA experiment at CERN stored Antihydrogen for 1000 seconds[3]. Very recently, in 2015, the charge-to-mass ratio of the antiproton was measured by the CERN BASE experiment with a precision of 69 parts per trillion[4].
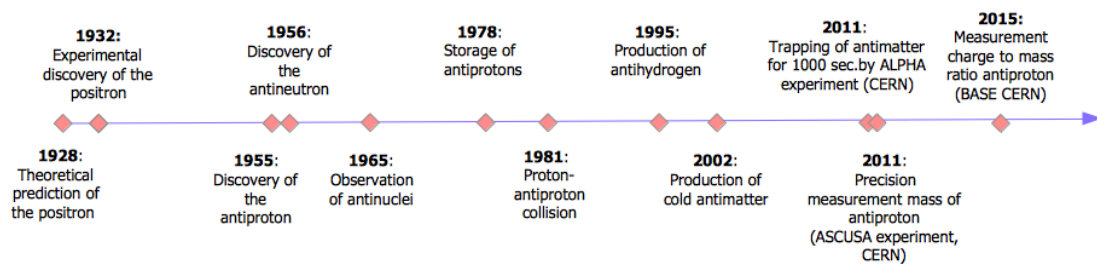
Figure 1: Timeline: Important steps in antimatter research

1.2   POSITRON

The positron e^+ is a fermionic, elementary particle and the anti-particle of the electron. It has the same spin and, within experimental limits, the same mass as the electron, while its charge and magnetic moment is the opposite.

Although the positron is stable in vacuum, in contact with matter it rapidly looses its kinetic energy until it is near thermal energy ($\approx$10 ps) and annihilates with electrons. [5] When an annihilation of a positron and an electron at rest occurs, two γ-rays are sent out in opposite directions, at an angle of 180°, each carrying an energy of $mc^2 = 511$ keV, where m is the rest mass of the electron and c refers to the speed of light:

$$e^+ + e^- \longrightarrow 2\gamma \tag{1}$$

1.3   POSITRONIUM (PS)

Positronium is the bound state of a positron and an electron, kept together by electromagnetic interaction. Ps has a binding energy of E_b=6.8 eV, and is considered as a semi-stable system because it only exists for parts of microseconds until the antiparticle pair annihilates.

Depending on the spins of the electron and the positron, positronium can exist in two states (see table 1). Ortho-Positronium (o-Ps) refers to the spin triplet state. The spins of the two particles are parallel and the total spin is 1. The lifetime of o-Ps is 142 nanoseconds. When forming para-Positronium (p-Ps) the spins of the electron and the positron are antiparallel, with a total spin of zero and a lifetime of 125 picoseconds. The ratio between the amounts of o-Ps and p-Ps produced during Ps-formation is 1:3 for kinematical reasons. While p-Ps decays into 2 γ-rays, each with an energy of 511 keV, o-Ps decays into 3 γ-rays (due to the conservation of angular momentum) with a total energy of 2× 511 keV [6].

Table 1: Ortho- & Parapositronium characteristics

type	spins	total spin	lifetime	annihilation
o-Ps	$\uparrow\uparrow, \downarrow\downarrow$	1	142 nsec.	3 γ-rays
p-Ps	$\uparrow\downarrow, \downarrow\uparrow$	0	125 psec.	2 γ-rays

1.4 POSITRON SOURCES

Positrons can either be produced by pair production, where high energy photons are converted into electron-positron pairs, or as a product of radioactive decay. Positrons emerge in β^+-decays, where a proton decays into a neutron, an electronneutrino and a positron.

Commonly used radioactive sources are ^{22}Na , ^{58}Co or ^{64}Cu. The source-isotope used in the AEḡIS apparatus is ^{22}Na, as it is in most laboratories. It has a half-life of 2.6 years and decays to the excited state (^{22}Ne*) of ^{22}Ne by β^+-decay. ^{22}Ne* relaxes into the ground state sending out a γ-ray carrying an energy of 1.27 MeV [7] :

$$^{22}\text{Na} \longrightarrow ^{22}\text{Ne}^* + \beta^+ + \nu_e \tag{2}$$

$$^{22}\text{Ne}^* \longrightarrow ^{22}\text{Ne} + \gamma \tag{3}$$
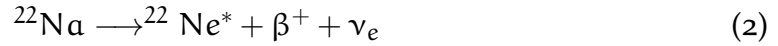
To preserve the charge balance when a proton decays into a neutron, a positron is emitted. ^{22}Na shows a branching ratio of 0.906 for positrons, which means that positrons are emitted in 90.6% of all decay events. Positrons emitted by radioactive sources show a relatively broad, continuous energy distribution ranging from 0-543 keV.

1.5 MODERATOR

The broad energy distribution of positrons, emitted by a radioactive source, makes any kind of beam guidance for positrons impossible. One had to think of a way to change the various energies of an ensemble of positrons to a defined energy range. This is a process referred to as moderation of positrons.

For most materials, the reason for their behaviour as moderators lies in their negative positron work function ϕ^+, which is defined as: [6]

$$\phi^+ = -D - \mu^+ \qquad (4)$$

The electron work function on the other hand is defined as:

$$\phi- = D - \mu^- \qquad (5)$$

Here D refers to the dipole barrier of the material. It is the change of potential energy across the surface dipole, arising from electrons spilling over the solids border into the vacuum. μ^+ (μ^-) is the chemical potential of the positron (electron). μ^+ is given by the difference in potential of the crystal zero, defined as mean electrostatic potential of the interstitial regions between the atoms, and the lowest positron energy state in the crystal. The chemical potential of the electron, μ^-, is defined as the difference in energy between the crystal zero and the Fermi level.
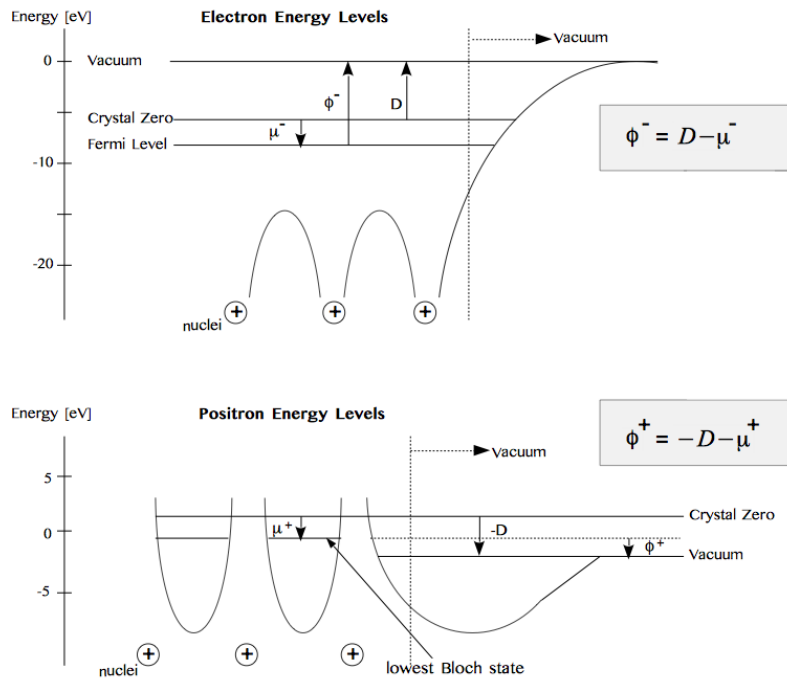
Figure 2: Schematic drawing of the energy levels of electrons and positrons within a solid, indicating the calculation of the electron and positron work function. For electrons, the work function is defined as the energy required to remove an electron from the highest possible energy state in the crystal, the Fermi level, to the vaccum. Here the dipole barrier D acts as a barrier in energy, which has to be overcome when removing the electron from the solid.

For the positron energy levels, the drawing indicates the case of a negative e^+ work function ϕ^+. D, the difference between the crystal zero and the vacuum energy level, is negative. As a result ϕ^+ is negative and positrons tend to leave the solid.

For electrons the dipole barrier causes an increase of the work function and thus binds the electrons more tightly to the surface. But as positrons are reverse in charge, the dipole contribution has the opposite effect. For this reason the electron work function can only be positive, while the positron work function can either be positive or negative.

In the latter case, positrons are emitted spontaneously, preferentially perpendicular to the surface due to the momentum they gain by the negative work function. Typical materials that are used as moderators are for example Tungsten or Copper. They both deliver very sharp energy distributions of δE=0.1 eV, but their efficiencies (defined by the ratio of slow e^+ escaping from the moderator and fast e^+ coming from the source) of 0.3% and 0.1% are rather small, respectively.

The moderator used in AEḡIS consists of solid Neon. A material that, at first glance, seems inappropriate as a moderator, due to its positive work function. However, rare gas solids such as neon, argon or krypton, which all show small

but positive positron work functions, have been shown to be very effective moderators.

This can be explained as follows. Positrons which enter a material are loosing their energy quickly due to inelastic collisions involving electronic transitions. In an insulator, such as neon, once the positron energy is less than the band gap, it can only continue loosing its energy by phonon scattering in small fractions. Like this, the diffusion length is large and it becomes more likely that positrons reach the surface before their energy falls below the positron work function. Thus a larger fraction of positrons can escape. Solid neon shows an efficiency of 0.7%, which is the highest quoted, but compared to tungsten and copper also exhibits a rather large energy spread δE of 0.58 eV. [8] [9]

1.6 POSITRON TRAPPING

For some experiments, as AEḡIS, far higher positron fluxes than those achieved by a simple source-moderator set-up are required. If the beam does not neccessarily have to be continuous, intense positron bunches can be accomplished by the stacking and accumulating of positrons in electro-magnetic traps. Positrons from the source are collected and stored, and after a certain amount of time, released in one bunch.

1.6.1 Surko trap

Figure 3 shows schematically the set-up and components of a so-called Surko trap. The five ring electrodes (E1-E5) confine the positrons axially, a homogeneous translational magnetic field ensures radial confinement[10].

In comparison to other traps such as the Penning-Malmberg trap[11], the group of Surko et. al. was the first to additionally make use of buffer gases within the traps in order to cool the positrons[10].

Positrons entering the trap are attracted by the potential well created by E1-E4 and gain kinetic energy until they reach electrode E5, where they are reflected back due to its higher potential.

For storing of positrons, electrode potential E3 is raised, thus positrons are trapped between E3 and E5. In the last step the positrons are dumped by lowering the potential of electrode E5 below the potential of electrode E4.

By introducing a buffer gas to the trap the amount of storeable positrons can be enhanced significantly. Positrons between the electrodes E3 and E5 are thermalized by collisions with the gas molecules. In this manner, their energy is not sufficient anymore to overcome the potential of the entrance electrodes and they cannot leave the trap after being reflected back by E5.
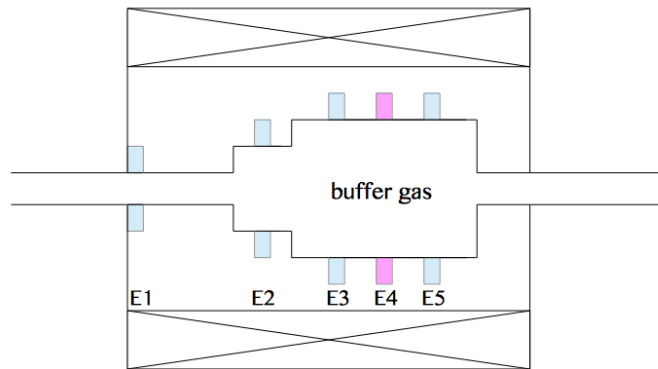
Figure 3: Schematic sketch of the set-up of a surko trap: Electrodes E1-E5 enable axial confinement while the magnetic field confines the positrons radially. The potentials of E1-E5 are variable and are changed for the different phases. Positrons are first guided into the trap by attractive potentials, then stored between E3 and E5 and cooled by the buffer gas and finally released again by lowering E5.

Possible cooling gases are for example N_2 or CO_2, both fullfill the essential condition that the time required for the thermalization of positrons has to be significantly shorter than the lifetime of the positrons in the gas. N_2 is used for first cooling at high energies (E>8.6 eV) because positrons loose their energy mainly due to electronic excitations[12]. CO_2 is used to cool down further (8.6 eV>E>0.05 eV). Here positrons loose smaller fractions of energy due to rotational and vibrational excitations[13].

1.6.2 *Rotating wall*

Inhomogenities and asymmetries of the electric and magnetic fields of the trap lead to an undesirable expansion of the positron plasma and consequently to a decrease of lifetime through annihilations with the walls[14].

Through an additional 'rotating wall' at the central electrode of the trap (as it is highlighted in a different colour in figure 3), positrons can be forced to stay in the center as a compressed cloud. The central electrode is divided into four parts, on each of which a sinusoidal voltage is applied. They are phase-shifted by $90°$ with respect to each other.

In this manner positrons see a perfectly rotating electric field and are thus forced to move inwards. By the compression, they also gain some kinetic energy and thus heat up, but already small amounts of buffer gas are enough to cancel out the heating.

A positron plasma in a magnetic field typically rotates around the axis of the field with a frequency f_E, proportional to the density n_P of the plasma, and indirectly proportional to the applied magnetic field B [15]:

$$f_E = \frac{n_P e}{4\pi\varepsilon_0 B},$$ (6)

where e is the elementary charge and ε_0 the electric constant.

Normally there is no linear relation between the frequency of the positron plasma f_E, and the frequency of the rotating wall f_{RW}. Recently it has been proven[16], that there is a certain regime, the so-called strong-drive regime, where the positron plasma frequency f_E, and the frequency of the rotating wall are directly related, so that $f_E = f_{RW}$. In this regime, where the internal potential of the plasma is in equilibrium with the magnetic field, the density of the positron plasma can be defined by the frequency of the rotating wall f_{RW}.

1.7 TECHNIQUES FOR THE CHARACTERIZATION OF POSITRON BEAMS

Several types of detectors can be used to trace trajectories, track down critical points in the system, where positrons are lost, or to characterize the positron beam spot.

Scintillators and semiconductors gather the positron signal indirectly by the detection of the annihilation γ-quants. The multi channel plate and phosphor screen assembly visualizes the positron beam by the conversion of positrons into electrons and in a second step electrons into photons in the visible range. [17]

1.7.1 *Scintillators*

The principle of scintillators for the detection of γ-rays is the conversion of the incoming high energy γ-quants into visible light, i.e. photons of a few electronvolts in energy. In principle, scintillators can be divided into organic and inorganic materials.

In organic scintillators, scintillation occurs via transitions between the molecular states, whereas in inorganic crystals scintillation appears due to interband transitions.

Inorganic materials, used as scinitillators, are crystals such as for example sodium iodide (NaI), caesium iodide (CsI) or lead tungstate ($PbWO_4$). They show high quantum efficiencies, nearly every incoming γ-ray results in many emitted photons. Typical decay times are in the range of several hundred nanoseconds.

Compared to typical plastic scintillators with operating times of a few nanoseconds, crystals respond quite slowly. On the other hand, plastic scintillators show low quantum efficiencies compared to inorganic crystals due to their low density[18].

In order to convert photons into electrons, scintillators are coupled to photodiodes or photomultiplier tubes for a conversion and amplification of the signal.

Incoming photons produce a current in the p-n-junction of the photodiode, which is restricted by a resistor and a capacitor. Due to that, a slowly decreasing signal occurs, even if the annihilation signal itself has only a very short time spread. Consequently, the temporal length of these signals only give a statement about the detector characteristics, not about the actually detected signal.

A valuable information about the annihilation signal gives the amplitude of the voltage. It is directly proportional to the number of incoming photons.

A photomultiplier tube consists of a photocathode, where photons cause the release of electrons from the material by the photoelectric effect. Subsequently the photoelectrons are accelerated in an electric field and hit several dynodes where they produce secondary electrons. In the last step a large number of electrons reaches an anode where they produce a sharp, easily detectable current pulse.

1.7.2 *Semiconductors*

Semiconductor detectors are basically reverse-biased diodes. If a γ-ray hits the material, it produces a number of electron-hole-pairs, proportional to the energy of the incoming photon. Those, being seperated by the electrical field, produce a detectable current pulse.

To reach maximum detection efficiency when it comes to γ-rays, materials with high atomic number such as Germanium are used. Intrinsic germanium has an empty conduction band at low temperatures. Absorbed photons induce a transition of electrons from the valence to the conduction band. In order to carry and store these excited electrons, a potential in the order of keV is applied to the germanium heads.

The main advantage of Germanium detectors is their excellent energy resolution which can be used for γ-ray spectroscopy. Disadventegous is that they have to be cooled with liquid nitrogen (77 K). Due to the low band gap of Ge, without cooling, charge carriers would be generated thermally. This would lead to leakage current-induced noise that destroys the energy resolution of the detector.

1.7.3 *Multi Channel Plate & Phosphor Screen*

An assembly consisting of a multi channel plate and a phosphor screen can be used to characterize the geometry and intensity of positron beams.

Multi channel plates are set up from many channeltrons. These are angled channels of a few μm in diameter, made from a high resistivity material, that releases electrons when hit by energetic photons or charged particles, such as positrons.

The electrons are accelerated towards the end of the channel by an applied voltage. Induced by the angled geometry of the channels, the electrons hit the walls several times before they reach the end and thus the signal is amplified by the production of secondary electrons. In the last step, a large number of secondary electrons hits a phosphor screen. The material of the screen gets excited and emitts light that can be monitored by a camera.

1.8 INTERACTIONS OF POSITRONS WITH SOLIDS

Figure 4 shows schematically the interaction of a positron beam ($E \leqslant 100$ keV) with the near-surface region of a solid. The various processes are put in order according to their time scales.

As the beam first encounters the surface, within the time interval $0 \lesssim t \lesssim 10^{-15}$ sec., it can either enter the solid or be reflected back. With an increasing atomic number of the material, the probabilty of a reflection of the beam gets higher. A material used as a positron reflector would for example be the high Z metal tantalum. It is possible, that positrons which enter the material may pass the specimen by channeling, although the probability of this process decreases with increasing thickness of the sample and lower energy of the beam. Otherwise the positrons can lose parts of their kinetic energy through core excitations. Secondary electrons can leave the material as a result of the interaction with the positron beam. During the process of equilibration ($0 \lesssim t \lesssim 10^{-12}$ sec.), positrons continuously loose energy through the excitation of plasmons, electron-hole pairs and phonons. Some of the faster, non-thermal positrons can reach the surface. They either leave the material again as positrons or bind with an electron and leave as fast positronium.

(1) First encounter: $0 \leq T \leq 10^{-15}\, sec$

Energy loss:
-core excitation

Scattering
Diffraction

e^+ beam

Channeling

Secondary electrons

(2) Attaining equilibrium: $0 \leq T \leq 10^{-12}\, sec$

Energy loss:
-plasmons
-electron/hole pairs
-phonons

e^+ beam

fast $\Big\{$ Ps* Ps$^-$ Ps e^+

(3a) Equilibrium: $0 \leq T \leq 10^{-10}\, sec$

γ_1

Diffusion

Surface e^+

e^+ beam

$e^+ e^-$ annihilation
Trapped annihilation

Energetic Ps
Slow e^+

γ_2

(3b) Longer Times: $0 \leq T \leq 10^{-7}\, sec$

γ_1

Diffusion

Surface
annihilation

e^+ beam

Slow e^+

γ_3

o-Ps decay

γ_2

γ_1

γ_2

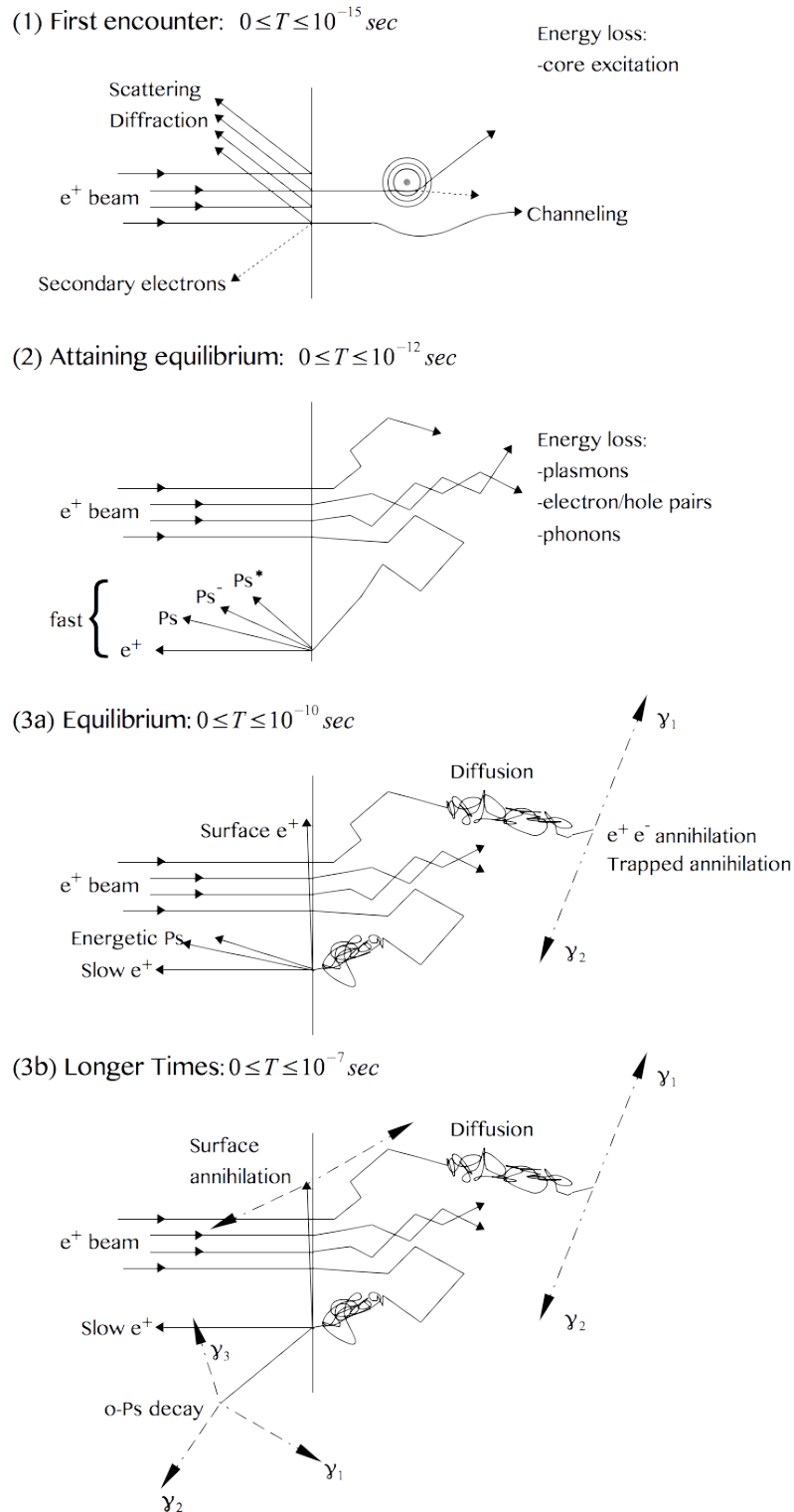Figure 4: Interaction of a positron beam with the near-surface region of a solid, in the sequence of the corresponding time scales. At first encounter (1), positrons are either reflected back or enter the material. Once they enter, they attain equilibrium (2) through the excitation of plasmons, electron-hole pairs or phonons. At equilibrium (3a,b) positrons start diffusing around within the solid and at some point annihilate.

Once the positrons reached equilibrium (approximately $0 \lesssim t \lesssim 10^{-10}$ sec.) they start diffusing through the solid. While some of the positrons annihilate with an electron instantly, other positrons get trapped in vacancies before they annihilate and send out two γ-quants. A part of the positrons may diffuse to the surface and leave as slow positrons or energetic surface-formed Ps.

Within longer time scales ($0 \lesssim t \lesssim 10^{-7}$ sec.) following events can be observed: o-Ps annihilates into three γ-quants outside the sample. Another process that can be observed within this time frame is the annihilation of surface positrons with electrons. [6]

The movement of thermalized positrons through a solid can be described classically as diffusion, with the correspoding diffusion equation in one dimension[19]:

$$\frac{\partial n(z,t)}{\partial t} = P(z,E) - [\lambda_b + k(z)]n(z,t) - \frac{\partial J}{\partial z} \tag{7}$$

In formula 7 n(z,t) refers to the probability density of finding a positron at the depth z at the time t and P(z,E) is the positron implantation profile.

The term $[\lambda_b + k(z)]n(z,t)$ takes into account positrons that either annihilate or get trapped in open volume defects, with λ_b, the e^+ annihilation rate and k(z) the trapping rate in open volume defects. J refers to the flux of positrons, created by positrons diffusing further or back the defined depth region.

The positron implantation profile, P(z,E), can be described by a so-called Makhov profile:

$$P(z,E) = \frac{mz^{m-1}}{z_0^m} exp\{-(\frac{z}{z_0})^m\} \tag{8}$$

with

$$z_0 = \frac{AE^r}{\rho\Gamma(1+\frac{1}{m})} \tag{9}$$

The mean positron implantation depth $\bar{z}$ is described by the following formula:

$$\bar{z} = \frac{A}{\rho} E^r \tag{10}$$

In formulas 8,9 and 10 ρ refers to the mass density of the material $[gcm^{-3}]$ and Γ is the Gamma function. m and r are dimensionless empirical parameters. A is an empirical parameter $[\mu gcm^{-2}keV^{-r}]$. m, r and A can be obtained theoretically using Monte Carlo simulations, widely used values are A=4.0 $\mu gcm^{-2}keV^{-r}$, m=2, r=1.6[20].
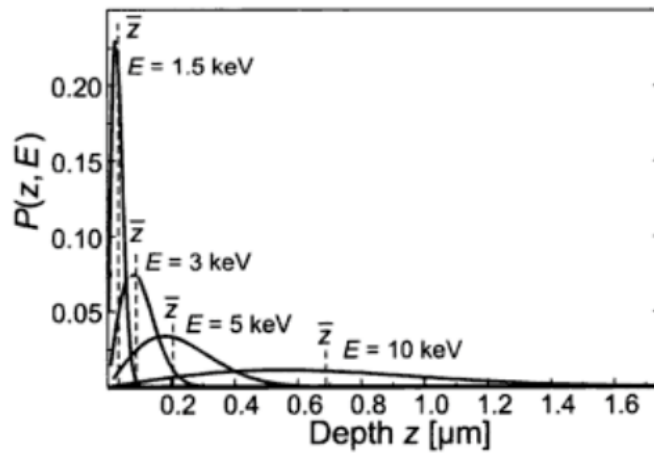
Figure 5: Makhov profiles for different positron implantation energies. Parameters used: A=4.0 $\mu gcm^{-2}keV^{-r}$, m=2, r=1.6. $\bar{z}$ indicates the mean penetration depth. Picture taken from [21].

As it can be seen in figure 5 the positron implantation profile gets smeared out for high e^+ implantation energies. Positrons get implanted into broader regions in depth and their localization becomes more difficult.

As it is depicted in figure 4, a possible result of the interaction between a positron and a solid is the formation of positronium. Positronium can be created at the surface by a positron, that diffuses there from the bulk and captures an electron, or Ps can be formed at the bulk of the material, diffuse to the surface and leave as Ps, if its energy is sufficient.

1.9.1 *Bulk formation*

Within the bulk of a material, it is, in terms of energy, more favorable for an electron and a positron to form positronium than to stay seperated.

The Ps atom diffuses through the material and, if it reaches the surface with sufficient energy, it can be emitted.

Similar to the positron work function, a Ps work function can be defined as[22]:

$$W_{bulk} = \phi^+ + \phi^- + E_{Ps} - 6.8 \; eV \tag{11}$$

In equation 11, ϕ^+ and ϕ^- refer to the positron and electron work function (as introduced in formulas 4 and 5). E_{Ps} is the binding energy of positronium in the material and 6.8 eV is the formation energy of positronium in vacuum.

If ϕ^+ and ϕ^- as well as E_{Ps} are small enough, the positronium work function can be negative and a Ps atom is emitted with the according energy. If the Ps work function is positive, positronium will not leave the solid at all.

There are two different processes of positronium formation in the bulk.

One is the so-called Ore process. If a hot, not yet thermalized positron, has an energy of a certain range (the Ore energy gap) it can simultaneously ionize a molecule and form Ps.

Positronium can also be formed by thermalized positrons via the Spur process. During its thermalization within the solid, a positron can create ions, electrons, excited molecules and radicals. If one of these, by the positron created electrons, is attracted by the potential of the positron, they can form positronium.

1.9.2 *Surface formation*

In the case of surface formed positronium, the following equation describes the corresponding work function $W_{surface}$[22]:

$$W_{surface} = \phi^+ + \phi^- - 6.8 eV \qquad (12)$$

If $\phi^+ \geqslant 0$ the positron can not exit the surface, still Positronium can be formed if the value ϕ^- allows $W_{surface}$ to be negative. In this case positrons can only leave the surface forming Ps. On the contrary, if a material shows a too negative positron work function ϕ^+, positrons are rather emitted directly without forming Ps.

Surface-formed Ps tends to leave the surface with a high energy in the order of eV. With higher temperatures of the Ps-converter the number of surface formed Ps increases. Positrons trapped at the surface, that already bound an electron, are enabled to overcome the potential barrier by thermal energy. [6] [22]

1.9.3 *Ps formation in metals, insulators and semiconductors[23]*

Due to their different electron densities, metals and insulators favour different processes of Ps formation.

Metals show a high density of delocalized electrons. This fact basically prevents Ps formation in the bulk, because the Coloumb attraction between an electron and the positron is screened by the other electrons. Due to the high number of available surface states within metals, Ps can be created at the surface quite efficiently. Positrons, that are implanted at higher energies have to diffuse back to the surface, where they can bind with an electron. Usually these positrons get trapped in a surface state before they are thermally emitted as Positronium.

Within insulators, due to their lower electron densities, the formation of Ps in the bulk of the material is possible. Because the number of surface states is too low here, Ps is barely created by surface formation.

Within semiconductors, both mechanisms are present, though surface formation is favoured.

Because of their different Ps emission channels, Ps emitted by metals and insula-

tors differs in its temperature. Because of the thermal detrapping within metals, the emitted Ps is basically of the same temperature as the target. The temperature of Ps emitted by insulators is given approximately by W_{bulk}, which is typically in the range of a few eV. If the positron-positronium converter target is kept at low temperatures, the thermal detrapping of metals vanishes, while the Ps emission from the bulk of insulators is still active.

1.10 LASER EXCITATION OF POSITRONIUM

The spectroscopic structure of positronium can be deduced from that of the hydrogen energy levels. Since the reduced mass of Ps is half the electron mass, each energy level E_n^{Ps} is half that of hydrogen according to the following formula[24]:

$$E_n^{Ps} = \frac{\mu_{Ps}}{m_e} Z^2 E_n^{H},\qquad(13)$$

where E_n^{H} is the corresponding energy level of hydrogen, μ_{Ps} is the reduced mass of the positronium atom, m_e is the electron mass and Z is the atomic number. The reduced mass affects also the positronium distance scale which is twice that of hydrogen. [25]

As Positronium is excited to higher states, its lifetime, τ_{Ps}, increases with the third power of the energy level n[26]:

$$\tau_{Ps} = \alpha n^3,\qquad(14)$$

where α is a constant, depending on the reduced mass and the orbital quantum number.

Consequently the lifetime of o-Ps can be enhanced up to milliseconds by exciting it to Rydberg states. These are electronically excited states with quantum numbers of n=10 or even higher. The lifetime of the n=17 Rydberg state of Ps can for example be calculated theoretically to ≈18 μs [27].

Figure 6 shows schematically the energy levels of positronium and two possible ways of excitation to Rydberg states. Both of them use an intermediate step, either
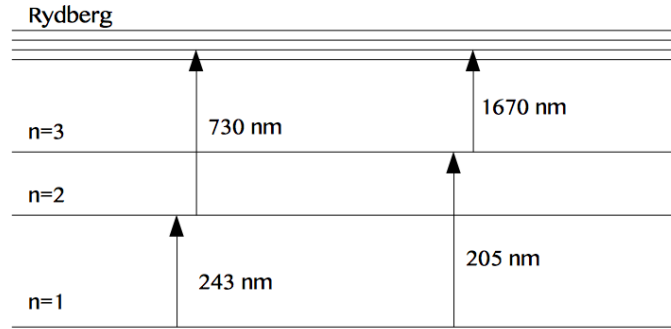
Figure 6: o-Ps energy levels: The arrows indicate two possible ways to excite to Rydberg states, either the n=2 or the n=3 state can be used as an intermediate step.

n=2 or n=3, prior to the excitation to higher levels. The n=2 state of Ps has been investigated intensively before, not only to test theoretical models of Ps but also as the intermediate step towards Rydberg excitation[28] [29].

In the present work the transition to Rydberg states is realized by a first excitation to the n=3 level of o-Ps (3^3P Ps), which is induced by the absorption of a photon starting from the ground state of o-Ps (1^3S Ps). The exact wavelength required for this excitation has been calculated to 205.0474 nm by Castelli[30].

Using n=3 as intermediate step instead of n=2 is expected to bring advantages related to the positronium lifetime as well as the required laser energies. As the n=2 state has a lifetime of only 3 ns, it decays back to the ground state rapidly. Here the n=3 state with its lifetime of about 10.5 ns seems more convenient for the further excitation to Rydberg states. Also the excitation via n=3 requires laser energies of $\approx$6 eV and $\approx$0.7 eV, while the excitation via n=2 requires a higher energy of the second laser with energies of $\approx$5 eV and $\approx$1.7 eV [31].

Once the n=3 Ps state has been produced, it can be visualized in lifetime measurements either by photoionization or magnetic quenching. In the case of photoionization a second laser pulse (E= 1.2 eV, $\lambda_{ioniz.}$=1064 nm) frees the positron from the Ps. The positron is then quickly accelerated to a negative electrode where it annihilates. For magnetic quenching the 3^3P Ps state is mixed with the 3^1P state by the Zeman effect. 3^1P Ps annihilates faster than 3^3P Ps, with a lifetime of 125 ps. Both processes lead to a decrease of the fraction of o-Ps decaying in 3 γ-rays and as a result of this, a changed lifetime spectrum.

By applying laser pulses of wavelengths between 1650 and 1700 nm, n=3 Ps can further be excited to Rydberg states. The excitation to states between n=10 and n=25 has earlier been shown by using a slow positron beam, with n=2 as an intermediate step [29]. The maximum energy level, Ps can be excited to, is n=27. At higher levels ionisation starts to affect the Ps atoms[32].

Also the excitation to Rydberg states can be observed using positron annihilation lifetime spectroscopy. The lifetime of Rydberg-Ps is much longer than that of ground state o-Ps. If Ps has been excited to these energy states, an excess of Ps annihilations several hundred nanoseconds after the prompt peak is noticeable in the corresponding lifetime spectrum. Note that this time difference does not correspond to the Rydberg-Ps lifetime, but to the time it takes them to reach the walls of the experimental chamber, where they annihilate.

The limit of the resolution of spectral lines in the visible and UV-range is often set by Doppler broadening. Also the linewidth of the transition of Ps to the n=3-state is determined by Doppler broadening.

Ps atoms, which move toward the exciting UV-laser light source with a thermal velocity v, have a transition frequency which differs from that of Ps atoms at rest by the Doppler shift. The Doppler shifted transition frequency (ω) is given by:

$$\omega = \omega_0 (1 \pm \frac{v}{c}), \tag{15}$$

where c is the speed of light and ω_0 is the transition frequency of a particle at rest. The number of Ps atoms n(v) with velocity v in the direction of the UV-laser is determined by the Boltzmann distribution:

$$n(v) dv = N \sqrt{\frac{m_{Ps}}{2\pi kT}} e^{-m_0 v^2/2kT} dv, \tag{16}$$

here N refers to the total number of Ps atoms and m_{Ps} refers to the mass of the Ps atom. k is the Boltzmann constant and T the temperature. The distribution of

transitions around the center frequency is then given by a Gaussian, with a full width at half maximum $\Delta\lambda$, expressed in terms of wavelength:

$$\Delta\lambda = \frac{2\lambda_0}{c}\sqrt{\frac{2kT\ln(2)}{m_{Ps}}}, \tag{17}$$

where λ_0 is the resonance wavelength of the transition.

1.11 APPLICATIONS OF POSITRONS IN MATERIAL SCIENCES: POSITRON ANNIHILATION SPECTROSCOPY

Positrons can be used as extremely accurate probes for the study of material defects. They exhibit a high sensitivity, furthermore the investigation of materials by positrons is a non-destructive way to analyze samples.

Since the distribution of electrons differs between defects and defect-free regions, positrons sense these differences. While the spatial probability density of positrons shows only small peaks in delocalized free state, positrons are strongly localized at the positions of defects[33].

Different techniques of positron annihilation spectroscopy are based on the analysis of the γ-quants sent out by the annihilating positrons.

Figure 7 indicates the different techniques of positron annihilation spectroscopy. Positrons emitted from a radioactive source penetrate into the sample and thermalize within few picoseconds before they annihilate with an electron. The associated γ-quanta can be measured in different ways, resulting in the 3 types of positron annihilation spectroscopy:

- Positron annihilation lifetime spectroscopy (PALS)

- Doppler broadening spectroscopy

- Angular correlation spectroscopy

1.11.1 *Positron Annihilation Lifetime Spectroscopy (PALS)*

In Positron Annihilation Lifetime Spectroscopy single positrons are implanted into the sample. Their lifetime is measured as the difference between the start
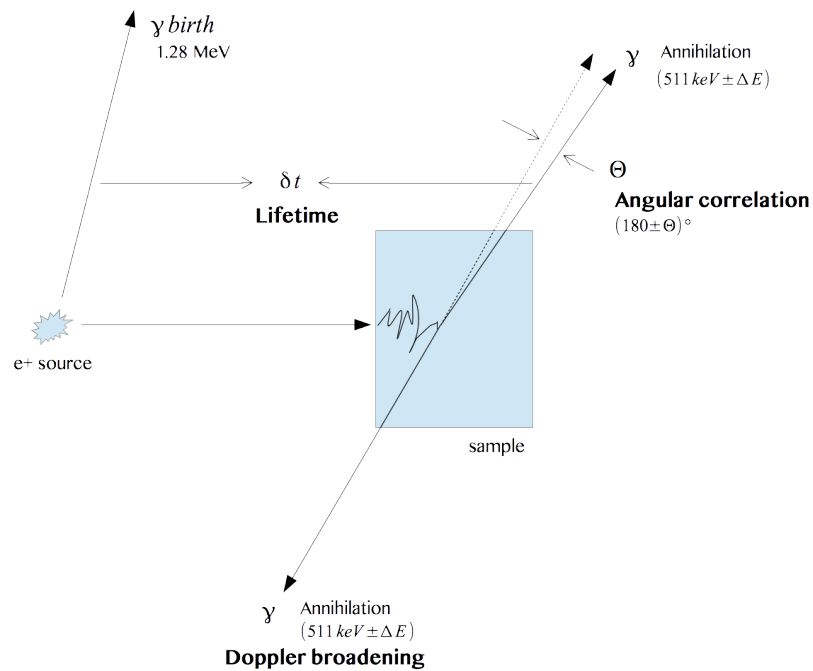
Figure 7: Measurements of the different characteristics of positron annihilation γ-rays, such as lifetime, angular correlation and the Doppler broadening of the annihilation peak, lead to the three main methods of positron annihilation spectroscopy. Picture redrawn after [34]

signal, the 1.28 MeV birth γ-quant emitted directly from the source, and the 511 keV γ-quant, emitted by the annihilation of a positron with an electron of the sample.

The data from single annihilation events are stored and in order to obtain a full lifetime spectrum, more than 10^6 annihilation events are recorded. Typical lifetime spectra show a large prompt peak, resulting from positron and p-Ps annihilations, followed by a more or less rapdily decreasing signal. If there is o-Ps being produced by the interaction of incoming positrons with the sample, the count rate after the prompt peak is enhanced due to the higher lifetime of o-Ps.

The positron lifetime is specified as the inverse of the positron annihilation rate λ_b. λ_b is directly proportional to the overlap between the positron distribution function and the electron distribution function. Consequently lower electron densities result in higher positron lifetimes. To each material a specific positron lifetime can be ascribed due to its specific electron density. Also open volume defects can increase the positron lifetime, since they are lower in electron density than the bulk material.

The lifetime in the trapped state gives information about the nature of the defect, the longer the lifetime, the larger the free volume of the defect. The intensity of the trap component of the lifetime spectrum is associated with the trap concentration.

1.11.2 *Single Shot Positron Annihilation Lifetime Spectroscopy (SSPALS)*

In Single Shot Positron Annihilation Lifetime Spectroscopy a large amount of positrons is implanted into the sample all at once. The resulting annihilation rays are detected in real time.

An obvious benefit of SSPALS in comparison to PALS is that less time for data acquisition is needed. However, the time resolution of SSPALS spectra depends on the temporal spread of the positron bunch, and thus it is typically not as good as the time resolution of a PALS spectrum. Other to that, a SSPALS spectra looks similar to a PALS spectra. Positronium formation becomes noticeable by the same indications [35]. A schematic sketch of a typical SSPALS/ PALS spectrum can be seen in figure 8.
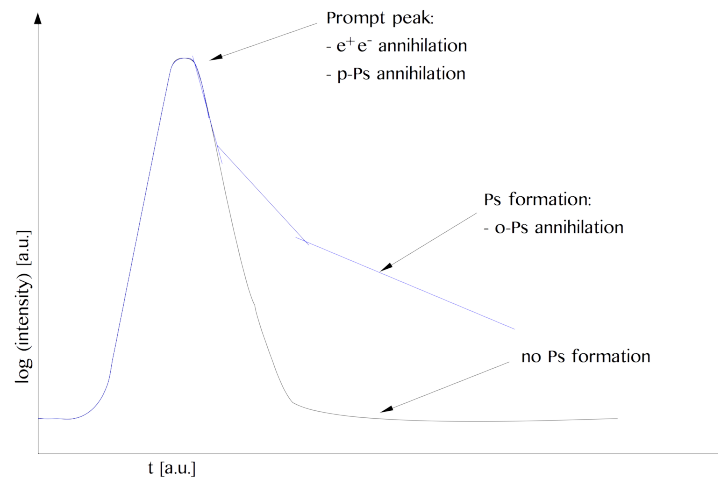

Figure 8: Comparison of two PALS/SSPALS spectra showing the difference between the curves for a sample with (blue curve) and without (black curve) Positronium formation. In the case of Ps formation the count rate after the prompt peak is higher due to the longer lifetime of o-Ps.

1.11.3 *Doppler broadening spectroscopy*

Due to the momentum distribution of the electrons involved in the annihilation processes with the positrons, the 511 keV signal does not result in a sharp line,

but in a Doppler broadened peak.

The reason for assigning this energy shift to the electrons only, is that the positrons thermalize very quickly after they enter the material and thus do not contribute. The Doppler shift ΔE for each photon is given by:

$$\Delta E = \frac{c}{2} p_L, \tag{18}$$

where p_L is the longitudinal momentum of the electron parallel to the direction of the emitted annihilation γ-quants and c is the speed of light.

To characterize the shape of the 511 keV annihilation peak, the S- and the W-parameter are introduced. The S-parameter refers to the signals close to the main peak at 511 keV and thus arises from annihilations with valence electrons, which are low in momentum. It is calculated by:

$$S = \frac{A}{C} \tag{19}$$

In formula 19 A refers to the central area of the Doppler peak and C to the total peak area (see figure 9). If many of the annihilations occur with valence electrons, the Doppler peak gets narrower and thus the S-parameter increases. As the density of valence electrons in open volume defects is larger than the density of core electrons, one can conclude a large density of open volume defects from this fact.

On the other hand the W-parameter refers to annihilations with high momentum, core electrons.

$$W = \frac{B}{C}, \tag{20}$$

where B is defined as the number of counts in the wings region of the peak.

For the measurements, related to material characterization presented in this thesis, the central area of the peak has been defined as $|E - 511|\,keV < 0.85\,keV$. The wings region has been defined as $2.75\,keV < |E - 511|\,keV < 4\,keV$, and the total area as $|E - 511|\,keV < 4.25\,keV$.

Of course the values of the S- and W-Parameters can change by choosing different energy windows for A and W. Therefore when analyzing data, these are always compared to the values of a defect-free sample of the same material deduced for the same energy windows.
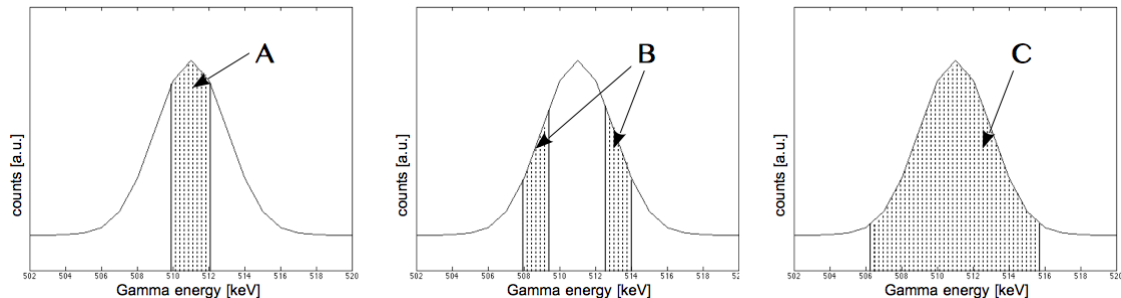

Figure 9: Schematic drawing of the Doppler broadened 511 keV annihilation line and definitions of central area (A), wings area (B) and total peak area(C).

Measurements of the S- and W-Parameter in dependence of the positron implantation energy give information about the distribution of defects in depth of the sample. By analyzing these defect depth profiles one can gain information about possible material changes and the interfaces in between those. Limitations in defect depth profiles arise due to broad implantation profiles (see figure 5) at high energies, so analyses of deeper sample layers always go hand in hand with less spatial resolution. [36] [22] [21] Mainly Doppler broadening spectroscopy uses high purity germanium (HPGe) detectors to detect the annihilation γ-rays. HPGe detectors show typical energy resolutions of 1-1.5 keV at 511 keV[17]. Especially when it comes to measurements of the W-parameter in order gain information about the chemical environment of the sample, higher resolutions are advantageous.

1.11.4 *Doppler broadening spectroscopy in coincidence*

For Doppler broadening coincidence measurements two detectors are placed 180° apart from each other, one on the left side, one on the right side of the sample. In this way both annihilation γ-rays can be recorded.

By measuring both γ-rays of one annihilation process, additional conditions are imposed to the signals: For one thing, the two γ-rays have to be detected in

roughly opposite directions at the same time. And for another thing, the sum of the energy of the two of them has to fulfill the following condition[37]:

$$E_1 + E_2 = 2m_0c^2 - E_{+,-} \approx 1.022 \text{ MeV,} \qquad (21)$$

where $E_{+,-}$ is the binding energy of the electron-positron pair and m_0 is the rest mass of the electron/positron.

Measuring in coincidence improves the resolution by a factor $\sqrt{2}$. Additionally the peak to background ratio is significantly higher. Typical values of this ratio for coincidence mesurements are around 10^5, while they are only ≈ 200 for spectra collected with a single detector[37].
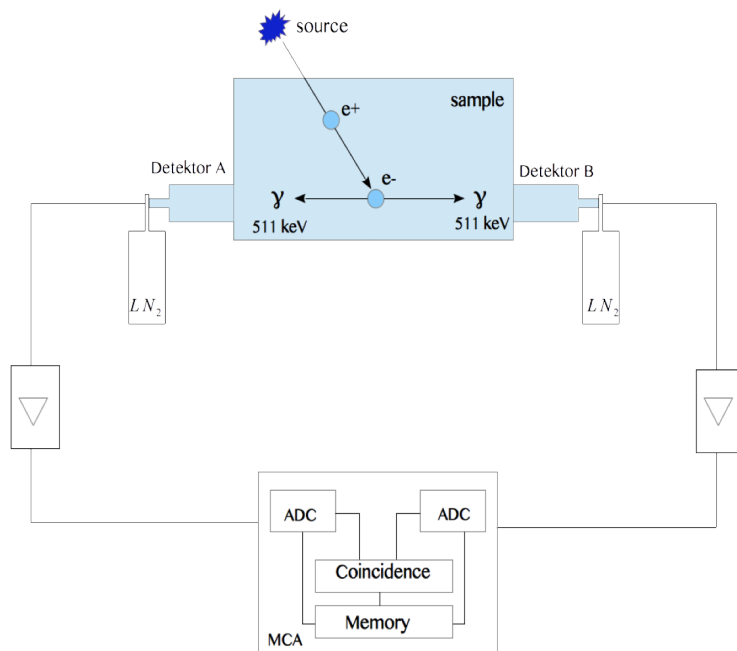

Figure 10: Experimental set-up of a coincidence Doppler broadening measurement: For the registration of both collinear coincidence γ-rays, two liquid nitrogen cooled Germanium detectors are used. The signals from the detectors are then further amplified and sent to a multi-channel analyzer (MCA), consisting of 2 analog-digital-converters (ADC), a coincidence and a memory chip

1.11.5 *Positronium formation spectroscopy, $F_{3\gamma}$ factor*

Positron annihilation can also occur after the formation of positronium. As mentioned previously, o-Ps decays into three gamma rays, each of energies ranging from 0 to $\sim m_0c^2$, with a total energy for all three of them of $\sim 2m_0c^2$.

For this reason, γ-rays induced by the annihilation of o-Ps are mostly accumu-

lated in the valley area of the energy spectrum (see figure 11). Hence spectra involving a high number of positron annihilations from the o-Ps state are remarkably different to those obtained from two-photon processes.

The parameter used to describe the positronium formation is the so-called $F_{3\gamma}$ parameter[38].

$$F_{3\gamma} = [1 + \frac{P_1}{P_0} \frac{R_1 - R_F}{R_F - R_0}]^{-1} \tag{22}$$

with

$$R_{1,F,0} = (T_{1,F,0} - P_{1,F,0})/P_{1,F,0} \tag{23}$$

Here T_F and P_F correspond to the total area and the peak area of the measured spectrum. $T_{0,1}$ and $P_{0,1}$ are the values of the total and peak area of two calibration samples, one of 0 % and one of 100 % positronium production.

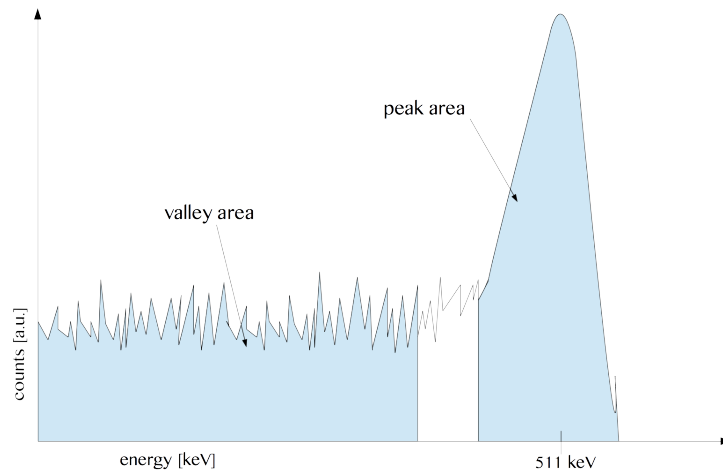Figure 11: Sketch of a possible energy spectrum indicating the ranges of the valley and the peak area. γ-quants induced by o-Ps decay increase the valley area, while e^-e^+ annihilations and p-Ps decay increase the peak area.

It has been shown that the $F_{3\gamma}$ fraction is not only material specific, but also related to the presence and dimension of pores as well as their interconnectivity [22] [21].

EXPERIMENTAL

2

EXPERIMENTAL

2.1 AEḡIS (ANTIMATTER EXPERIMENT: GRAVITATION, INTERFEROMETRY, SPECTROSCOPY)

2.1.1 *The AEḡIS experiment, a brief introduction*

The weak equivalence principle, also known as the universality of free fall reads: All test particles in a given gravitational field undergo the same acceleration, regardless of their mass and composition[39].

In the Newtonian picture this is interpreted as the gravitational force being exactly proportional to the inertial mass, while Einstein derived the Einstein Equivalence Principle from this fact[40].

In the 16$^{\text{th}}$ century Galileo conceived his famous gedanken experiment of studiyng the free fall of a feather and a stone from the tower of Pisa[41]. Since that time, the weak equivalence principle has been tested precisely for matter[42], but never directly for antimatter.

Within the ongoing research on antimatter, the question of its behaviour in a gravitational field arised. According to the General Theory of Relativity, antimatter has a positive mass, so an antihydrogen atom consisting of an antiproton and a positron, should behave exactly like a hydrogen atom in the earth's gravitational field. The Weak Equivalence Principle should still be valid.

The main goal of the AEḡIS experiment, placed at CERN, is to measure the effect of the Earth's gravitational acceleration (ḡ) on antihydrogen (H̄) with an accuracy of 1%. It was first proposed in 2007 and the construction of the main apparatus was completed at the end of 2012. The experiment is situated at the Antiproton Decelerator (AD) ring.

Figure 12 shows a schematic sketch of the first part of the experiment where a beam of antihydrogen atoms, the simplest form of electrically neutral antimatter,

29

is produced: Pulses of positrons, coming from a ^{22}Na source, hit a specially designed, nanostructured target and form positronium.

These positronium atoms are then Laser-excited to Rydberg states (Ps*) and combined with antiprotons ($\bar{p}$), coming from the AD, to form excited antihydrogen ($\bar{H}^*$) via a charge exchange reaction:

$$Ps^* + \bar{p} \longrightarrow \bar{H}^* + e^- \tag{24}$$

There are several advantages of using Rydberg positronium. Firstly the cross-section for antihydrogen production is bigger for higher energy states. It is proportional to $a_0 n^4$, where a_0 is the Bohr radius and n is the principal quantum number of Ps.

Additionally the energy states of the antihydrogen are defined by the energy state population of the positronium and thus well predictable when using excited Ps. To enable a gravity measurement of antihydrogen in the second part of the experiment, antihydrogen has to be cold. The reason is that for this case, the beam divergence is lower and the deflection by gravity is bigger. For the creation of cold $\bar{H}$, the antiprotons are cooled in a trap system before they are used for the charge exchange reaction. Also the Ps converter target is chosen and manipulated in such a way that it creates Ps of low energy.

The produced antihydrogen is than accelerated horizontally through Stark acceleration upon a so-called moiré deflectometer (see figure 13). This instrument consists of a system of gratings that split the beam into parallel rays, which form a periodic pattern.

When the antihydrogen atoms arrive at the end of the system, hence come in contact with matter, they annihilate at positions which reproduce the periodic pattern. By the drifts of these annihilation points it can be measured how strong gravity affects antihydrogen atoms of different velocities during their horizontal flight. By the means of these data, the strength of the gravitational force between the earth and the antihydrogen atoms can be determined [43].
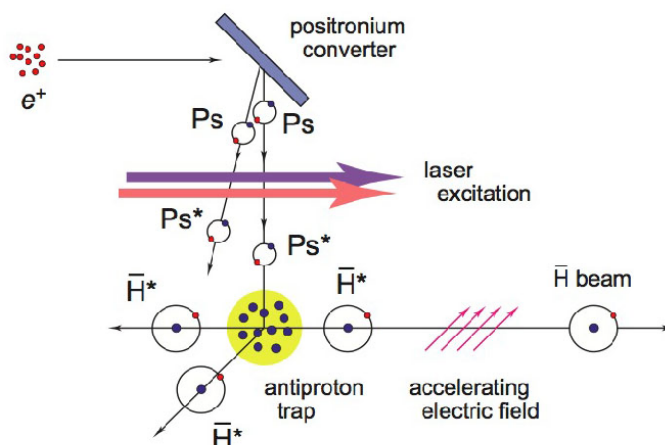
Figure 12: Antihydrogen formation in AEḡIS: Positrons are accelerated towards a nanostructured Ps converter target, the produced Ps is laser-excited to Rydberg states. Ps* and p̄ form excited H̄, which is then accelerated in an electric field. Picture taken from [43]
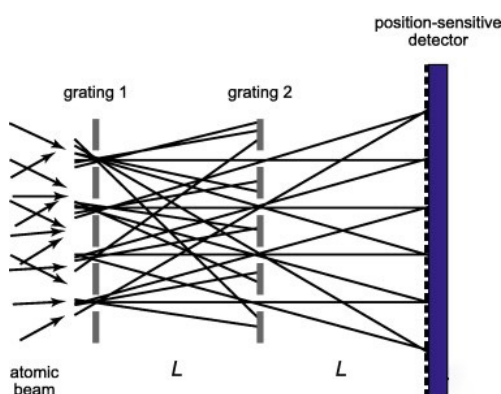

Figure 13: Moiré deflectometer: The system consists of 2 identical transmission gratings and a spatially resolving detector for antiproton annihilations. Through the vertical shifts of the antiproton annihilation points the effect of gravity on antihydrogen can be determined. Picture taken from [43]

2.1.2 *The AEḡIS positron system*

Figure 14 shows a schematic drawing of the first parts of the AEḡIS positron system. As it is essential for the lifetime of positrons the whole system is kept under good vacuum conditions by several roughing-, ion- and cryopumps. The guidance of the positrons is realized by electrostatic and magnetic fields.

Moderated positrons leaving the source region are initially cooled in the trap. In the next step, positrons are guided to the accumulator, where a variable number of pulses from the trap can be stored. Bunches of positrons leaving the accumulator can then either be sent towards the buncher and the test chamber, or to the main apparatus.
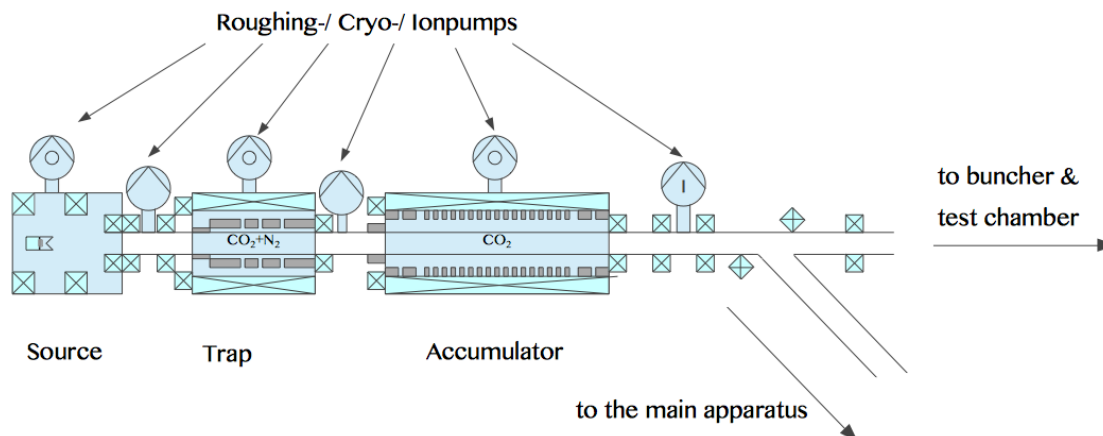
Figure 14: Sketch of the AEḡIS positron system, consisting of the basic components source, trap and accumulator. Positrons are emitted from a ^{22}Na source. At the trap, they are accumulated in a step potential and cooled down by two buffer gases. Within the accumulator, it is possible to store a certain number of pulses from the trap in a ring potential. Positrons are cooled down further in the accumulator, using only one buffer gas.

2.1.2.1 *Source*

As mentioned earlier, the AEḡIS positron source is realized by the isotope ^{22}Na. In 2011 the source had an activity of 18 mCi. As ^{22}Na has a half-life of $\tau_{1/2}$=2.6 yrs.[7], the activity during 2015 can be calculated to $\approx$7 mCi.
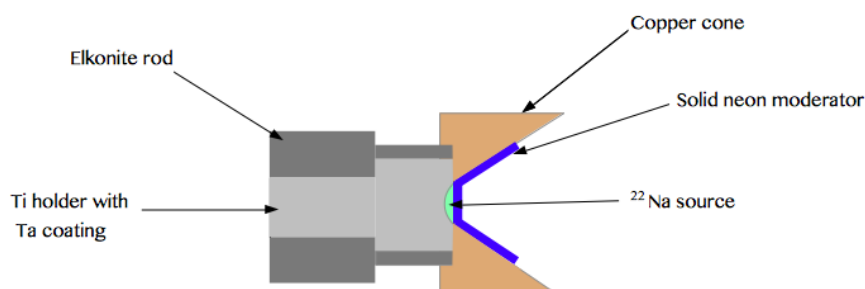
Figure 15: Schematic drawing of the source set-up (producing company: First Point Scientific Inc. technology). The ^{22}Na source is mounted on a head made of tantalum coated with titanium. On top of the source the solid neon moderator is grown on a copper cone.

The ^{22}Na source is mounted on a head made of tantalum coated with titanium. As titanium is a high Z-material, it is very likely to reflect positrons. The head is placed inside the source holder, which is made from a tungsten-copper alloy. On top of the source, the solid neon moderator is grown on a copper cone, kept at a potential of 18 V, in order to push emitted positrons in the direction of the trap. On the left side of the source holder, a helium-pump refrigerator is placed.

It keeps the source chamber in high vacuum ($\approx 10^{-8}$) and cools it down to 7 K, in order to keep the neon in its solid state.

To ensure a high moderator efficiency, neon can be evaporated and regrown automatically. By heating the system the solid neon gets gaseous and can be pumped out. New neon gas can be injected into the chamber and as the source chamber is cooled down again, it solidifies on the source. Since the initial layer contains many defects, it has to be annealed at 9.3 K before the chamber is again cooled down to 7 K.

The efficiency of the moderator is around $\epsilon \approx 2.5 \times 10^{-3}$. Around the source region a pair of Helmholtz coils is installed which generates a magnetic field parallel to the translational axis.

2.1.2.2 *Trap*

The AEḡIS trap consists of a Surko trap with additionally applied rotating wall to the central electrode, as it is described in detail in section 1.6.2.

The value of the applied magnetic field around the trap region is 0.07 T. Since the positrons coming from the source enter the trap rather fast, the trap is containing a large amount of the buffer gases CO_2 and N_2 to cool the positrons down quickly and efficiently. The gas pressure in the trap is set to $p_{trap} = 10^{-4}$ mbar. Consequently the positron lifetime is, with values around a few hundred milliseconds, quite low.
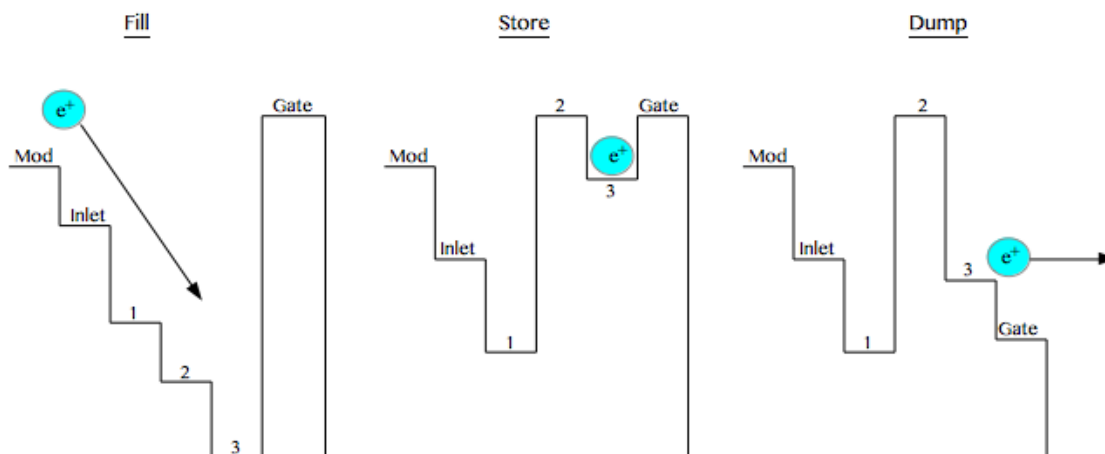
Figure 16: Positron trapping: The process is controlled by the six electrodes Mod, Inlet, 1, 2, 3 and Gate. In the first phase, the potentials on the first five electrodes are lowered to allow the positrons to get in. To 'store' the positrons, they are captured between electrode 2 and the gate electrode by raising the potential of electrode 2. Finally they are dumped by lowering the potentials of electrode 3 and the gate.

Figure 16 shows the process of filling, storing and dumping of positrons. In the first phase, the trap is filled. By setting low potentials to the first five electrodes, Moderator (Mod) to electrode 3, positrons are enabled to get into the trap. When reaching the gate electrode, they are reflected back by its high potential. During this process, positrons are cooled down by buffer gases and thus being trapped in the electrode with lowest potential (3). In the following step, the potentials of electrode 2 and the gate electrode are raised to store positrons and to compress them by the rotating wall. In the last step positrons are dumped and sent into the direction of the accumulator by lowering the potential of electrode 3 and the gate fast. The electrode potential can be switched within the order of 100 µs. All in all the trapping takes 0.15 s.

2.1.2.3 *Accumulator*

In principle the accumulator is set up in a similar way as the trap. Positrons are also captured, cooled and finally released again within the three phases of filling, storing and dumping (see figure 17).

As the purpose of the accumulator is to collect high numbers of already cooled positrons, only CO_2 is used as a buffer gas and also the gas pressure is significantly smaller than in the trap, with $p_{accumulator}=6 \times 10^{-8}$ mbar. Consequently the positron lifetime can be enhanced to several minutes.

While the potential well of the trap has a stepped shape, it is harmonic within the accumulator, set up by 21 electrodes. The potential allows confinement of the positron cloud in the transversal direction.

Another difference to the trap is that the accumulator cannot not only be filled once, but various times. The user can decide how many pulses of positrons from the trap should be accumulated before dumping the positrons into the direction of the transfer line.

For dumping a potential with a constant negative slope is applied (see figure 17, right). This potential is adjustable, so that the positrons can be released with various energies, ranging from 50 eV to 400 eV.
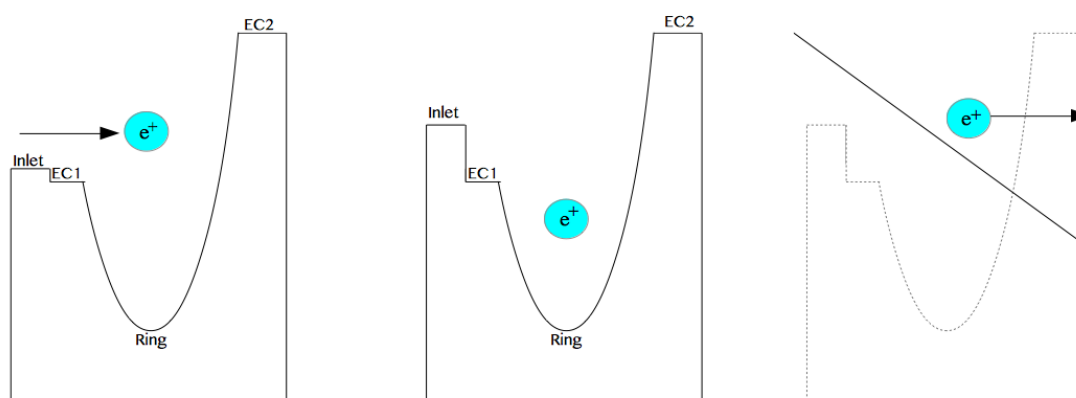

Figure 17: Positron accumulation process: By lowering the potentials of the inlet and the EC1 electrode, positrons get into the accumulator. To keep them within the potential well, the inlet potential is raised. For dumping the positrons the potentials are changed to a variable falling slope.

2.1.2.4 *Transfer Line & Buncher*

After the positrons have left the accumulator with a temporal spread of ≈20 ns, they move along the transfer line, where they are only confined radially by big solenoids, each carrying a current of 100 A (see figure 18).

The beam tube is evacuated to a pressure of 5×10^{-10} mbar. An actuator with a phosphor screen can be moved into the tube in order to visualize and characterize the positron beam.

A big angled coil acts as magnetic beam switch. If it is switched on, positrons are guided down to the main apparatus. If not, they just continue moving towards the buncher and the experimental chamber. After the magnetic transport along

the transfer line, the positron guiding can be switched to purely electrostatic transport, before the positrons get into the region of the buncher which consists of 28 electrodes. The reason therefor is that some positronium experiments as well as some diagnostic tools in the test chamber would be affected by magnetic fields.

The first buncher electrode consists of μ-metal, which acts as a shielding for the magnetic field and is kept at a voltage V_1=-800 V. A second electrode, next to it, is kept at a voltage of V_2=-2100 V.

The following 25 electrodes make up the buncher. Initially they are all kept at a voltage of V_{3-27}=-535 V. At the moment when the positrons enter the buncher, the electrode potentials are switched to form a parabolic-shaped potential along the tube axis, superimposed to a high voltage. The parabolic shape compresses the positron cloud transversally as it accelerates positrons further away stronger than those close to the test chamber.

The high voltage potential accelerates the positron bunch and can be changed from 3-10 kV. The duration of the positron pulse is 30 ns and the rising time is 2-3 ns. For more details concerning positron bunching and the electrostatic transport system of AEḡIS see [44].
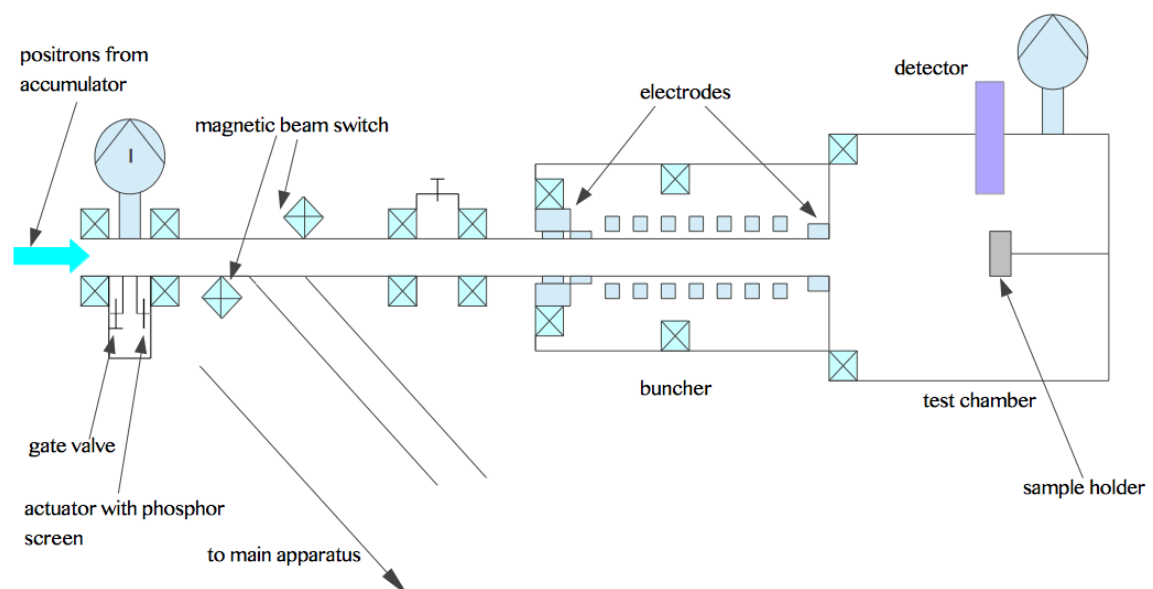

Figure 18: Transfer line and buncher: Positrons from the accumulator are guided along the transfer line magnetically. They can either be sent towards the main apparatus or towards the test chamber by activating or deactivating a magnetic beam switch. The buncher is made up by 27 electrodes forming a parabolic potential superimposed to a high voltage.

2.1.2.5 *Test chamber*

Figure 19 shows schematically the set-up of the test chamber. The sample holder is installed perpendicular to the direction of the positron beam ejected from the buncher. Up to three samples can be fixed on it at the same time. The sample holder is moveable without opening the test chamber by means of an actuator connected to it.

If the actuator is put to the empty position on the very left of the sample holder (see figure 19), the positrons can pass through and end up on the multi channel plate (MCP) and phosphor screen assembly, where they can be visualized.

On top of the chamber there is an intend, where a detector ($PbWO_4$ crystal and PMT Hammamatsu R11265-100) can be placed.

The chamber has several viewports, through one of them the laser can pass into the test chamber, perpendicular to the direction of the positrons.
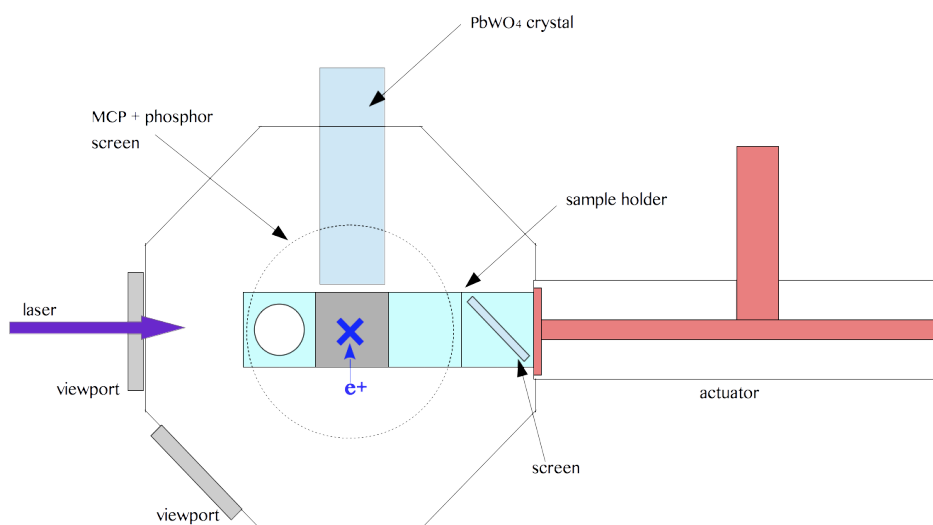

Figure 19: Test chamber: Positrons are accelerated into the test chamber, perpendicular to the target holder, which is moveable via an actuator. At an intend, on top of the chamber, a detector is placed. For a visualization of the positron beam, it can be sent towards an MCP and phosphor screen assembly. Through one of the view ports, a laser pulse can pass into the chamber.

2.1.3 *The AEḡIS main apparatus[45]*

By activating the coils of the magnetic beam switch (see figure 18) positrons are guided to the main apparatus. It consists of the beam tube, a series of electrodes, kept at ultra-high vacuum at a pressure of 10^{-11} mbar, surrounded by two strong, superconducting solenoid magnets.

The first coil is referred to as 5 T solenoid in figure 20. The magnetic field of 5 T of the first coil is generated by a current of 183 A. The current through the second coil (1T solenoid) is set to 85 A and the corresponding magnetic field strength is 1 T. In order to maintain the superconductivity of the coils, they have to be cooled down to temperatures of 4 K. This is realized by two cylindrical vessels surrounding the beam tube. The inner vessel is filled with liquid helium (T_{LHe}=4 K), the outer one, which is filled with liquid nitrogen (T_{LN_2}=77 K), acts as an additional shielding between the temperature of the magnet and the room temperature of the surroundings.

The antiprotons are injected into the main experiment by the antiproton decelerator (AD) ring and come in bunches of 10^7 antiprotons with energies of 100 MeV. Electrodes in the 5 T region are used to catch and accumulate positrons and antiprotons. In the catching trap, the antiprotons are cooled down as they lose energy by inelastic collisions with electrons. In the accumulating trap, antiprotons are collected to create a cloud with a sufficient number density to interact with the positronium cloud in the following steps.

In the 1 T solenoid there are several sets of traps, that treat positrons and antiprotons separately. Positrons captured in the 5 T region are sent to the 1 T diochotron trap that moves the positrons off-axis to the beam line. In the launch trap they are radially and longitudinally compressed and then accelerated towards the positron-positronium converter target. Antiprotons in the 1 T region are compressed and then stored in the antihydrogen formation trap, which is placed in front of the positron-positronium converter. Ps produced by the converter enters in this semi-transparent trap after excitation to Rydberg states. Finally antihydrogen is produced via a charge exchange reaction. At the end of the beam line a moiré deflectometer measures the vertical displacement of the antihydrogen atoms.
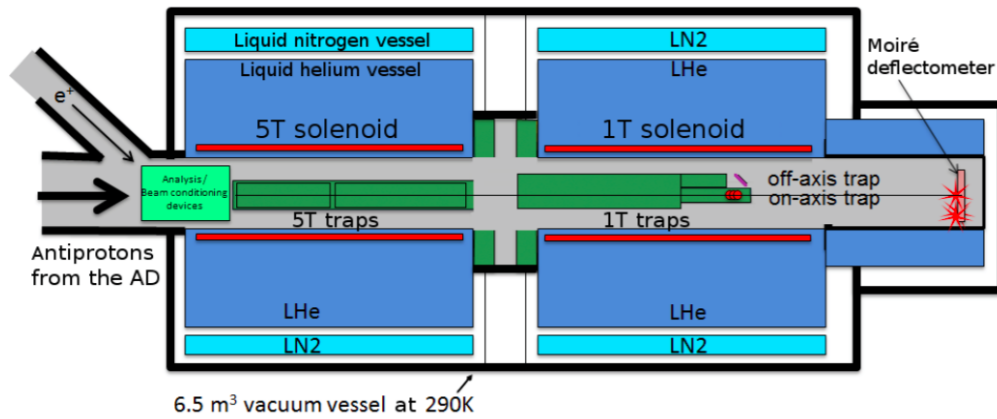
Figure 20: The main apparatus consists of a beam tube at UHV surrounded by two superconducting magnets producing magnetic fields of 5 T and 1 T. Both regions contain several traps to catch, cool down and accumulate positrons and antiprotons seperately. At the end of the 1T solenoid the antihydrogen formation trap is placed, where antihydrogen is being formed. The beam of antihydrogen atoms is sent towards the moiré deflectometer. Picture taken from [26].

2.1.3.1 *The AEḡIS laser system*

The laser system is an essential part of the AEḡIS experiment, delivering the laser pulses to excite and photoionize positronium. Its layout can be seen in figure 21. The system uses a Q-switched Nd-YAG laser providing an energy of 650 mJ and pulses of 4 ns.

The laser assembly can generate seperate pulses of the three different wavelengths 1064 nm, 532 nm and 266 nm correponding to the 1st, 2nd and 4th harmonic of the YAG radiation. The 2nd and 4th harmonic are created by non-linear KTP ($KTiOPO_4$) crystals.

The laser system has to produce UV-light of a wavelength of 205 nm for the excitation to n=3 (see section 1.10) as well as IR-light of approximately 1670 nm wavelength (depending on number of Rydberg state) in order to excite positronium to Rydberg states. Additionally pulses of 1064 nm wavelength are required for the photoionization of the n=3 o-Ps states. Therefore the system is split into two optical paths.

For the UV-radiation, an OPG (optical parametric generator) is pumped by the 2nd harmonic of the 532 nm wave of the YAG-laser. The output light of the OPG has a wavelength of 894 nm and is sent to an OPA (optical parametric amplifier) where it is amplified. In the next step the 894 nm wave is frequency summed with the 3th harmonic of the 266 nm wave in a non-linear barium borate crystal. The

final laserlight output can be tuned between 204 nm and 206 nm by means of the temperature of the OPG. It has a temporal full width half maximum (FWHM) of 1.5 ns. The bandwidth is 112 GHz. Energies can be varied up to 60 μJ. The laser spot is of elliptical shape with a vertical full width half maximum (FWHM) of 6 mm and a horizontal FWHM of 4 mm.

The second laser pulse of IR-light is generated as follows. The 1st harmonic of the 1064 nm wave of the YAG is directed to a beamsplitter, where a part of it goes straight through, the other part is reflected in perpendicular direction. The first part just keeps its wavelength of 1064 nm and can be used to ionize the excited positronium states. This pulse has an energy of 50 mJ and a temporal FWHM of 10 ns.

The second part goes on to an OPG where it is transferred into light of a wavelength of 1650-1700 nm and subsequently amplified by an OPA. Finally both pulses pass a dichroic mirror, which blocks the 1064 nm light. The time length of this laser pulse is 4 ns, the energy can be varied up to 55 mJ. The spot is of circular shape with a diameter of 8 mm.

Via transfer lines, the produced pulses can either be carried to the main experiment or to the test chamber. Inside the test chamber a ceramic screen, monitored by a camera, is placed which enables an alignment of the laser pulses in the target region.

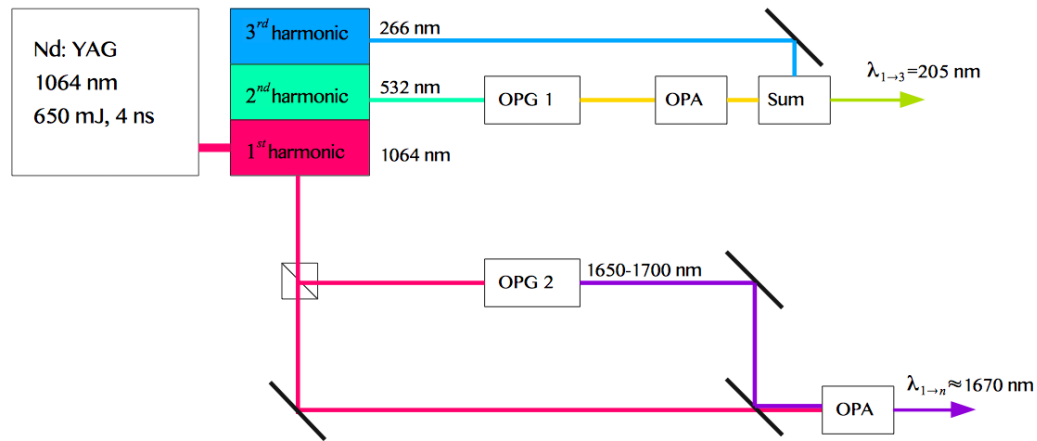For further information on the AEḡIS laser system see for example [32].

Figure 21: Laser system: An Nd-YAG laser assembly provides seperate pulses of 1064 nm, 532 nm and 266 nm. For the production of UV-light (205 nm) and IR-light (1670 nm) the system is split into two optical paths. For the UV-pulse, the 532 nm, 2nd harmonic passes an OPG and an OPA and is then frequency summed with the 266 nm, 3rd harmonic. To generate the IR-pulse a part of the 1064 nm 1st harmonic goes on to an OPG and an OPA, which transfers the pulse to a wavelength of 1650-1700 nm and amplifies it.

2.2 VEPAS (VARIED ENERGY POSITRON ANNIHILATION SPECTROSCOPY) LABORATORY COMO

2.2.1 *Experimental setup*

Positrons emitted directly from a radioactive source show a relatively broad energy distribution (see chapter 1.4). So, if there is no moderator present in between the source and the specimen, they get implanted into various regions of depth. For the investigation of the bulk of homogenous materials this does not bring up any difficulties. However, if the samples are composed of one ore more different thin layers, that should be analyzed seperately from each other, positron beams have to be monoenergetic and tuneable.

To reach the maximum efficiency for investigating of thin layers and defects near surfaces and at interfaces, the Como VEPAS laboratory uses slow positron beam techniques. Positrons, that leave the moderator of the source, are guided through a system of electrical lenses and a beam bender in order to obtain such a confined, monoenergetic positron beam and thus defined small penetration depths. The size of the positron spot on the sample is ≈5 mm. Positron implantation energies can be tuned from 0.1- 17.1 keV.

The experimental set-up of the slow positron beam of the VEPAS laboratory Como consists of the following parts:

- Positrons are emitted by a ^{22}Na radioactive source, showing an activity of ≈7-8 mCi during the time of the measurements.

- Right after the source a crystalline tungsten foil for the moderation of positrons is placed. It has a diameter of ≈1 cm and a thickness of ≈1 µm. Positrons are emitted perpendicular to the surface with energies of ≈3 eV.

- The positron beam is set up by the main components, i.e. the first track, the deflection unit and the second track.
  Within the first track positrons are initially gathered, accelerated and made parallel through a series of electrodes.
  The deflection unit consists of parallel plates, which bend the beam by 90°. In this way positrons and γ-rays emitted directly from the source cannot reach the sample. Furthermore, the deflection unit ensures that only monochromatic positrons are transported towards the sample.
  The first lense of the second track refocuses the beam, the second one accelerates the beam. The third lense consists of three electrodes and focusses the beam on the sample.

- The test chamber is kept at a vacuum of 10^{-7} mbar by two roughing pumps and two turbopumps in series. There is an actuator in order to mount the sample holder together with the sample perpendicular to the positron beam. The final kinetic energy of the positrons is defined by the potential difference between the sample and the moderator.

- Perpendicular to the second track, outside of the test chamber and 180° apart from each other, two high purity germanium (HPGe) detectors are placed. They are cooled with liquid nitrogen and connected to a multi channel analyzer (MCA) to measure the spectra in coincidence.
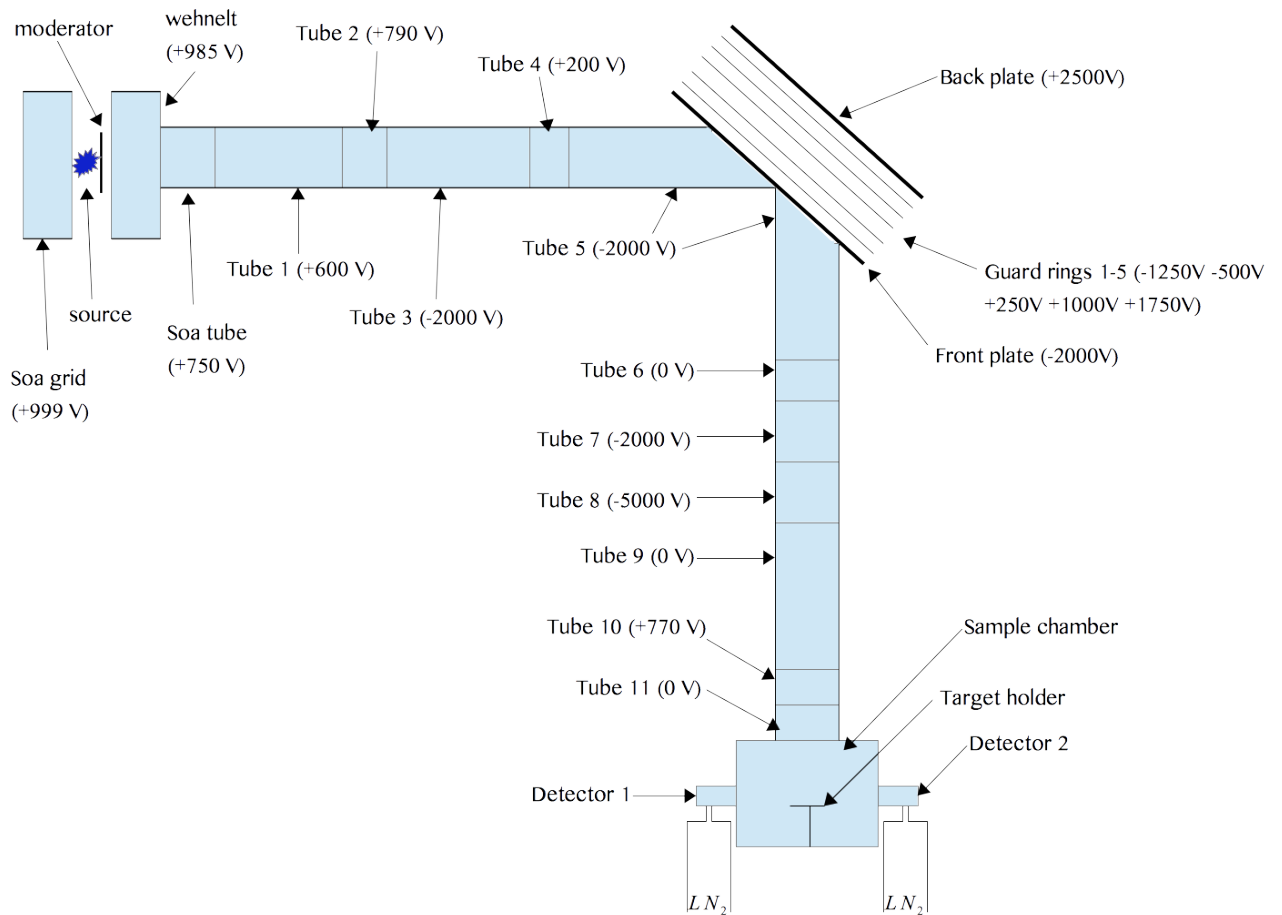
Figure 22: Set-up of the COMO Slow Positron Beam: Positrons leaving the source are moderated by a tungsten foil. They are accelerated and focussed within the positron beam, set up by the main components: first track, deflection unit and second track. Positrons are implanted into the sample with energies tuneable from 0.1 keV to 17.1 keV.

RESULTS AND DISCUSSION

RESULTS AND DISCUSSION

3.1 POSITRON TRANSPORT TO THE TEST CHAMBER

For the laser excitation measurements described later, positrons are guided into the test chamber. To enable an efficient transport, some effort has to be made in the forefront.

First of all, the magnetic switch, placed after the accumulator (see figure 18) has to be turned off, so that the positron bunch goes on straight to the test chamber and not downwards to the main apparatus. Also, before important measurements, the system has to be optimized. Here the most important parameter is the number of positrons reaching the target. This number depends on the transport efficiency, mainly on the positron lifetime in the accumulator determining the number of positrons that can be stored. Through varying conditions in the surroundings of the experiment, as changing magnetic and electric fields, the optimum settings are not constant. For the optimization process, the positron signal at the exit of the accumulator can be monitored by a small, moveable CsI-scintillator coupled to a photodiode. Certain parameters of the system, as for example the frequency of the rotating wall or the strength of magnetic and electric fields during the storage are then varied until the positron signal is optimized. Previous measurements have shown that the magnetic field has a positive effect on the extraction of positrons from the buncher[46].

After this optimization process, it has been estimated that up to $\approx 1.2 \times 10^7$ positrons reach the target, if the magnetic field in the target region is set to 250 G.
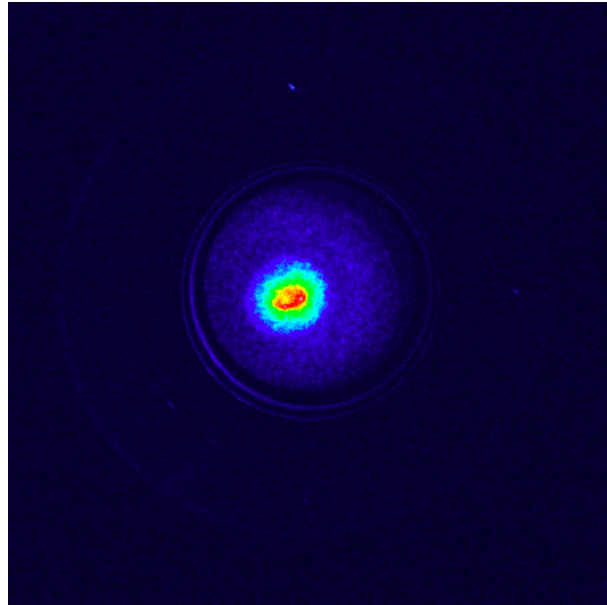
Figure 23: Image of the positron pulse on the phosphor screen (see figure 19) using a positron implantation energy of 3.3 keV.
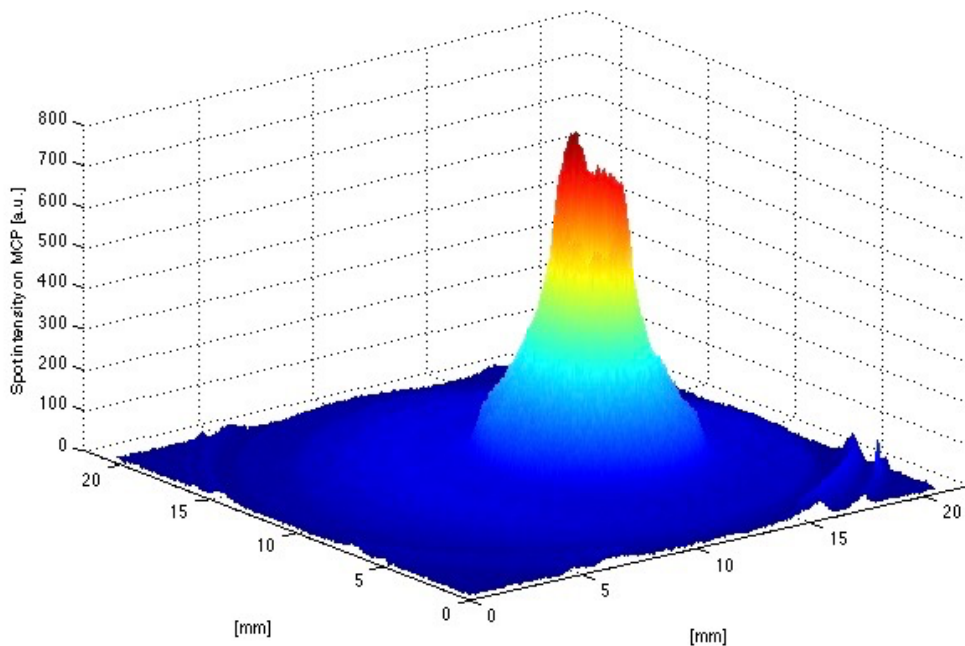
Figure 24: 2D map of the positron beam intensity, monitored by the MCP detector, using a positron implantation energy of 3.3 keV. The diameter of the area of the spot at FWHM and at 20% of the overall intensity maximum were calculated to 3.28 mm and 6.95 mm via Matlab.

In order to monitor the positron spot, the sample holder can be moved to the edge of the test chamber. In this configuration, the positrons get implanted directly on the multi-channel plate detector (MCP). The positron pulse is then imaged on the phosphor screen by a charge-coupled device camera.

The data describing the intensity distribution on the MCP can be acquired by the online AEḡIS data acquisition tool 'Captor' and was further analyzed using Matlab.

Figure 23 shows the positron spot on the MCP. The data is acquired using a positron implantation energy of 3.3 keV, set at the buncher.

Figure 24 shows a 2D map of the beam intensity at the phosphor screen. The diameter of the area at FWHM has been calculated to ≈3.3 mm, the diameter at 20% of the maximum to ≈7.0 mm. To do so, a data matrix containing the intensity values at the MCP was evaluated. By logical indexing and masking the data region with intensities higher than the specified values (bigger than 50% and 20% of the overall maximum) was found. The distances on the MCP were calculated from the indexes of the intensity regions.

It has to be mentioned, that this data set was acquired while surrounding experiments in the hall were working, i.e. having switched on their magnetic and electric fields. Narrower distributions could be found while other experiments were switched off [44].

3.2 POSITRONIUM FORMATION

After a successful transport of positrons into the test chamber, Ps formation in the positron-positronium converter (see section 3.2.1) and its emission into vaccum (as required by the proposal of the AEḡIS experiment) has been tested.

Ps formation has been detected via SSPALS measurements. SSPALS spectra have been acquired by a $PbWO_4$ detector, coupled to a Hammamatsu R11265-100 PMT. Different detector systems have been tested previously, as for example Cherenkov radiators and plastic scintillators as γ-ray converters. The $PbWO_4$ detector shows the lowest noise-level after the prompt peak; also the signal of the background spectrum drops to the noise-level very fast [46]. For these reasons, this detector is used to acquire all the data presented in this work.

Figure 25 shows the comparison of SSPALS spectra, normalized to the same prompt peak amplitude, acquired using a positron implantation energy of 3.3 keV. The background spectrum (black curve in figure 25) is recorded, moving the actuator to a position, where the positrons annihilate at the target holder, made from aluminium. It shows a large annihilation peak, followed by a fast decrease to noise-level, as it is expected.

For the record of the second spectrum (red curve in figure 25), the target (p-type (111)-Si) is moved to the center of the positron bunch. It also shows an annihilation prompt peak, but in this case, followed by a slowly decreasing signal. The slowly decreasing component clearly indicates the formation and annihilation of of o-Ps.
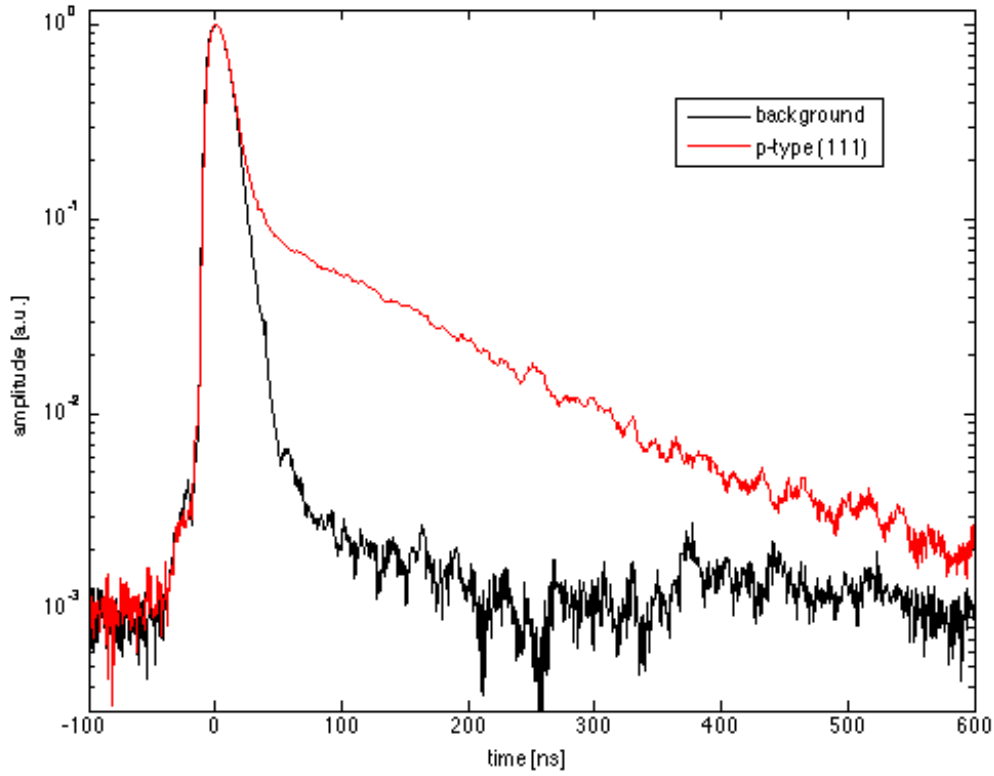
Figure 25: Comparison of normalized SSPALS spectra implanting positrons into the aluminium target holder (black line) and into the positron-positronium converter (p-type (111)-Si, red line). Each spectrum is an average of 15 shots from the accumulator.

It is possible to calculate the Ps lifetime from an SSPALS spectrum since the probability of o-Ps decay follows an exponential function:

$$N(t) = N_0 e^{-\frac{t}{\tau}}, \tag{25}$$

where N_0 is the initial number of Ps atoms, t is the time since the initial Ps formation and τ is the Ps lifetime. To evaluate τ, the background spectrum is substracted from the Ps formation spectrum and the region after the prompt peak is fitted using equation 25. From the measured data the positronium lifetime is calculated to (142.8 ± 1.0) ns.

3.2.1 Positron-Positronium converter target

The positron-positronium converter is placed at the target holder in the test chamber (see figure 19). For the measurements in this work, a nanochannel-containing

sample made from p-type silicon (Si) with a (111)-crystal orientation is used. Previously to this work, several positron-positronium converter targets, as for example p-type Si with a (100)- or n-type Si with a (100)-crystal orientation, have been tested. The p-type (111)-sample turned out to be the most efficient one in terms of Ps production and its emission into vacuum[46].

The nanochannels are made by electrochemical etching with hydrofluoric acid (HF). The Si-sample is put into a solution, consisting of HF and ethanol. Between two electrodes, in contact with the solution, an etching current of 10 mA is applied for 15 min. Subsequently to the etching procedure, the sample is heated to 100°C in order to induce oxidation and to create a thin layer of silica on the internal surface of the nanochannels. The pore diameter of the etched nanochannels is expected to be in the range of 5-10 nm, their depth is around 1-2 µm. For a further description of the targets see [47].
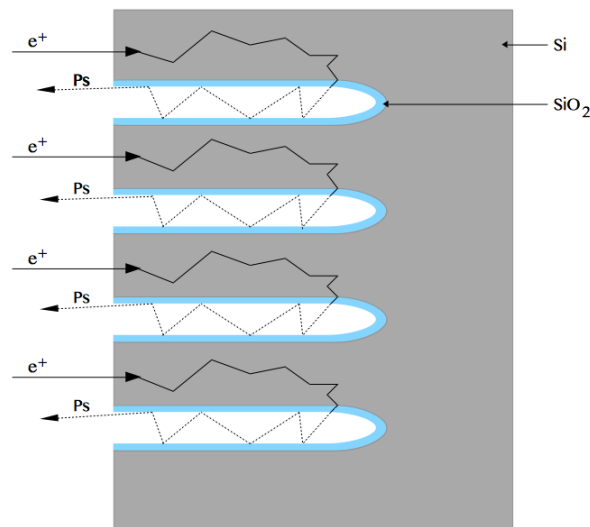
Figure 26: Schematic scetch of the Positron-Positronium converter target: Positrons implanted into the sample are likely to get to the interface between Si and SiO_2. The main part of Ps is formed within the bulk of the silica layer. The energy of Ps emitted into the nanochannels is lowered through inelastic collisions with the walls of the channels before they leave the sample.

The process of positronium formation within the nanochannelled targets can be explained as follows. Positrons, implanted into the sample, are likely to get to the interface between the p-type Si and the silica layer within their lifetime. As it is energetically more favourable, it is quite likely that they enter the silica [47]. In the bulk of the silica, positronium is formed. It diffuses to the surface and is

emitted into the nanochannels with an energy between 1 eV and 3 eV[48]. Thus, most of the created Ps is bulk-formed Ps, although there is also a small contribution of surface-formed Ps.

Positron implantation energies of 3.3 keV correlate to mean implantation depths of ≈142 nm, i.e. positrons are far from reaching the end of the nanochannels (their depth is around 1-2 μm). Before leaving the sample, the energy of Ps is lowered by inelastic collisions with the walls of the nanochannels. It is expected, that Ps has less kinetic energy, if the positrons are implanted with higher kinetic energies. As higher positron implantation energies also correlate to a higher positron implantation depth, formed Ps will experience more collisions with the walls of the nanochannels before it leaves the target[49].

3.3 LASER EXCITATION OF POSITRONIUM

In this section the results of the positronium laser excitation in the AEḡIS test chamber are presented. Parts of these measurements are published in Physical Review A [50].

For all measurements the magnetic field in the test chamber is set to 250 G and, as described previously (see section 3.2), positrons are implanted into the p-type sample with an implantation energy of 3.3 keV. The laser pulses are sent into the test chamber parallel to the target, with a time delay of 16 ns to the prompt annihilation peak (see figure 19).

3.3.1 *Excitation to n=3*

3.3.1.1 *Magnetic quenching*

After the formation of positronium on the converter target in the test chamber, an UV-pulse with a wavelength of λ_{UV}=205.045 nm and a power of 60 µJ is applied to excite o-Ps to the n=3 state. The magnetic field quenches this n=3-state and hence leads to a decrease in its population.

Figures 27 and 28 show the normalized SSPALS spectra with and without switching on the UV laser. They are created by an average of 15 shots from the accumulator, each containing 1000 pulses from the trap.

The spectrum with the UV-laser switched on shows a slightly smaller area beneath its curve, for the marked time window. Because the signal in this time window is mainly created by annihilating o-Ps, it decreases for the case of excitation and quenching (UV laser on) while the signal in the region of short annihilation times near the prompt peak rises. Note that the SSPALS spectra shown in figure 28 are normalized, so the rise in the prompt peak can not be observed.
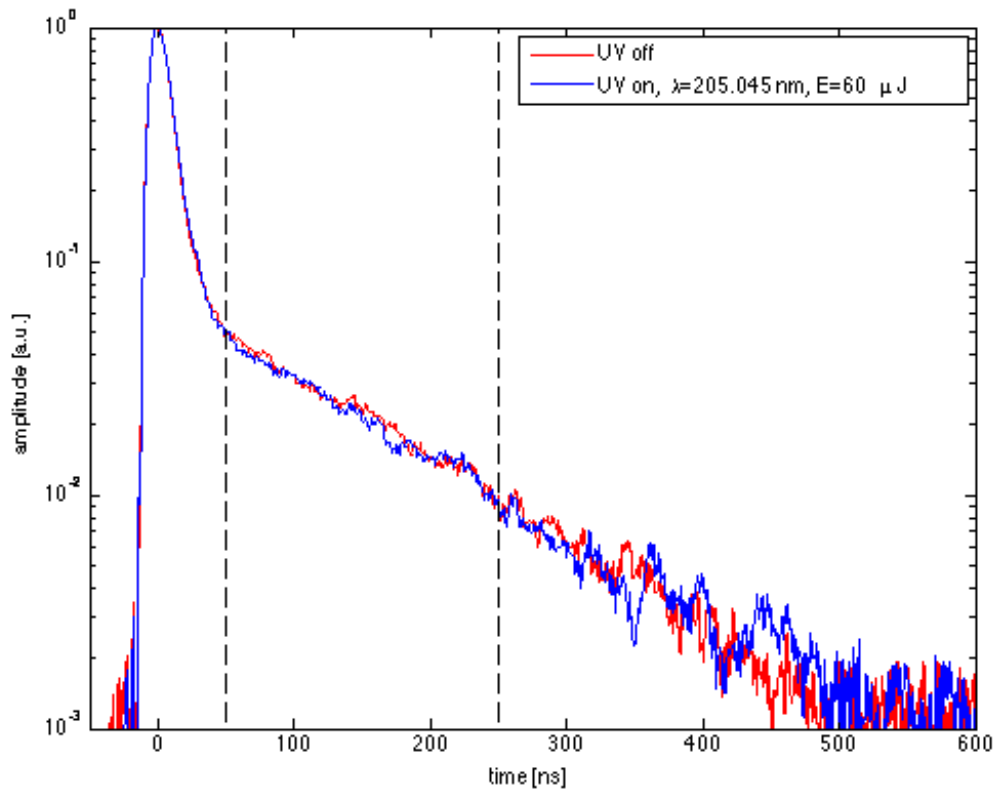
Figure 27: Normalized SSPALS spectra of Ps annihilation with UV-laser (λ_{UV}=205.045 nm) switched on (blue line) and switched off (red line). Each spectrum is composed by 15 shots from the accumulator. The dashed vertical lines indicate the range considered for the calculation of the S-parameter
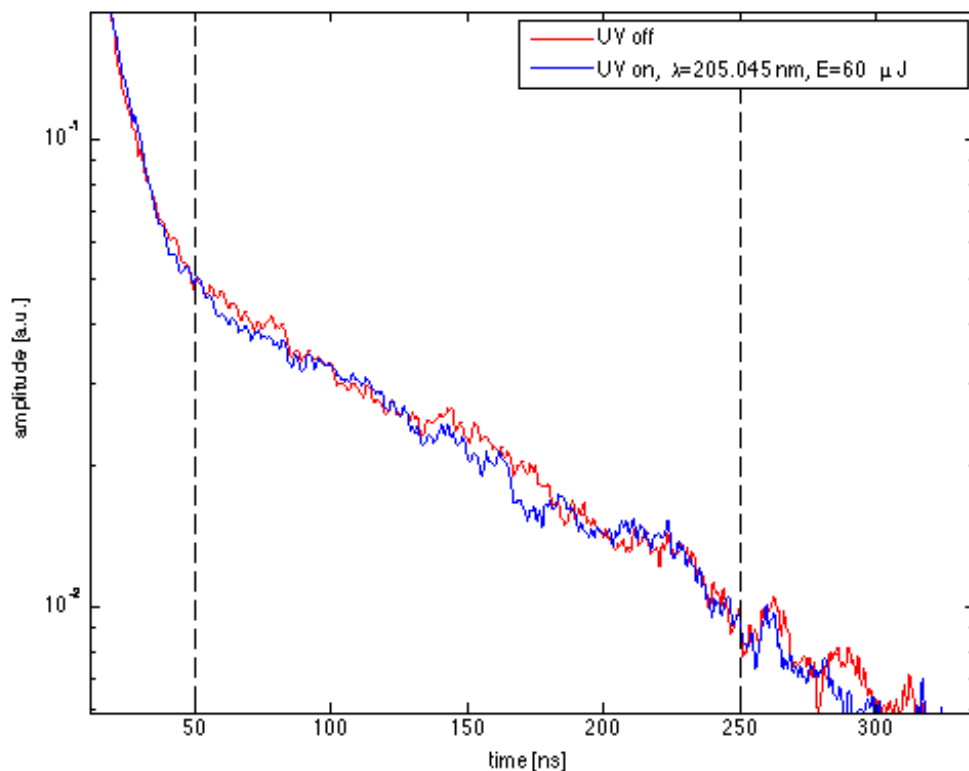
Figure 28: Zoom into the relevant section of figure 27. In this depicition of the data, the difference in the area beneath the two curves can be observed more clearly.

To evaluate the fraction of excited o-Ps, the S-parameter is calculated. It compares the areas under the curve of the lifetime spectra when excitation and photoionization or magnetic quenching is applied (A_{on}) to when it is not applied (A_{off}).

$$S = \frac{A_{on} - A_{off}}{A_{off}} \tag{26}$$

For the data depicted in figures 27 and 28, S has ben calculated to $(3.6 \pm 1.2)\%$ in the time window between 50 and 250 ns. The error is calculated by the standard deviation of the 15 shots.

3.3.1.2 *Photoionization*

For the photoionization of the n=3-state of o-Ps a second intense IR-laser pulse is superimposed to the UV-pulse. Temporal and spatial settings are the same for both pulses. The time delay to the prompt peak is 16 ns, as it is in the case of magnetic quenching. The IR-pulse has a wavelength of λ_{IR}=1064 nm and an energy of 55 mJ. The magnetic field of 250 G in the sample region is still switched on, to keep the same conditions of transport and focus as used before during the quenching measurements.
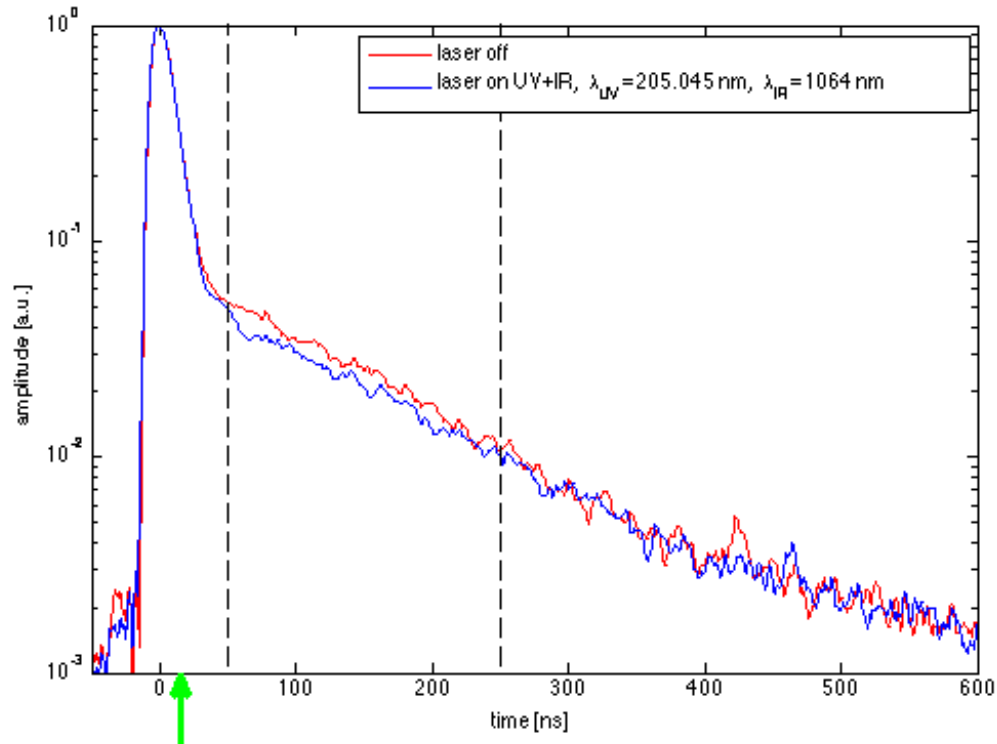
Figure 29: Normalized SSPALS spectra of Ps annihilation with UV-laser (λ_{UV}=205.045 nm) and IR-laser (λ_{IR}=1064 nm) switched on (blue line) and off (red line). Each spectrum is composed by 15 shots from the accumulator, containing 1000 pulses from the trap. The dashed vertical lines indicate the range considered for the calculation of the S-parameter (as defined in figure 27). The green arrow indicates the temporal position of the laser pulse.

Figure 29 shows the two SSPALS spectra. One is recorded having the UV- and the IR-laser switched on, for the other one, both are turned off. The green arrow indicates the temporal position of the laser pulse.

The IR-pulse photoionizes the n=3-state of o-Ps and leads to the same effect as the magnetic quenching, i.e. a decrease in the population of o-Ps. The area under the curve in the range 50-250 ns decreases for the case that the UV- and the IR-laser are both switched on. From the data, the fraction of photoionized Ps can be calculated to S=(15.5 ± 1.3) %. The error is again given by the standard deviation of the 15 shots.

In comparison to the case of magnetic quenching, the S-parameter for photoionization is more than four times higher. This result does not mean that for the case of magnetic quenching less Ps is excited into the n=3 state. It just shows that photoionization is more efficient than quenching when it comes to depopulating this o-Ps energy level.

Theoretical calculations for the value of the S-parameter, when magnetic quenching and photoionization is applied, have been calculated beforehand by Villa, Castelli and Caravita. For quenching, with a field of 250 G and for ideal spatial and temporal overlap of the laser spot and the Ps cloud, a maximum excitation efficiency of 17% is estimated. In the case of photoionization the theoretical maximum signal should be S=93% [50]. The ratio between the theoretical and the experimental efficiency is 0.21 for magnetic quenching and 0.17 for photoionization, indicating an experimental efficiency of 17-21%.

To validate if the applied laser power is sufficient to excite a maximum number of Ps, the energies of the UV- and the IR-laser are scanned in a range from 0 to 80 μJ (UV) and 0 to 50 mJ (IR). The different S-parameters corresponding to all energy values set, are obtained by taking the average of 15 shots from the accumulator, each containing 1000 pulses from the trap. During the variation of the energy of the IR-pulse, the UV-pulse is kept constant at an energy of 60 μ J and a wavelength of λ_{UV}=205.045 nm. Vice versa, during the variation of the UV energy, the IR-pulse is kept constant at an energy of 55 mJ and a wavelength of λ_{IR}=1064 nm.

In the case of altering the IR-energy, S increases steeply for low energies, then reaches a plateau quickly and saturates (see figure 30). Around an energy of 15 mJ, saturation is reached. Since the excitation measurement was done with an IR-energy of 55 mJ, the S-parameter would not get any bigger by applying a higher IR-energy.

When the UV-energy is varied, S increases fast initially, then it reaches a plateau or a much slower linear increase (see figure 31). This behaviour can be explained by the Gaussian profile of the laser pulse. The initial fast increase of the S-parameter is caused by transitions excited by the center of the pulse, while the slow increase at higher energies is induced by transitions excited by the tails of the pulse. In general the same argument is valid for the variation of the photon energy of the IR-laser. But since the diameter of the IR-laser spot (d_{IR} ≈8 mm) is larger than the diameter of the UV-laser spot (d_{UV}=4-6 mm), all Ps excited to n=3 by the UV-laser is expected to be close to the central part of the IR-laser spot.

The data depicted in figures 31 and 30 also shows that the IR-laser has no direct influence on the excited fraction of positronium. If the IR-energy is set to

Figure 30: Measured values for the S-parameter (as defined in figure 27) as a function of the energy of the IR-laser. The arrow marks the energy used for the excitation measurements (data presented in figure 29). The vertical errorbars are given by the standard deviation of the measured values, the horizontal errorbars are given by the spread in energy of the laser
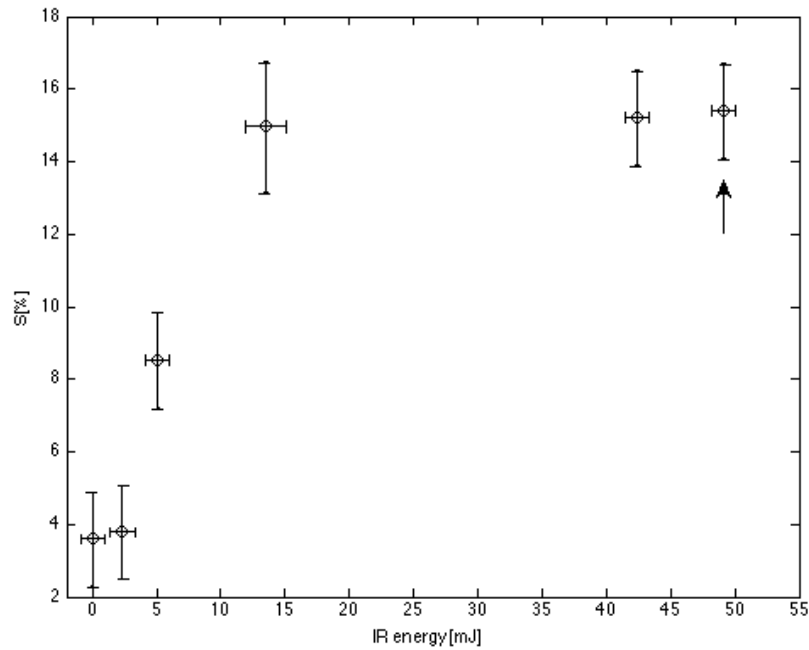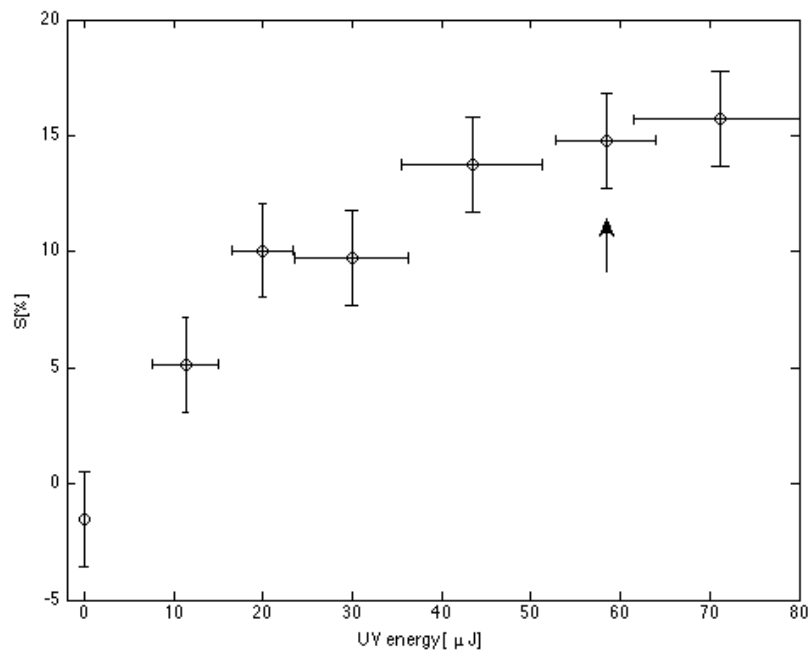

Figure 31: Measured values for the S-parameter (as defined in figure 27) as a function of the energy of the UV-laser. The arrow marks the energy used for the excitation measurements (data presented in figure 29). The vertical errorbars are given by the standard deviation of the measured values, the horizontal errorbars are given by the spread in energy of the laser

zero, S is still around 4%, while for an UV-energy of zero, there is no excited positronium at all (S=0%). This validates, that the process works, as it was theoretically expected. The excitation of positronium itself is enabled by the UV-laser, the IR-laser only makes the excitation signal clearer.

3.3.1.3   *Linewidth of the 1^3S - 3^3P Ps excitation*

To obtain the linewidth of the 1^3S - 3^3P Ps excitation the UV-wavelength is scanned in a range from 204.8- 205.2 nm with an energy set constantly to 60 µJ. While the IR-pulse is kept constant at a wavelength of 1064 nm and an energy of 55 mJ, the corresponding SSPALS spectra are taken.
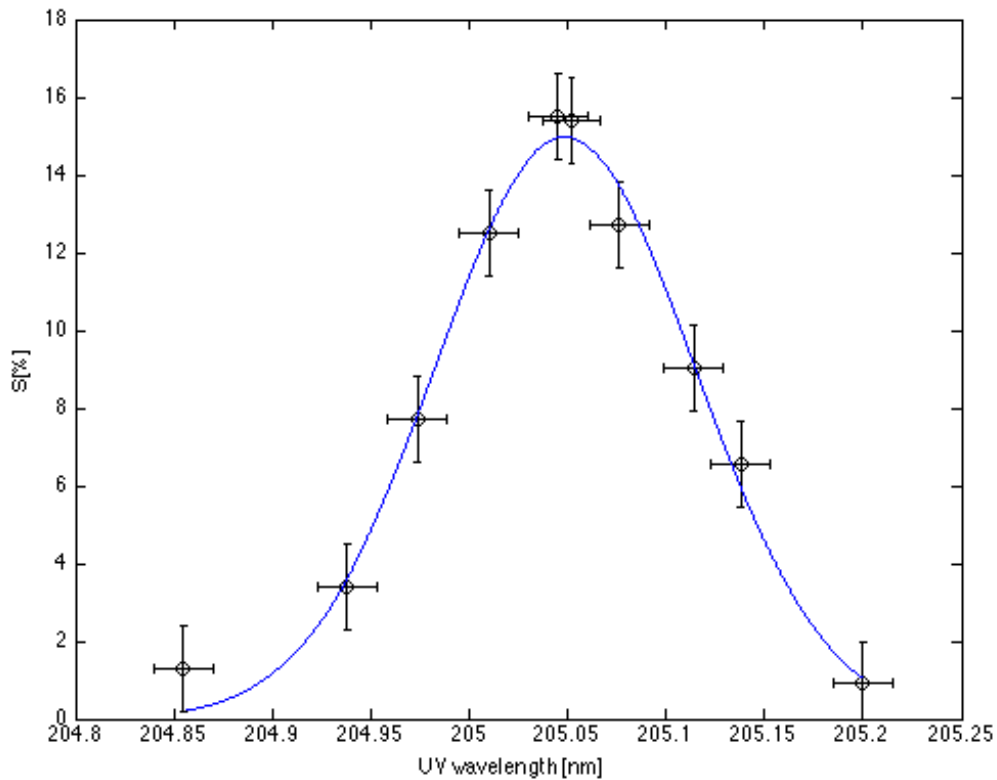
Figure 32: Linewidth of the 1^3S - 3^3P Ps excitation. Each datapoint is obtained by taking the average of 15 shots. The vertical errorbars are calculated by the standard deviation of S, the horizontal errorbars result from the variation of the laser output. The data is fitted by a Gaussian distribution.

Figure 32 shows the obtained S-parameter for each wavelength set. Each datapoint is an average of 15 shots from the accumulator, containing 1000 pulses from the trap. The errorbars of the S-parameter datapoints in the y-axis correspond to the standard deviation, the x-axis errorbars correspond to the accuracy

of the wavemeter that is used for the scan of the UV-wavelength (Avantes Ava Spec-3648-USB2, accuracy=±0.02 nm).

From the measurement, it is clear that there is a UV-wavelength, that maximes the value of the S-parameter. The largest S-parameter found, is (15.5±1.3)% with a corresponding resonance wavelength of (205.05 ± 0.02) nm, which is in good agreement with previous simulations[30]. The other values around the resonance wavelength of 205.05 nm show a broadened peak and are fitted by a Gaussian distribution. The linewidth of the transition is mainly a consequence of Doppler broadening induced by positronium atoms moving along the axis of the laser pulse, parallel to the surface.

For this reason, it is possible to obtain the temperature, and consequently the mean velocity of the Ps atoms in this direction, from the Doppler peak. The temperature can be found from the evaluation of equation 17. Once knowing the temperature the mean velocity in the transversal direction can be obtained from:

$$\frac{1}{2}m_{Ps}\left\langle v_x^2 \right\rangle = \frac{3}{2}kT \tag{27}$$

Where $\left\langle v_x^2 \right\rangle$ is the mean square velocity. The FWHM according to equation 17, can be evaluated from the Gaussian fit of the Doppler broadened peak to $\Delta\lambda = 0.15 \times 10{-9}$ m. For the resonance wavelength $\lambda_0 = 205.05 \times 10^{-9}$m is inserted. For the mass of the positronium atom, twice the electron mass, $2 \times 9.11 \times 10^{-31}$ is used.

The calculation results in a positronium temperature of $\approx(1150\pm150)$ K and a mean velocity in the range of 10^5 m/sec. Thus the positronium atoms leaving the converter target are far from being thermalised. The linewidth of the excitation to n=3 (see figure 32) has been estimated to approximately $2\pi\times470$ GHz, while the bandwidth of the laser is only $2\pi\times48$ GHz. By the convolution of the two spectral distributions, one can expect an excitation efficiency of up to 10 %. It can be concluded, that the main limiting factor for the efficient excitation of Ps is given by the limited laser bandwidth compared to the Doppler profile.[50]

If positronium leaving the target would be slower, the Doppler broadening of

the line would be smaller. Consequently a laser of the same bandwidth could address and excite a larger fraction of Ps.

Colder positronium can be created by increasing the positron implantation energy. It is implanted deeper into the sample and experiences a higher number of collisions. Therefore it looses more of its kinetic energy before it leaves the target.

3.3.2 *Excitation to Rydberg-states*

In order to excite positronium to Rydberg states the wavelength of the IR-pulse is varied in a range $\approx$1684-1708 nm, corresponding to the energy levels n=17 to n=15. The energy of the IR-pulse, the UV-wavelength and the UV-energy are kept constant at E_{IR}=55 mJ, λ_{UV}=205.049 nm and E_{UV}=60 µJ.
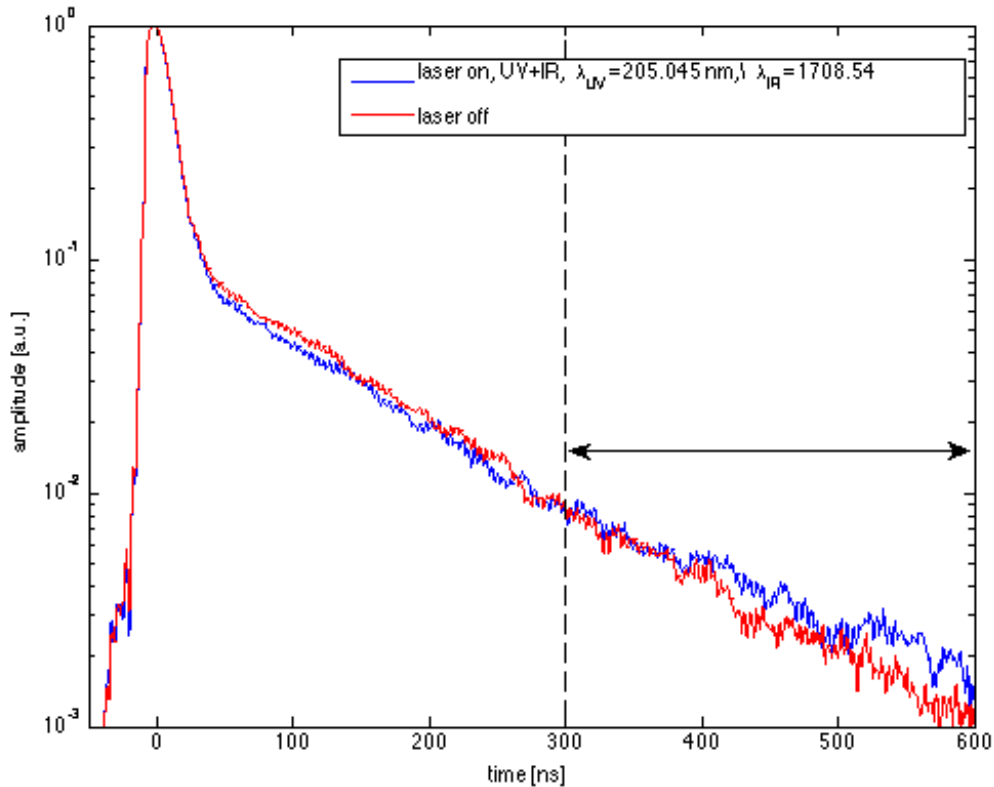
Figure 33: Comparison of SSPALS spectra of Ps annihilation with UV-laser (λ_{UV}=205.045 nm) and IR-laser (λ_{IR}=1708.54 nm) switched on (blue line) and off (red line). Each curve is composed by an average of 15 shots from the accumulator, containing 1000 pulses from the trap. The S-parameter is caculated for the time window marked by the black arrow.

Figure 33 shows a comparison of two SSPALS spectra, switching the laser (UV+IR) on and switching it off. Each curve is composed by an average of 15 shots from the accumulator, containing 1000 pulses from the trap.

In the time window between 50 ns and 250 ns, the S-parameter decreases if the lasers are switched on. On the contrary, in the time window between 300 ns and 600 ns, the S-parameter increases. This is due to the fact, that by excitation to Rydberg states the positronium lifetime increases up to the milliseconds scale. Therefore less o-Ps in ground state is left which produces annihilation signals in the 50-250 ns time window. On the other hand the signal corresponding to longer Ps lifetimes (300-600 ns) produced by Rydberg positronium gets higher. Note that the increased signal in the time window, marked in figure 33, is not created by the annihilation signal of Rydberg-Ps in vacuum, but by its annihilation as it reaches the walls of the test chamber.

For the time window 300 ns to 600 ns the S-parameter has been calculated to (17.8 ± 2.0) %.
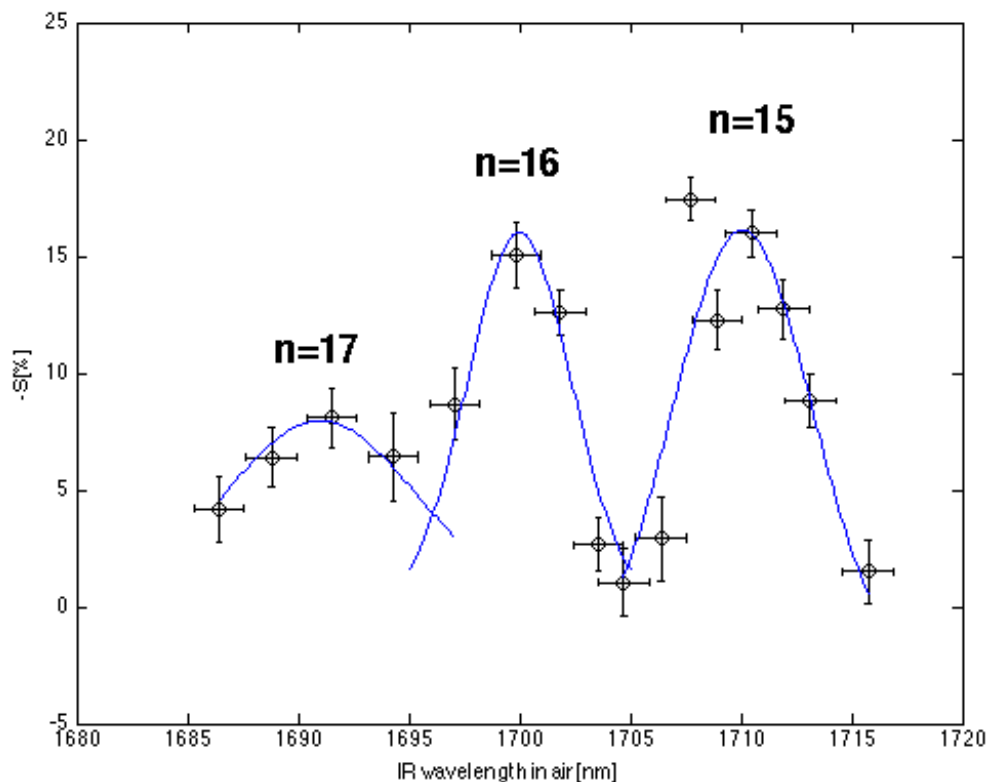
Figure 34: Measured S-parameter as a function of the IR-wavelength. Each point is an average of 15 shots from the accumulator, containing 1000 pulses from the trap. The horizontal errorbars are given by the standard deviation of S, the vertical errorbars result from the variation of the laser output.

Figure 34 shows the S-parameter in dependence of the IR-wavelength. Each point is an average of 15 shots. The n=15 and the n=16 transition are clearly dis-

tinguishable, while the excitaion to n=17 is only vaguely recognizable from the acquired data.

This can be explained by the fact, that at higher states different n-manifolds overlap in a continuum of energy levels.

The datapoints are fitted by three independent Gaussian distributions in the ranges of the three transitions. The results of the measurement are in good agreement to a spectroscopic survey, using the n=2 level as intermediate step carried out by Cassidy et al.[29].

The VEPAS laboratory of Como is part of the AEḡIS collaboration. As the set-up of their positron beam is geared to material research, the measurements of the carbon nanoparticle filters were conducted at their laboratory.

For the first set of samples the Doppler broadening of the annihilation line is measured, as well as the positronium formation. The second set of samples is analyzed by Doppler broadening spectroscopy only. In both cases the data are evaluated by the VEPFIT program. For more information on this software see [51].

3.4.1 *Measured samples*

3.4.1.1 *Filter samples AVL*

The samples described in the following section are air monitoring filters in combustion engine test systems of the company AVL (Anstalt für Verbrennungskraftmaschinen List).

Of particular interest for the company is to study the behaviour of the carbon particles in the micropores of the filter. The carbon adsorption profile and the interfaces between carbon and the filter shall be observed to conclude the penetration depths of carbon into the samples.

Analyzed were two sets of samples, microstructured nickel and quartz tissue filters, each differing in their carbon nanoparticle loadings.

<u>Microstructured nickel filter:</u>

- 100% pure electrodeposited Nickel

- microstructur: 2000 holes/ 0.0254 m each of a radius r=3.75×10^{-6} m

- thickness t=6×10^{-6} m

- diameter d$\approx$ 2.5 cm

- density of the the filter material nickel: ρ_{Nickel}=8.908 g/cm^3

- average density of the microstructured sample: $\bar{\rho} \approx 6.47$ g/cm^3 calculated from $\bar{\rho} = (1-p)\rho_{Nickel}$, with porosity $p_{nickel} = \dfrac{V_{void}}{V_{total}}$ (where V_{void} is the pore volume)

The company provided one blank nickel filter, to measure it as a reference, as well as a nickel filter penetrated with carbon particles. The thickness of the carbon layer is assumed to be < 1 μm. For the density of the carbon nanoparticles a value of ≈ 1.95 g/cm^3, as for amorphous carbon is assumed.
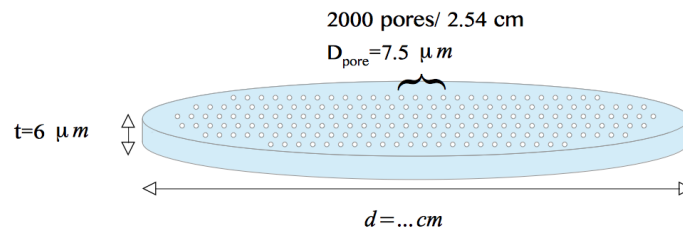
Figure 35: Schematic drawing of the nickel filter sample

Quartz tissue filter:

- Pallflex Tissuquartz filter 2500 QAT-UP

- tissue made of 100% pure quartz (SiO$_2$) filaments of ≈432 μm thickness

- areal density $\rho_{area} = 5.8$ g/cm^2, bulk density $\rho_{bulk} = 0.134$ g/cm^3

- porosity $p_{quartz} = 95\%$ (calculated with a quartz density of $\rho_{quartz} = 2.6$ g/cm^3)

Analyzed were eight quartz tissue filters with carbon loadings, differing in the size of the carbon particles and carbon loading times as well as one pure filter without loading as a reference. The silica quartz tissue filters are made by the Pall corporation and are used as air monitoring filters. The carbon nanoparticles were infiltrated by a flow of carbon nanoparticles taken from an aerosol. The density of the nanoparticles has been estimated to 1.8 g cm^{-3} (as it was later found to be the value which is used often in literature[52] for amorphous carbon rather than 1.95 g cm^{-3}, as used for the previous measurements). Figure 37 shows a greatly enlarged shot of the quartz tissue.

Table 2: Tissue quartz filters

Sample Nr.	size of carbon particles [nm]	loading time [min]
1	55	5
2	55	15
3	80	5
4	80	15
5	120	1
6	120	4
7	41	7

Figure 36: Image of the quartz tissue samples with different loadings of carbon nanoparticles. There are noticeable changes in the degree of black between the samples. This is presumably due to the different nanoparticle dimensions as well as different carbon concentrations.
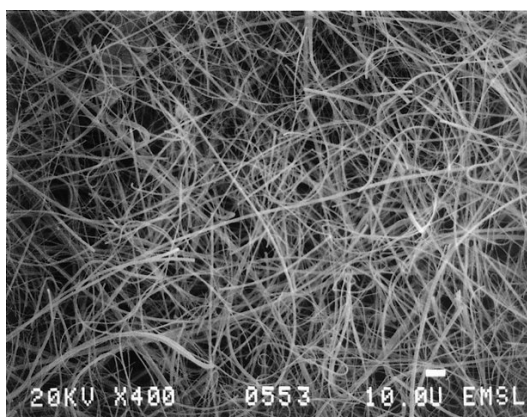
Figure 37: Image of the blank quartz tissue filter

3.4.1.2 *Positronium formation reference samples*

To calculate the $F_{3\gamma}$-fraction for the measured samples according to formulas 22 and 23 one needs reference samples in order to define values of the total area and peak area corresponding to 100% and 0% Positronium formation $T_{1,0}$ and $P_{1,0}$.

Aerogel 85

Aerogels are high porousity materials. They can exhibit the lowest bulk density of any known solid with a fraction of up to 99.8 of their volume consisting of pores. In this work Aerogel85 is used as a reference sample for 60 % Ps formation. For further information see [53].

- $\rho_{aerogel}$=85 mg/ cm^3

- porosity $p_{aerogel}$= 96

- pore diameter $d_{pore,Ae}$=25 nm

- pore surface area $A_{surface,Ae}$=660 m^2/g

- maximum Ps-production: $\approx$ 60%

Mono UTHClAl

- pure silica with aluminium layer on top

- ρ_{mono}=101 mg/ cm^3

- pore diameter $d_{pore,mono}$=5 nm

- porosity p_{mono}= 60

- pore surface area $A_{surface,mono}$=703 m^2/g

- minimum Ps-production: $\approx$ 17%

3.4.2 *Microstructured nickel filter*

To get a first idea how deep the positrons are implanted into the samples, the implantation profiles for nickel and carbon are calculated according to equation 8 for each positron implantation energy. The peak values of these distributions (see equation 10) correspond to the mean positron implantation depths depicted in figure 38.

The values for the parameters used to calculate the mean positron implantation depth can be found in subsection 1.8. The positron implantation energy is varied in a range of 0.1- 17.1 keV, as this is the possible energy range of the experimental set-up of the VEPAS laboratory.

As the mean density of the amorphous carbon layer is lower than the density of the porous nickel filter, positrons are implanted deeper into the carbon for the same implantation energies.

These theoretical calculations of the positron implantation depth before the measurements are a useful tool. Using the gained information, it can be estimated beforehand which positron implantation energies should be set. Also datapoints from following measurements can be assigned to certain regions in depth of the sample.

The exact thickness of the carbon layer has not been known exactly in the forefront. For a thickness of the carbon layer less than 1 μm, it can be deduced from the positron implantation profiles, that positrons should be implanted into the region of the nickel substrate for energies higher than ≈11 keV.

For the measurements of Doppler broadening spectroscopy, the positron annihilation peak is recorded and the S-parameter is calculated from the data. The positron implantation energy is varied in the range 0.1 keV - 17.1 keV in 38 steps. To improve the statistics each sample is measured twice. Note that in this case the S-parameter corresponds to the central area beneath the annihilation peak. It has nothing to do with the previously mentioned S-parameter of positronium excitation.
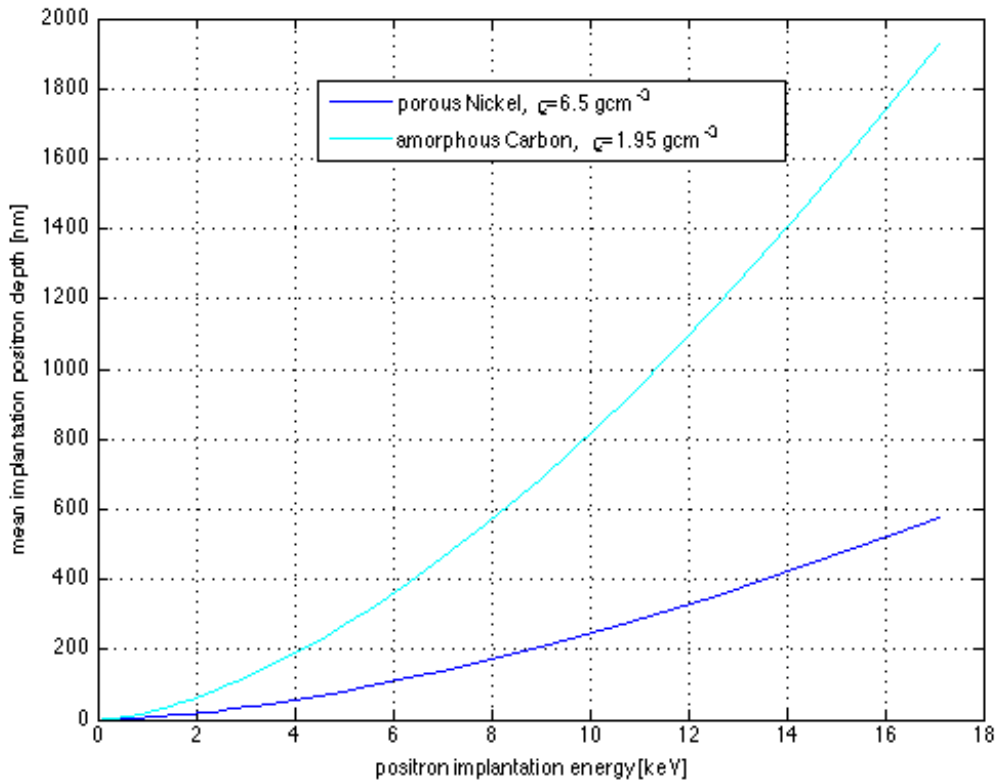
Figure 38: Mean positron implantation depth (according to equation 10) for nickel and carbon in dependence of the positron implantation energy derived from the corresponding implantation profiles.

Figure 39 shows the S-parameter of the nickel filter sample with (black curve and datapoints) and without (blue curve and datapoints) carbon nanoparticles deposited on top.

The values and the corresponding fitted curve of the pure nickel sample show a behaviour expected for specimen consisting of only one layer of the same material: The fit is made up by one curve with consistent parameters. There are no rapid changes in the slope. Using the slope of the fit, it is possible to calculate the positron diffusion length via VEPFIT. For the pure nickel sample it is calculated to $L_{pos,Ni}$= (170 ±2) nm. As the positron diffusion length in defect free nickel is around 150 nm[55], there seem to be no defects in the present sample, within the limits of the technique. It seems that also the micropores of the sample do not really influence the positron diffusion length.

To fit the nickel-carbon datapoints, three layers of material are assumend: carbon, the interface between carbon and nickel and nickel. This gives minimal values for the statistical deviation and thus the best possible fit. In contrast to the data
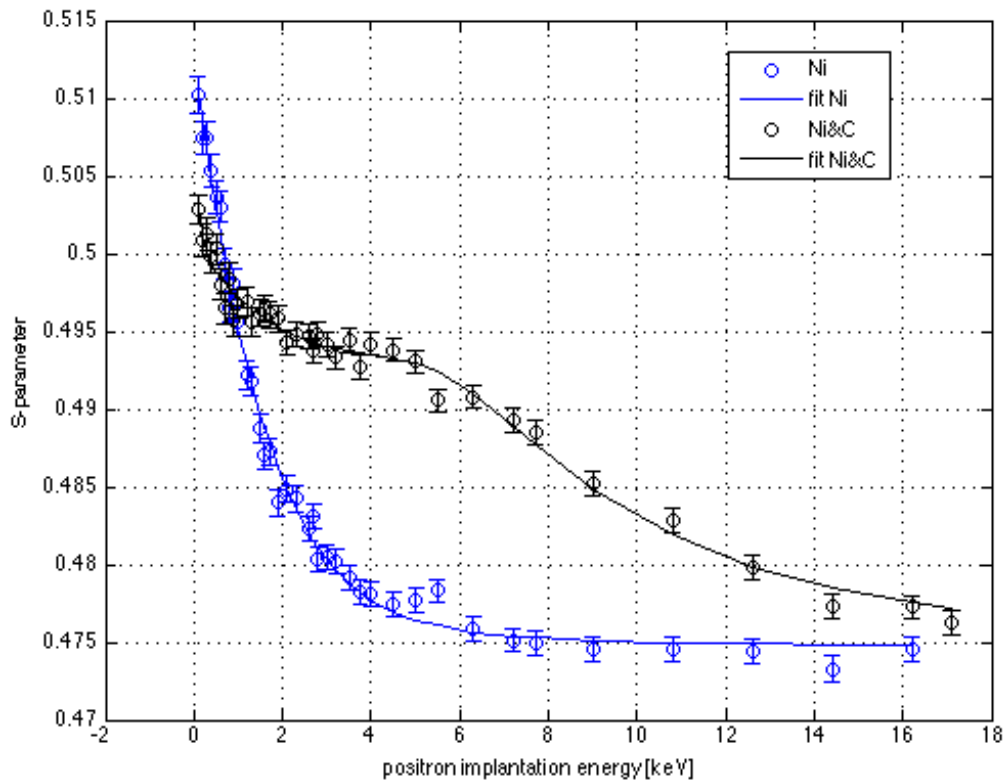
Figure 39: S-parameter as a function of the positron implantation energy for the nickel and the nickel-carbon sample. The continuous curves through the datapoints represent the best fits proposed by VEPFIT. The errorbars correspond to the standard deviation of the values. The measurements were carried out in collaboration with Lisa Marx. The same figure can be found in her Master Thesis[54].

obtained for the pure nickel sample, the fit of the nickel-carbon sample, shows an inflection point. This behaviour is seen in the energy region between 4 and 8 keV and indicates an interface in this region.

The value for the positron diffusion length in carbon is determined to $L_{pos,C}= (44 \pm 2)$ nm.

Within the program, it is also possible to calculate the thickness of different layers. The thickness of the carbon layer is computed to $t_C= (620 \pm 20)$ nm.

Since most of the parameters (number of layers, density, thickness, positron diffusion length and S-parameter) used for this calculations, could only be estimated, this result can only represent a very rough estimation.

The data was fitted, making the assumption, there is a third layer consisting of the interface region between carbon and nickel. In fact, to verify the existence of an interface the statistics of the measurement are not high enough. Although the used fit showed the lowest statistical deviation, also the errors of other fits using

two layers were not significantly higher.

In the next step, the positronium formation is measured. In addition to the two filter samples provided by AVL, four other samples were measured. The two silicon samples are the same nanostructured samples as used in the AEḡIS set-up. The p-type silicon sample shows a (111) crystal orientation, while the n-type sample shows a (100) crystal orientation. The Aerogel85 and the MonoUTH were provided by the como VEPAS laboratory, as reference samples.
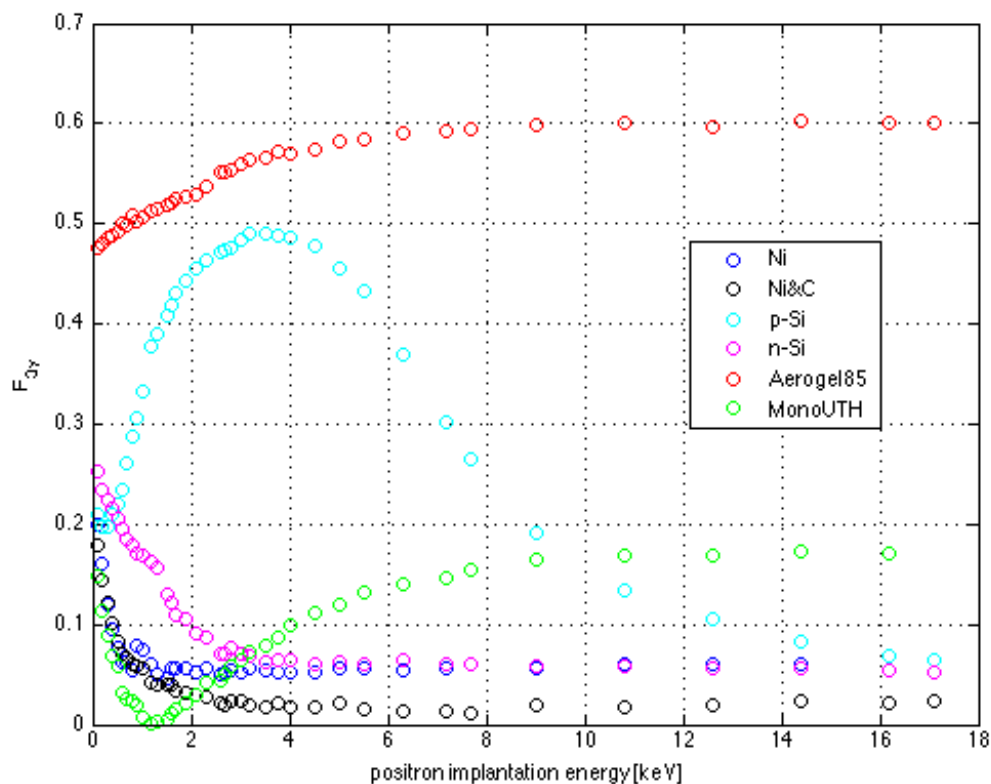
Figure 40: $F_{3\gamma}$-fraction Nickel filter, Nickel filter with Carbon and reference samples MonoUTH & Aerogel85. The measurements were carried out in collaboration with Lisa Marx. The same figure can be found in her Master Thesis[54].

The relevant parameter concerning positronium formation is the $F_{3\gamma}$-fraction. In figure 40 the $F_{3\gamma}$-fraction of the samples is depicted. The 100% Ps formation reference sample, Aerogel85, shows a maximum of approximately 0.6 in its $F_{3\gamma}$-fraction for energies higher than 9 keV. The 0% Ps formation reference sample, MonoUTH, has its maximum of approximately 0.17 in the same range of energy. The pure Nickel filter as well as the filter with the carbon layer, show insignificant values of positronium formation. The maximum values of the $F_{3\gamma}$-fraction can be

found to be 0.06 for the nickel sample and 0.02 for the nickel-carbon sample. However, it is noticeable that, even for very high positron implantation energies higher than 16 keV, where the positrons should have reached the bulk of both samples, their $F_{3\gamma}$-fraction values never converge. By this fact, it could be assumed that the carbon particles diffuse very deep into the sample, approximately 450 nm. This value is limited by the maximum positron implantation energy reached by the set-up.

To confirm the presented results, further measurements using higher statistics and different techniques are necessary. For example a coincidence measurement, where certain areas of the sample can be measured more precisely would be of great interest.

In order to get a more appropriate fit of the data further details on the samples, as the exact density of the carbon layer and its thickness, as well as the deposition method, is inevitable. Further, it would be interesting to remove the carbon layer and measure it without the nickel substrate.

3.4.3 *Quartz tissue filter*

All filters of the second set of samples are made of quartz tissue. The company provided eight samples, each differing in time of carbon deposition and size of the carbon nanoparticles. Within the measurements, the positron implantation energy is varied for each sample between 0.1 keV and 17.1 keV, in around 30 steps. Doppler broadening spectroscopy measurements are conducted for all samples seperately.

In order to get an idea of the behaviour of positrons and thus the S-parameter, within the carbon layer, without the influence of the filter media, a carbon reference sample is measured as well. It consists of a powder sintered into a cylindrical pellet of 2 cm in diameter and 7 mm in thickness. The diameter of the carbon nanoparticles within the sample is known to be $\approx$500 nm.
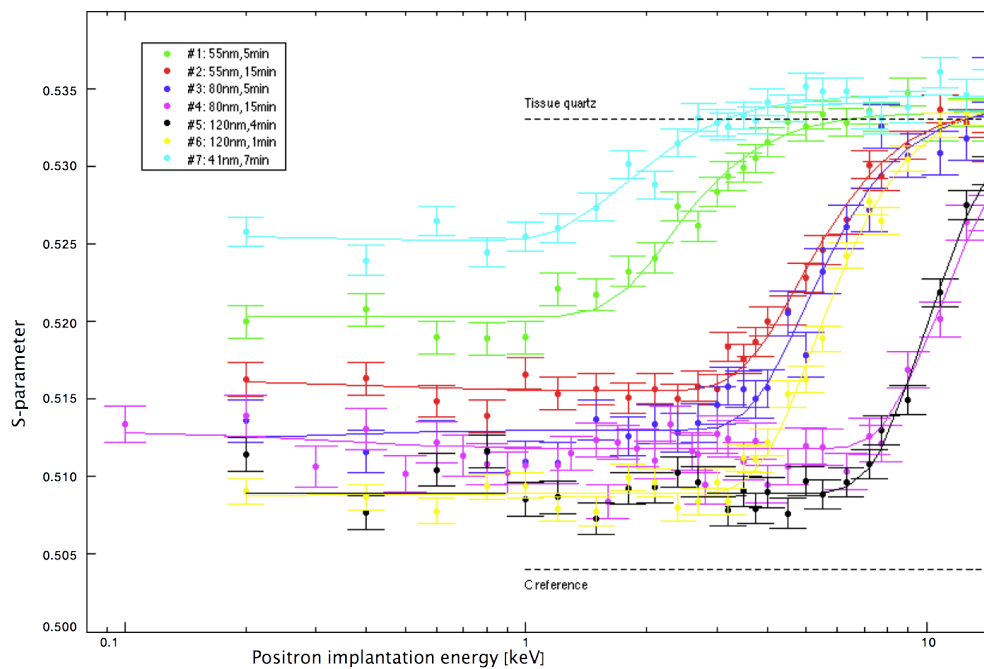
Figure 41: S-parameter in dependence of the positron implantation energy for the samples Nr. 1-7. The black, dashed horizontal lines indicate the measured S-parameter of the pure quartz tissue filter as well as a carbon reference sample. The continuous curves through the datapoints represent the fits according to the VEPFIT program. The errorbars represent the statistical standard deviation of the values.

Figure 41 shows the measured values of the S-parameter for different positron implantation energies. The two black, dashed lines indicate the values of the S-parameters of the blank quartz tissue filter as well as the carbon reference sample. The data clearly indicates the existence of two different environments where the positrons annihilate. On the left, at low positron implantation energies, there is a first layer of quartz tissue highly infiltrated with carbon. Here the datapoints show a decrease of S-parameter, going into the direction of the value, measured in the carbon reference sample.

Into the direction of higher positron implantation energies, positrons reach deeper layers of the sample. They get into the region of quartz tissue free from carbon. The datapoints in this energy range approach the value of the S-parameter of the blank quartz tissue sample.

Comparing sample pairs with the same size of the carbon nanoparticles, as samples Nr. 3 and 4, or Nr. 5 and 6, it can be concluded qualitatively, that the onset of the S-increase is shifted to higher energy values and consequently the

thickness of the first layer, increases with the duration of the deposition process. In figure 42 it can be seen, that the width of the first plateau is larger for sample Nr. 5, with a carbon deposition time of 4 minutes than for sample Nr. 6, with a carbon deposition time of 1 minute. As the diameter of the carbon nanoparticles for both of them is 120 nm, they are comparable. Also the data depicted in figure 43 verifies this correlation between the duration of the process and the width of the first plateau. This width is bigger for sample Nr. 4, with a deposition time of 15 minutes, than for sample Nr. 3 with a deposition time of only 5 minutes. The diameter of the nanoparticles on both of them is 80 nm.
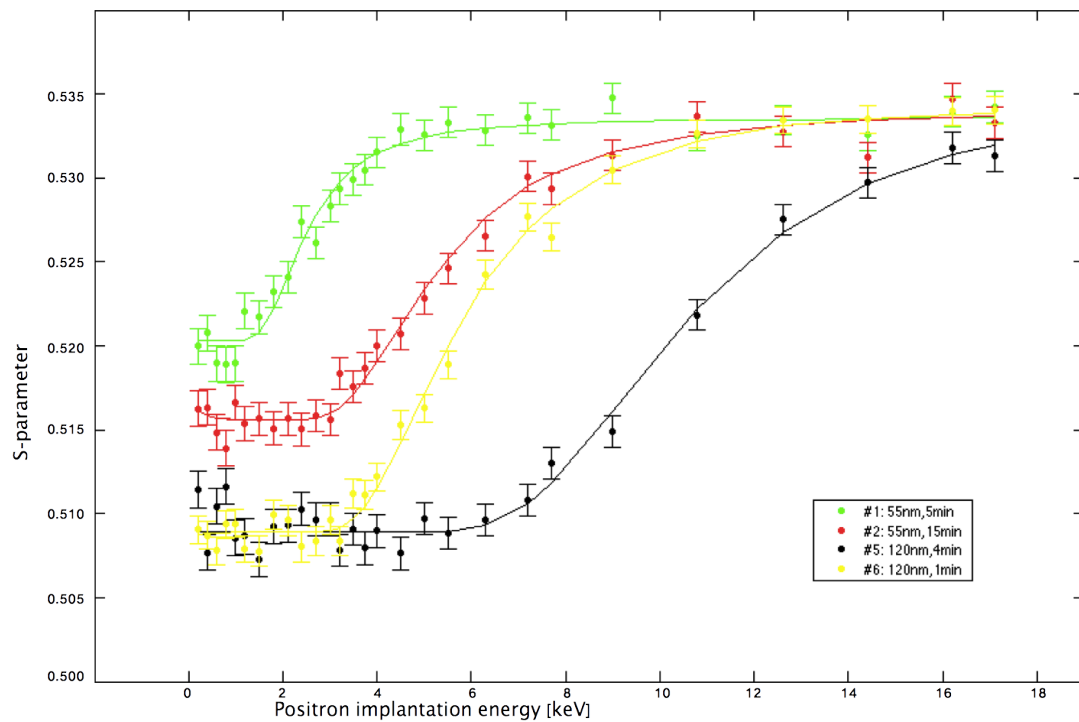
Figure 42: S-parameter in dependence of the positron implantation energy for the samples Nr. 1, 2, 5 and 6. The continuous curves through the datapoints represent the fits according to the VEPFIT program. The errorbars represent the statistical standard deviation of the values.
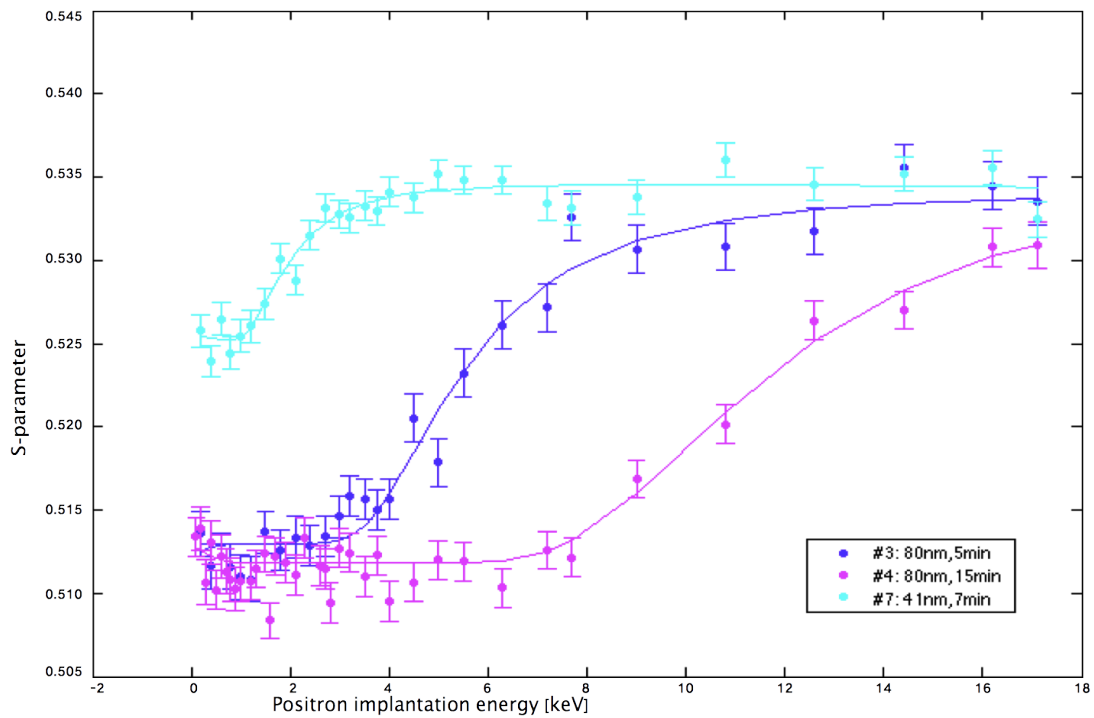
Figure 43: S-parameter in dependence of the positron implantation energy for the samples Nr. 3, 4 and 7. The continuous curves through the datapoints represent the fits according to the VEPFIT program. The errorbars are obtained statistically by the standard deviation of the values.

Next, the dependence of the S-parameter on the dimension of the nanoparticles will be considered. By comparing samples Nr. 1, 3, 5 and 7 (as they have similar carbon deposition times) the S-parameter at low values of the positron energy seems to increase as the dimension of the nanoparticles decreases as it is depicted in figure 44 The reason for this behaviour is, that smaller particles have higher ratios of surface to volume. At the surface, the defect density is higher than in the bulk of the material. Positrons trapped in defects are more likely to annihilate with the low momentum, valence electrons associated to the defect. The Doppler peak of the 511 keV annihilation line gets narrower and consequently the S-parameter increases (see section 1.11.3).
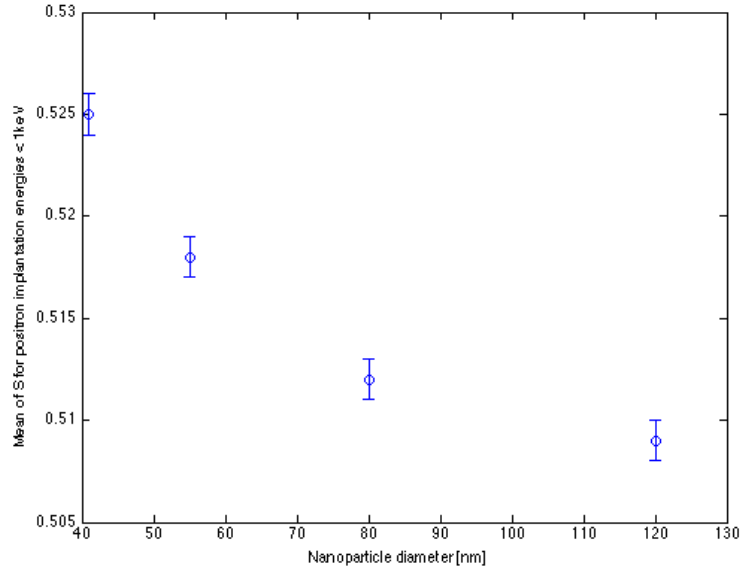
Figure 44: Mean value of the S-paramater as a function of the diameter of the nanoparticles for positron implantation energies <1keV.

In the region of low positron implantation energies, there is a gap of $\Delta S \approx 0.005$ between the S-parameter values of samples Nr. 1 and Nr. 2 (see figure 42). From this fact, it can further be concluded, that the S-parameter also depends on the carbon deposition time and therewith the carbon concentration in the quartz tissue. This conclusion is due to the fact that the two samples exhibit the same particle size.

In order to estimate the carbon concentration of the first layer, a model based on two assumptions is used:

- The value of the S-parameter in the first layer (S_1) depends on the carbon concentration (p) in the tissue and is calculated as a balance between the values S_Q (S-parameter of the blank quartz tissue) and S_{NP} (S-parameter of the carbon nanoparticles) as follows:

$$S_1 = pS_{NP} + (1-p)S_Q \tag{28}$$

- The value of S_{NP} depends on the annihilation of positrons in the bulk and the surface of the nanoparticles:

$$S_{NP} = \alpha S_C + (1 - \alpha) S_{surf} \tag{29}$$

S_C and S_{surf} are the S-parameters of the carbon nanoparticles within the bulk and at the surface, α is the probability for a positron annihilation in the bulk region of the carbon nanoparticle.

The value of α is dominated by the ratio of the diameter (d) of the nanoparticles and the positron diffusion length (L_C) in carbon and is described by the Langevin function[56]:

$$\alpha = \coth(\frac{d}{L_C}) - \frac{L_C}{d} \tag{30}$$

The positron diffusion length L_C is assumed to be 5 nm, since this is in the range of typical values in literature[57][58].

As there are still too many unknown parameters in equations 28 and 29, the carbon concentration p of samples Nr. 5 and Nr. 6 is estimated to 0.9. The reason why such a high value of carbon concentration is assigned to samples Nr. 5 and Nr. 6 is mainly that they both show the lowest S-parameter of all samples within their first layer (see S_1 in table 3). Another indication for a rather high carbon concentration is that they show the darkest degree of black from all samples(see figure 36, first row from the bottom). In equations 28 and 29 for S_1 the measured value of the S-parameter of the first layer of samples Nr. 5 and Nr. 6 and for S_Q the measured S-parameter of the blank quartz tissue reference sample is inserted. The S-parameter of the carbon nanoparticles reference sample is chosen to represent the bulk value of the S-parameter of the carbon nanoparticles (S_C). Due to the large diameter of the particles within the sample, surface contributions can be neglected.

All in all, the known parameters of equations 28 and 29 for samples Nr. 5 and Nr. 6 are S_1, S_Q, S_C, p and α. A value for S_{NP} is calculated by formula 28. In the next step a value for $S_{surface}$ can be calculated using equation 29. Knowing the

Table 3: Results of the fit using the VEPFIT program
L$_+$...positron diffusion length, t [min]...duration of the carbon deposition, d [nm]...diameter of the carbon NP's, S$_1$...S-parameter of the first layer, S$_{NP}$...S-parameter of the nanoparticles, p...carbon concentration, ρ_1 [gcm^{-3}]...density first layer, α...probability of e$^+$ annihilation in the bulk, t$_1$ [µm]...thickness of the first layer

	L$_+$ [nm]	S-parameter					
Quartz tissue, S$_Q$		0.534					
Amorphous C, S$_C$	5	0.504					
NP surface, S$_{surface}$		0.553					

sample nr.	t [min]	d [nm]	S$_1$	S$_{NP}$	p [%]	ρ_1 [gcm^{-3}]	α	t$_1$ [µm]
1	5	55	0.520(1)	0.508(2)	0.54(5)	1.03(8)	0.91(2)	0.15(1)
2	15	55	0.515(1)	0.508(2)	0.73(5)	1.34(8)	0.91(2)	0.36(1)
3	5	80	0.513(1)	0.507(2)	0.78(5)	1.43(8)	0.94(2)	0.40(1)
4	15	80	0.511(1)	0.507(2)	0.84(5)	1.53(8)	0.94(2)	1.30(5)
5	4	120	0.509(1)	0.506(2)	0.90(5)	1.63(8)	0.96(2)	1.10(5)
6	1	120	0.509(1)	0.506(2)	0.90(5)	1.63(8)	0.96(2)	0.38(1)
7	7	41	0.525(1)	0.510(2)	0.37(5)	0.74(8)	0.88(2)	0.12(1)

parameters S$_Q$, S$_{surface}$, S$_C$ and α, as well as the measured values of S$_1$ for the other samples, the values for the carbon concentration p in the quartz tissue can be calculated from equation 28 for samples Nr. 1, 2, 3, 4, 7.

Finally the density of the first layer can be calculated by:

$$\rho_1 = p\rho_C + (1 - p)\rho_Q \tag{31}$$

For the following results the density of the carbon nanoparticles ρ_C was considered to be 1.8 gcm^{-3} and the density of the quartz tissue ρ_Q=134 mgcm^{-3}.

The values for the thickness t$_1$ (last column of table 3) of the first layer of quartz tissue infiltrated with carbon nanoparticles are estimated by the program VEPFIT. For these calculations only the region of quartz tissue highly infiltrated with carbon at low positron implantation energies (corresponding to the first plateau in figure 41) are taken into account. The software uses a best-fit procedure based on the solution of the diffusion equation in each layer of the heterostructure, taking into account the energy dependent positron implantation profiles. The free parameters of the model for each analyzed layer include the S-parameter value, the positron diffusion length and the layer density. The continuous curves through the datapoints in figures 41, 42 and 43 represent the results of a best-fit procedure obtained by VEPFIT. The fitting functions were calculated giving the program the

information of 2 exisiting layers in the sample: a first layer highly infiltrated with carbon nanoparticles and the quartz tissue.

Figures 45 and 46 show the qualitiative behaviour of the density and thickness of the first layer for similar deposition times and different nanoparticel diameters, for samples Nr. 1, 3, 5 and 7. It is clear that the thickness as well as the density show an important dependency on the nanoparticle diameter.

Figure 45: Qualitative behaviour of the thickness of the first layer as a function of the nanoparticle (NP) diameter for similar deposition times (samples Nr. 1,3,5 and 7). The doted lines are only a visual guide.
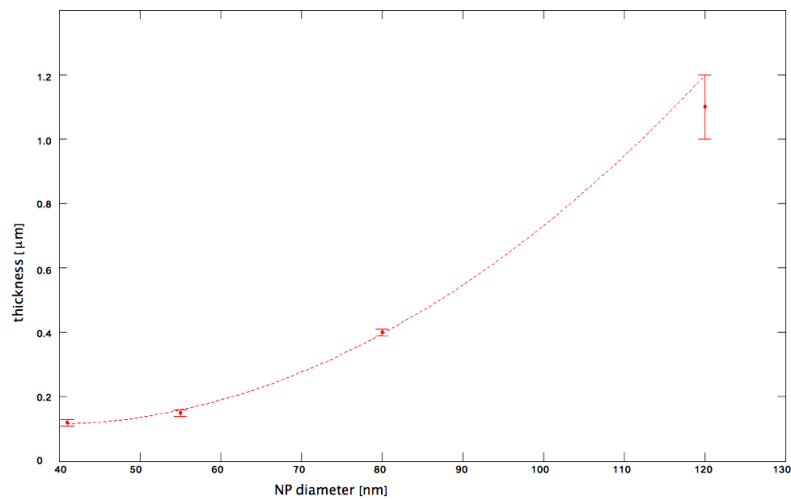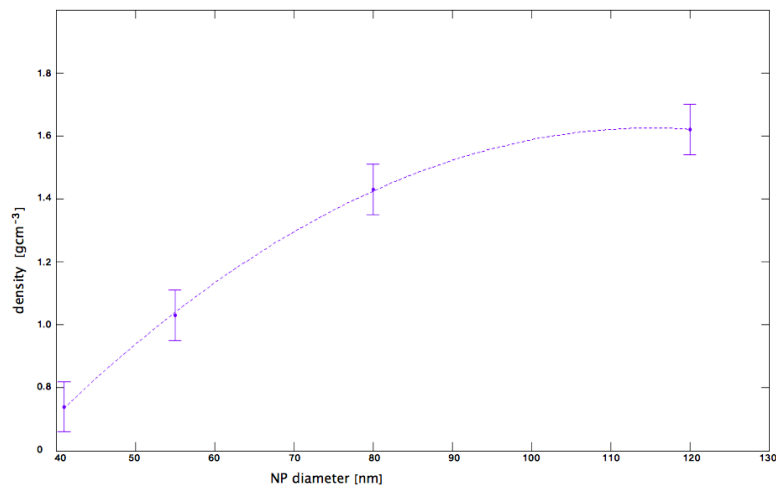

Figure 46: Qualitative behaviour of the density of the first layer as a function of the nanoparticle (NP) diameter for similar deposition times (samples Nr. 1,3,5 and 7). The doted lines are only a visual guide.

Modeling an interface layer

Within the VEPFIT model it is possible to introduce a second infiltrated layer, i.e. the whole sample is now assumed to be composed of three layers: A first layer highly infiltrated with carbon nanoparticles, a second interface layer and the blank quartz tissue. The first layer corresponds to the first plateau in figure 41 and the second, interface layer to the transition region between the two plateaus.

For the modeling of an interface layer, additional assumptions have to be made. Indeed, there is a direct connection between the density and the thickness of the interface layer. To estimate the thickness t_2, it is necessary to make an estimation about the mass density ρ_2, as described in the following. It is important to note that the introduction of a second layer does not change the characteristics of the first layer. Thus the data of table 3 remains practically unaltered within the experimental error presented there.

In order to gain more information about the second layer, the weight of the samples is measured, using a high precision balance. The mass of the filter tissue without carbon is determined and a density estimation is performed. The calculated density is nearly 16% higher than the density value provided by the company producing the filters. A possible explanation for this difference could be that the weighted mass is affected by the absorption of humidity, since SiO_2 is intrinsically hydrophilic. For this reason, all samples were heated in a furnace at 200°C for 30 minutes to evaporate the water. In all cases this procedure reduced the mass only by 1%. Other reasons for this discrepancy could be a further contamination of the filter (carbon particles in air etc.) or an unintentional variation or not reproducibility of the filter properties.

Table 4: Measured values for the mass and radius of the infiltrated zone
     t [min]...duration of the carbon deposition, d[nm]...diameter of the carbon NP's,
     m[g]...mass of the sample, Δm [mg]...mass difference blank sample/ carbon sample, R
     [cm]...radius of the infiltrated zone

Sample Nr.	t [min]	d [nm]	m [g]	Δm [mg]	R [cm]
Quartz	-	-	0.1156(1)	0	-
1	5	55	0.1225(1)	6.9(2)	2.10(5)
2	15	55	-	-	2.10(5)
3	5	80	0.1240(1)	8.4(2)	2.15(5)
4	15	80	0.1246(1)	9.0(2)	2.15(5)
5	4	120	0.1220(1)	6.4(2)	2.15(5)
6	1	120	0.1209(1)	5.3(2)	1.80(5)
7	7	41	0.1215(1)	5.9(2)	2.05(5)

Table 4 shows the mass and the difference in mass between the infiltrated samples and the pure quartz tissue (Δm). To use the mass data for further calculations, following assumptions have to be made:

The mass values of all blank filters before deposition are equal (within the experimental error of the measurement). Additionally, the eventual water adsorption and contamination is the same in all filters. Only in this case, Δm represents the carbon addition during infiltration. In order to make this more clear, the mass of the filters could be measured before and after carbon deposition in controlled conditions, where contamination is avoided.

Sample Nr. 2 could not be measured because the tissue got damaged during its removal from the sample holder after a positron annihilation spectroscopy measurement, which affected its weight.

By a comparison of samples Nr. 3 & Nr. 4 and Nr. 5 & Nr. 6, it can be concluded that there is no linear correlation between the growth time and the mass difference Δm. The carbon was not infiltrated linearly with the time exposed at the aerosol.

For a further analysis, the density of the first layer ρ_1 is fixed, according to the previous results (see table 3). The thickness of the two layers (t_1,t_2) and the density of the second layer (ρ_2) are estimated. By an iterative procedure the best

Table 5: Results of the fit for the introduction of a second layer using the VEPFIT program t [min]...duration of the carbon deposition, d[nm]...diameter of the carbon NP's, $\Delta m/A$ [mgcm^{-2}]...areal density, ρ_1 [gcm^{-3}]...density first layer, ρ_2 [gcm^{-3}]...density second layer

sample nr.	t [min]	d [nm]	$\Delta m/A$ [mg cm^{-2}]	ρ_1 [gcm^{-3}]	ρ_2 [gcm^{-3}]	t_1 [μm]	t_2 [μm]
1	5	55	0.50(3)	1.0(1)	1.2(3)	0.15(1)	4(1)
2	15	55	-	1.3(1)	-	0.36(1)	-	-
3	5	80	0.58(3)	1.4(1)	0.9(2)	0.40(1)	6(1)
4	15	80	0.62(3)	1.5(1)	1.1(3)	1.30(5)	4(1)
5	4	120	0.44(3)	1.6(1)	0.9(3)	1.10(5)	3(1)
6	1	120	0.52(3)	1.6(1)	1.5(3)	0.38(1)	3(1)
7	7	41	0.45(3)	0.7(1)	1.5(3)	0.12(1)	3(1)

fit is obtained: An initial value for ρ_2 is set, t_1 and t_2 are found as fit results of the two-layer-fit and then ρ_2 is set according to the following boundary condition:

$$\frac{\Delta m}{A} \approx \rho_1 t_1 + \rho_2 t_2 \tag{32}$$

The procedure ends when the convergence is reached.

In table 5 the results of the best fits are summarized. The thickness of the first layer has a wide range from 0.12 μm to 1.3 μm, which is accurately determined by the fitting procedure. In general, it can be seen that the thickness of the first layer t_1 increases with the time of the deposition. For samples Nr. 3 and Nr. 4, with deposition times of 5 minutes and 15 minutes, it is 0.4(1) μm and 1.30(5) μm.

Compared to t_1 the error for the thickness of the second layer is two orders of magnitude higher. The reason for this result is that the positrons seem to be very sensitive to the first layer and to the quartz tissue (plateaus at lower and higher energies) but not to the second layer. Information regarding the second layer could be found in the transition region between the two plateaus. The thickness of the second layer t_2 can be derived from the s-shaped region of the S vs. positron implantation energy-curve. Even if the error for t_2 is considered, the data shows a second layer thicker than the first layer for all samples. Taking into account the error for ρ_2, the density of the second layer is smaller than the density of the first layer, except for the two cases with smallest nanoparticles (Samples Nr. 1 and 7). The reason is probably that these smallest nanoparticles have a higher capability of penetrating inside the quartz tissue.

Figures 47 and 48 give a summary of the main results of table 5. They show the density as a function of the thickness of the layer for all samples.

Also in this case, to get more precise values on the thickness and density of the second infiltrated layer, a coincidence measurement with higher statistics should be considered. As already mentioned for the previous set of samples (microstructured nickel filter), the results obtained by VEPFIT are strongly dependent on the information given for the samples. In both cases the exact densities of the carbon layers are unknown and have to be estimated. Also the values for the deposited mass of carbon, used as input parameters for the program, are based on assumptions. If these parameters could be given more precisely in the forefront, the analysis of the interfacial region could be a lot less complex, it would be possible to gather more information about it and the quality of the results could be improved.
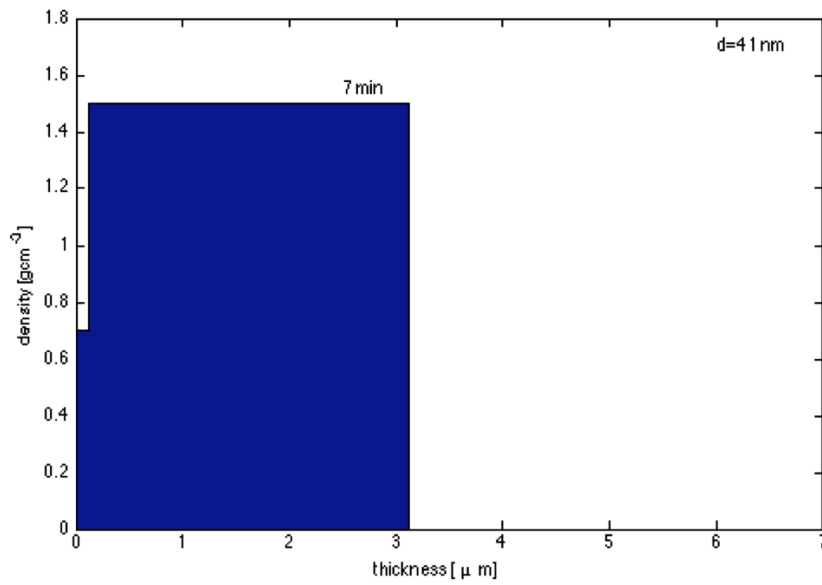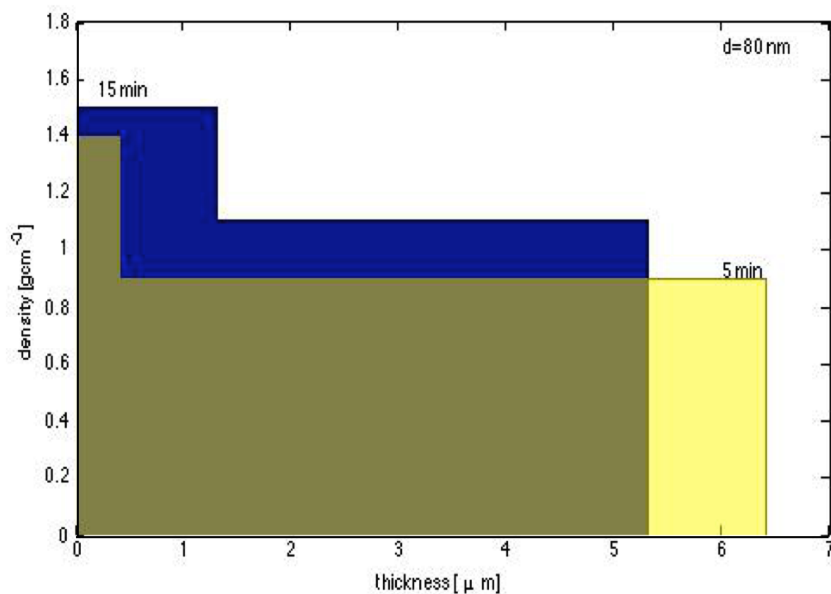
(a) Nr. 7
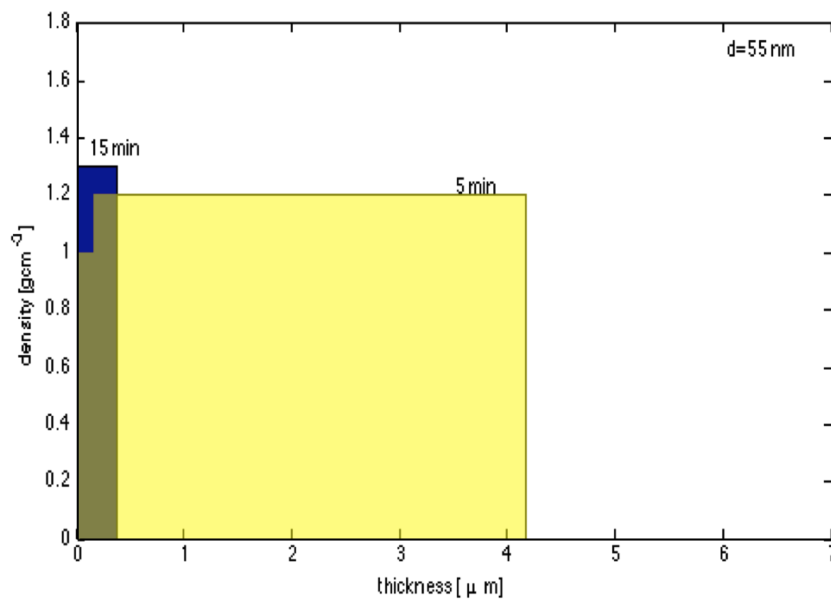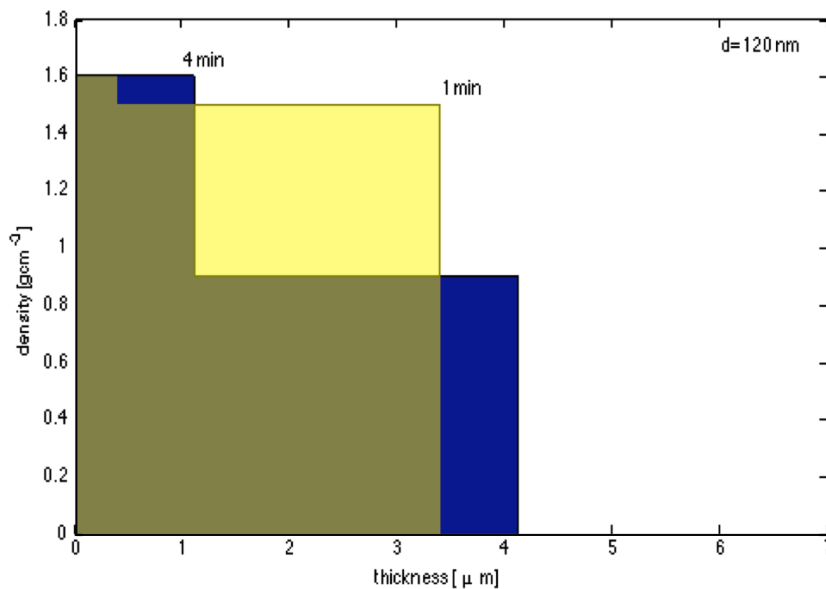

(b) Nr. 1 & Nr. 2

Figure 47: Density profiles for samples Nr. 1, 2 & 7 according to table 5 for carbon nanoparticle size of d=41 nm (a) and d=55 nm (b)

(a) Nr. 3 & Nr. 4

(b) Nr. 5 & Nr. 6

Figure 48: Density profiles for samples Nr. 3, 4, 5 & 6 according to table 5 for carbon nanoparticle size of d=80 nm (a) and d=120 nm (b)

SUMMARY

SUMMARY

4.1 AEḡIS EXPERIMENT: PS FORMATION AND LASER EXCITATION OF PS

4.1.1 *Positron transport to the test chamber & Ps formation*

The positron beam spot in the test chamber has been characterized by implanting it onto the MCP and phosphor screen assembly. The diameter of the area at FWHM of the spot was found to be 3.3 mm. An image of it as well as a 3D map of the beam intensity can be seen in figures 23 and 24.

4.1.2 *Positronium formation*

The suitability of channel-porous p-Si(111) for Ps formation could be demonstrated using lifetime spectroscopy (see figure 25). From the data, the positronium lifetime could be calculated to (142.8 ± 1.0) ns.

4.1.3 *Laser excitation of positronium to n=3*

Efficient excitation of o-Ps to the n=3 level in vacuum has been demonstrated. For the production and detection of positronium, a pulsed slow positron beam and single shot positronium annihilation lifetime spectroscopy was used. The laser excitation of n=3 at 205 nm was monitored by magnetic quenching and photoionization.

4.1.3.1 *Magnetic quenching*

In the case of magnetic quenching at a field of 250 G, the fraction of excited positronium was measured to S=(3.6 ± 1.2)%. This is a small signal, not clearly visible in the corresponding SSPALS spectra (see figure 27) at first sight. Anyhow, excitation could be verified by the good statistics of the measurement. In order to generate higher fractions of excited o-Ps, one could think of increasing the strength of the magnetic field. However, this is no solution, because higher magnetic fields lead to quenching of the ground state o-Ps. The S-parameter would

increase but not due to a higher detection efficiency of excited Ps, but because of an additional signal created by the quenched ground state positronium. To improve the detection ability a different technique, like selective photoionization, was applied as summarized next.

4.1.3.2 *Photoionization*

In addition to the UV-laser and the magnetic field, an IR-pulse was applied to depopulate the excited o-Ps. The corresponding S-parameter is S=(15.5±1.3)%. This signal is more than four times bigger than for magnetic quenching only. The reason for a bigger signal in this case is not a larger fraction of excited o-Ps, but a more efficient depopulation of the excited states.

4.1.3.3 *Linewidth of the 1^3S-3^3P Ps excitation*

The UV-wavelength was varied and the corresponding SSPALS spectra were measured to obtain the linewidth of the transition to n=3. Figure 32 shows the S-parameter as a function of the wavelength. It results in the expected Doppler broadened linewidth. The resonance wavelength was found to be (205.049±0.002) nm. From a Gaussian fit of the peak the o-Ps velocity parallel to the surface of the target could be estimated to $\bar{v}_x \approx 10^5$m/sec. The corresponding positronium temperature is (1150±150) K.

4.1.3.4 *Excitation to Rydberg states*

Setting the wavelength of the IR-laser to 1708.54 nm, the excitation of Ps to n=15 was measured. The S-parameter for this transition was found to be S=(17.8±2.0) nm. To measure also the transitions to n=16 and n=17 the IR-wavelength was varied between 1684 nm and 1708 nm. Figure 34 shows the S-parameter as function of the wavelength. The n=15 and the n=16 transition are clearly distinguishable, while the excitaion to n=17 is only vaguely recognizable.

4.2 VEPAS LABORATORY COMO: POSITRON ANNIHILATION SPECTROSCOPY OF NANOCARBON PARTICLE FILTERS

4.2.1 *Nickel filter*

The first set of samples, a pure microstructured nickel filter and the same filter with an additional layer of carbon nanoparticles, was investigated using Doppler broadening and positronium formation spectroscopy. To gather some information before the measurements, the mean positron implantation depths for amorphous carbon and porous nickel were calculated from the corresponding Makhov profiles for various positron implantation energies. As expected, the calculation showed, that positrons get implanted deeper into the amorphous carbon layer due to its lower density.

4.2.1.1 *Doppler broadening spectroscopy*

The Doppler broadening of the positron annihilation line was measured for positron implantation energies varied between 0.1 keV and 17.1 keV. For each energy the S-parameter, corresponding to the central area beneath the annihilation peak, was calculated. In figure 39 the datapoints as a function of the positron implantation energy are depicted for both samples. By the use of the program VEPFIT, the obtained values were fitted and the positron diffusion length in the nickel filter and the carbon could be obtained to $L_{pos,Ni}$=(170±2) nm and $L_{pos,C}$=(44±2) nm. Furthermore the thickness of the carbon layer has been estimated to t_C=(620±2) nm. The fit was done, assuming that there is a third layer consisting of the interface region between carbon and nickel. In fact, to verify the existence of an interface the statistics of the measurement is not high enough. Indeed the 3-layer fit showed the lowest statistical deviation, however, the errors of other fits using two layers were not significantly higher.

4.2.1.2 *Positronium formation spectroscopy*

The positronium formation for both samples in the energy range between 0.1 keV and 17.1 keV was measured. The $F_{3\gamma}$-fraction as a function of the positron implantation depth can be seen in figure 40. Both samples showed insignificant values of positronium formation. The maximum value of the $F_{3\gamma}$-fraction for the nickel filter was measured to be 0.06%, while the maximum for the nickel-carbon

sample was only 0.02%. It is noticeable, that even for high positron implantation energies and consequently in deep layers of the sample, the $F_{3\gamma}$-fraction for the nickel sample is consistently higher than for the nickel-carbon sample. This seems to be an indication of carbon nanoparticles diffusing deeply into the sample, approximately 450 nm.

4.2.2 *Quartz tissue filter*

Analyzed were eight quartz tissue filter samples with carbon layers on top, each differing in particle size and deposition time of the carbon nanoparticles. Additionally a blank filter and a carbon nanoparticle sample were measured as a reference. All samples were analyzed by the means of Doppler broadening spectroscopy and further interpreted using VEPFIT. Figure 41 shows the S-parameter as a function of the positron implantation depth for all samples. The data clearly indicates the existence of two different environments where the positrons annihilate: A layer of tissue highly infiltrated with carbon at lower implantation energies, and a layer dominated by quartz tissue, free from carbon, at higher implantation energies. By comparing samples of similar particle size and different deposition times, it could be shown that the width of the first layer increases with the duration of the carbon deposition. Further the S-parameter was found to be dependent on the size of the carbon particles and the deposition time. Based on a model and the fits obtained by VEPFIT, the density and thickness of the first layer was calculated for each sample. The results can be found in table 3. A second layer has been introduced to the VEPFIT and its thickness and density have been calculated. These results can be found in table 5.

4.3   FUTURE OUTLOOK

The results presented in this thesis have shown that an efficient excitation of positronium to n=3 and a further excitation to Rydberg states is possible in the present set-up. For a successful performance of the next planned steps towards the formation of cold antihydrogen, it will be inevitable to lower the temperature of the produced positronium.

An additional benefit of colder Ps is that it should enable the laser excitation of a larger fraction.

For this reason, the focus of the next measurements will lie on the reduction of the Ps temperature and the study of the Ps energy distribution.

The laser excitation measurements to n=3 will be repeated at higher positron implantation energies, up to 6 keV, to create colder positronium at the target. From the Doppler broadening of the excitation line, the Ps velocity at different positron implantation energies will be deduced.

Another strategy to achieve colder Ps is to cool down the target. In the course of this thesis, a cryostat has been installed to the test chamber. In the following months measurements of the Ps energy with varied target temperatures will be conducted.

Another important factor for the improvement of the laser excitation efficiency is to optimize the temporal and spatial overlap of the laser pulse and the Ps cloud. Thus, it will be necessary, to gain more insight into the Ps velocity distribution. So far, the laser pulse proceeds in parallel to the sample surface and only the Ps velocity in this direction could be concluded. To get to know the energy distributions also in other directions, the laser pulse will be applied not only parallel but also perpendicular and anti-parallel to the target surface.

In addition to the abovementioned optimizations of conducted experiments, some further positronium spectroscopy measurements are scheduled. It is planned to create the metastable n=2 Ps-state via n=3 as an intermediate step, and to test laser-cooling on it. This would not only be the first time to produce the Ps n=2 state in this way, but also the first demonstration of Ps laser-cooling. Since only a fraction of approximately 10% of n=3 Ps undergoes the transition to n=2, it

is necessary to optimize excitation to n=3 in the forefront. Additionally a new positron source will be installed to increase the statistics of the measurement.

Concerning the analysis of the carbon particle filters at the VEPAS laboratory of Como, it would be essential to know more characteristics of the samples to prove the results of the first measurements. Also conceivable would be more detailed measurements with higher statistics of certain areas of the sample, as well as measurements of additional samples, as for example samples made exclusively from deposited carbon.

[1] DIRAC, P.A.M.: The quantum theory of the electron. In: *Proceedings of the Royal Society of London* (1928), Nr. 778, -. http://rspa.royalsocietypublishing.org/content/royprsa/117/778/610.full.pdf

[2] ANDERSON, Carl D.: The apparent existence of easily deflectable positives. In: *Science* 76 (1932), Nr. 1967, S. 238–239. http://dx.doi.org/10.1126/science.76.1967.238. – DOI 10.1126/science.76.1967.238. – ISSN 0036–8075

[3] Confinement of antihydrogen for 1,000 seconds. In: *Nat Phys* 7 (2011), 07, Nr. 7, 558–564. http://dx.doi.org/10.1038/nphys2025. ISBN 1745–2473

[4] ULMER, S. ; SMORRA, C. ; MOOSER, A. ; FRANKE, K. ; NAGAHAMA, H. ; SCHNEIDER, G. ; HIGUCHI, T. ; VAN GORP, S. ; BLAUM, K. ; MATSUDA, Y. ; QUINT, W. ; WALZ, J. ; YAMAZAKI, Y.: High-precision comparison of the antiproton-to-proton charge-to-mass ratio. In: *Nature* 524 (2015), 08, Nr. 7564, 196–199. http://dx.doi.org/10.1038/nature14861. ISBN 0028–0836

[5] KUBICA, P. ; STEWART, A. T.: Thermalization of Positrons and Positronium. In: *Phys. Rev. Lett.* 34 (1975), Apr, S. 852–855. http://dx.doi.org/10.1103/PhysRevLett.34.852. – DOI 10.1103/PhysRevLett.34.852

[6] SCHULTZ, Peter J. ; LYNN, K. G.: Interaction of positron beams with surfaces, thin films, and interfaces. In: *Rev. Mod. Phys.* 60 (1988), Jul, S. 701–779. http://dx.doi.org/10.1103/RevModPhys.60.701. – DOI 10.1103/RevModPhys.60.701

[7] MACMAHON, TD ; BAERG, AP: The electron capture to positron branching ratio in the decay of 22Na. In: *Canadian Journal of Physics* 54 (1976), Nr. 14, S. 1433–1437

[8] GULLIKSON, E.M. ; JR., A.P. M.: Solid neon moderator for producing slow positrons. In: *Applied Physics Letters* 49 (1986), Nr. 17, –

[9] GULLIKSON, E. M. ; MILLS, A. P.: Positron Dynamics in Rare-Gas Solids. In: *Phys. Rev. Lett.* 57 (1986), Jul, S. 376–379. `http://dx.doi.org/10.1103/PhysRevLett.57.376`. – DOI 10.1103/PhysRevLett.57.376

[10] C.M. SURKO, M. L. ; PASSNER, A.: Positron plasma in the laboratory. In: *Physical Review Letters* 62 (1989), Nr. 8, S. 901–904. `http://dx.doi.org/http://dx.doi.org/10.1103/PhysRevLett.62.901`. – DOI http://dx.doi.org/10.1103/PhysRevLett.62.901

[11] SURKO, C.M. ; GREAVES, R.G.: Emerging science and technology of antimatter plasmas and trap-based beams. In: *Physics of Plasmas* 11 (2004), Nr. 5, 2333–2348

[12] MURPHY, T. J. ; SURKO, C. M.: Positron trapping in an electrostatic well by inelastic collisions with nitrogen molecules. In: *Phys. Rev. A* 46 (1992), Nov, S. 5696–5705. `http://dx.doi.org/10.1103/PhysRevA.46.5696`. – DOI 10.1103/PhysRevA.46.5696

[13] GREAVES, R. ; SURKO, C.: Positron trapping and the creation of high-quality trap-based positron beams. In: *Nucl. Instrum. Meth. B* 192 (2002), S. 90–96. `http://dx.doi.org/10.1016/S0168-583X(02)00717-6`. – DOI 10.1016/S0168–583X(02)00717–6

[14] NOTTE, J. ; FAJANS, J.: The effect of asymmetries on non-neutral plasma confinement time. In: *Physics of Plasmas* 1 (1994), Nr. 5, 1123–1127. `http://ist-socrates.berkeley.edu/~fajans/pub/pdffiles/EffectAsymConfinementTimePoP.PDF`

[15] CASSIDY, D.B.: Experiments with many-positron systems. In: *Physics with many positrons* 174 (2010), S. 1–75. `http://dx.doi.org/10.3254/978-1-60750-647-8-1`. – DOI 10.3254/978–1–60750–647–8–1

[16] CASSIDY, DB ; GREAVES, RG ; MELIGNE, VE ; MILLS JR, AP: Strong drive compression of a gas-cooled positron plasma. In: *Applied Physics Letters* 96 (2010), Nr. 10, S. 101502

[17] KNOLL, Glenn F.: *Radiation detection and measurement*. John Wiley & Sons, 2010

[18] MUKHOPADHYAY, Sanjoy: Plastic gamma sensors: an application in search of radioisotopes. In: *Optical Science and Technology, SPIE's 48th Annual Meeting* International Society for Optics and Photonics, 2004, S. 62–72

[19] PUSKA, Martti J. ; NIEMINEN, Risto M.: Theory of positrons in solids and on solid surfaces. In: *Reviews of modern Physics* 66 (1994), Nr. 3, S. 841

[20] VEHANEN, A. ; SAARINEN, K. ; HAUTOJÄRVI, P. ; HUOMO, H.: Profiling multilayer structures with monoenergetic positrons. In: *Phys. Rev. B* 35 (1987), Apr, S. 4606–4610. http://dx.doi.org/10.1103/PhysRevB.35.4606. – DOI 10.1103/PhysRevB.35.4606

[21] KRAUSE-REHBERG, Reinhard ; LEIPNER, Hartmut S.: *Positron annihilation in semiconductors: defect studies*. Bd. 127. Springer Science & Business Media, 1999

[22] MARIAZZI, S.: *Application of Positron Spectroscopy for defect Characterization*, University of Trento, Diss., 2012

[23] WEISS, AH ; COLEMAN, PG ; COLEMAN, PG: Positron Beams and Their Applications. In: *World Scientific: Amsterdam* 129 (2000)

[24] MADSEN, L. B. ; LAMBROPOULOS, P.: Scaling of hydrogenic atoms and ions interacting with laser fields: Positronium in a laser field. In: *Phys. Rev. A* 59 (1999), Jun, S. 4574–4579. http://dx.doi.org/10.1103/PhysRevA.59.4574. – DOI 10.1103/PhysRevA.59.4574

[25] RICH, Arthur: Recent experimental advances in positronium research. In: *Rev. Mod. Phys.* 53 (1981), Jan, S. 127–165. http://dx.doi.org/10.1103/RevModPhys.53.127. – DOI 10.1103/RevModPhys.53.127

[26] RIENÄCKER, Benjamin: Investigation of positron-positronium converter targets at AEgIS, Master Thesis at University of Applied Sciences Munich. (2015)

[27] DELLER, A. ; ALONSO, A. M. ; COOPER, B. S. ; HOGAN, S. D. ; CASSIDY, D. B.: Measurement of Rydberg positronium fluorescence lifetimes. In: *Phys. Rev. A*

93 (2016), Jun, S. 062513. `http://dx.doi.org/10.1103/PhysRevA.93.062513`. – DOI 10.1103/PhysRevA.93.062513

[28] CASSIDY, DB ; BROMLEY, M W. ; COTA, LC ; HISAKADO, TH ; TOM, HWK ; MILLS JR, AP: Cavity induced shift and narrowing of the positronium Lyman-α transition. In: *Physical review letters* 106 (2011), Nr. 2, S. 023401

[29] CASSIDY, DB ; HISAKADO, TH ; TOM, HWK ; MILLS JR, AP: Efficient production of Rydberg positronium. In: *Physical review letters* 108 (2012), Nr. 4, S. 043401

[30] CASTELLI, F ; GIAMMARCHI, MG: Laser-driven Positronium excitation in the AEGIS antimatter experiment at CERN, Societa Italiana di Fisica. (2009)

[31] CASTELLI, F. ; BOSCOLO, I. ; CIALDI, S. ; GIAMMARCHI, M. G. ; COMPARAT, D.: Efficient positronium laser excitation for antihydrogen production in a magnetic field. In: *Phys. Rev. A* 78 (2008), Nov, 052512. `http://link.aps.org/doi/10.1103/PhysRevA.78.052512`

[32] CARAVITA, Ruggero: *Laser apparatus for exciting Positronium in AEGIS Positronium spectroscopy experiment*, Diploma Thesis at University of Pavia, Diss., 2011

[33] TUOMISTO, Filip ; MAKKONEN, Ilja: Defect identification in semiconductors with positron annihilation: experiment and theory. In: *Reviews of Modern Physics* 85 (2013), Nr. 4, S. 1583

[34] THRÄNERT, Stefan: *Charakterisierung mikro-und mesoporöser Gläser mit Hilfe der ortho-Positronium Lebensdauer-Spektroskopie*, Dissertation, Universität Halle, Diss., 2008

[35] CASSIDY, D. B. ; DENG, S. H. M. ; TANAKA, H. K. M. ; MILLS, A. P.: Single shot positron annihilation lifetime spectroscopy. In: *Applied Physics Letters* 88 (2006), Nr. 19. `http://dx.doi.org/http://dx.doi.org/10.1063/1.2203336"`. – DOI http://dx.doi.org/10.1063/1.2203336"

[36] DUPASQUIER, Alfredo ; MILLS JR, AP: *Positron spectroscopy of solids*. Bd. 125. IOS Press, 1995

[37] Asoka-Kumar, P. ; Alatalo, M. ; Ghosh, V. J. ; Kruseman, A. C. ; Nielsen, B. ; Lynn, K. G.: Increased Elemental Specificity of Positron Annihilation Spectra. In: *Phys. Rev. Lett.* 77 (1996), Sep, S. 2097–2100. `http://dx.doi.org/10.1103/PhysRevLett.77.2097`. – DOI 10.1103/PhysRevLett.77.2097

[38] Lynn, KG ; Welch, DO: Slow positrons in metal single crystals. I. Positronium formation at Ag (100), Ag (111), and Cu (111) surfaces. In: *Physical Review B* 22 (1980), Nr. 1, S. 99

[39] Wesson, Paul S.: *Five-dimensional physics: classical and quantum consequences of Kaluza-Klein cosmology.* World Scientific, 2006

[40] Lightman, Alan P. ; Lee, David L.: Restricted proof that the weak equivalence principle implies the Einstein equivalence principle. In: *Physical Review D* 8 (1973), Nr. 2, S. 364

[41] Galilei, G: *1638 Discorsi Intorno a due Nuove Scienze (Leiden).* 1914

[42] Will, Clifford M.: *Theory and experiment in gravitational physics.* Cambridge University Press, 1993

[43] Kellerbauer, A ; Amoretti, M ; Belov, AS ; Bonomi, G ; Boscolo, I ; Brusa, RS ; Büchner, Matthias ; Byakov, VM ; Cabaret, L ; Canali, C u. a.: Proposed antimatter gravity measurement with an antihydrogen beam. In: *Nuclear Instruments and Methods in Physics Research Section B: Beam Interactions with Materials and Atoms* 266 (2008), Nr. 3, S. 351–356

[44] Aghion, Stefano ; Amsler, C ; Ariga, A ; Ariga, T ; Belov, AS ; Bonomi, G ; Bräunig, P ; Bremer, J ; Brusa, RS ; Cabaret, L u. a.: Positron bunching and electrostatic transport system for the production and emission of dense positronium clouds into vacuum. In: *Nuclear Instruments and Methods in Physics Research Section B: Beam Interactions with Materials and Atoms* 362 (2015), S. 86–92

[45] Drobychev, G Y. ; Gendotti, U ; Boscolo, I ; Walters, H ; Büchner, M ; Rubbia, André ; Oberthaler, MK ; Nédélec, P ; Zavatarelli, S ; Carraro,

C u. a.: Proposal for the AEGIS experiment at the CERN antiproton decelerator (Antimatter Experiment: Gravity, Interferometry, Spectroscopy). 2007. – Forschungsbericht

[46] JERNELV, Ine L.: Optimisation of Positron-Positronium Conversion and Positronium Laser Excitation, Master Thesis at Norwegian University of Science and Technology (NTNU). (2015)

[47] MARIAZZI, S ; BETTOTTI, P ; LARCHERI, S ; TONIUTTI, L ; BRUSA, RS: High positronium yield and emission into the vacuum from oxidized tunable nanochannels in silicon. In: *Physical Review B* 81 (2010), Nr. 23, S. 235418

[48] NAGASHIMA, Y ; MORINAKA, Y ; KURIHARA, T ; NAGAI, Y ; HYODO, T ; SHIDARA, T ; NAKAHARA, K: Origins of positronium emitted from SiO 2. In: *Physical Review B* 58 (1998), Nr. 19, S. 12676

[49] MARIAZZI, Sebastiano ; BETTOTTI, Paolo ; BRUSA, Roberto S.: Positronium cooling and emission in vacuum from nanochannels at cryogenic temperature. In: *Physical review letters* 104 (2010), Nr. 24, S. 243401

[50] AGHION, S. ; AMSLER, C. ; ARIGA, A. ; ARIGA, T. ; BONOMI, G. ; BRÄUNIG, P. ; BREMER, J. ; BRUSA, R. S. ; CABARET, L. ; CACCIA, M. ; CARAVITA, R. ; CASTELLI, F. ; CERCHIARI, G. ; CHLOUBA, K. ; CIALDI, S. ; COMPARAT, D. ; CONSOLATI, G. ; DEMETRIO, A. ; DI NOTO, L. ; DOSER, M. ; DUDAREV, A. ; EREDITATO, A. ; EVANS, C. ; FERRAGUT, R. ; FESEL, J. ; FONTANA, A. ; FORSLUND, O. K. ; GERBER, S. ; GIAMMARCHI, M. ; GLIGOROVA, A. ; GNINENKO, S. ; GUATIERI, F. ; HAIDER, S. ; HOLMESTAD, H. ; HUSE, T. ; JERNELV, I. L. ; JORDAN, E. ; KELLERBAUER, A. ; KIMURA, M. ; KOETTIG, T. ; KRASNICKY, D. ; LAGOMARSINO, V. ; LANSONNEUR, P. ; LEBRUN, P. ; LEHNER, S. ; LIBERADZKA, J. ; MALBRUNOT, C. ; MARIAZZI, S. ; MARX, L. ; MATVEEV, V. ; MAZZOTTA, Z. ; NEBBIA, G. ; NEDELEC, P. ; OBERTHALER, M. ; PACIFICO, N. ; PAGANO, D. ; PENASA, L. ; PETRACEK, V. ; PISTILLO, C. ; PRELZ, F. ; PREVEDELLI, M. ; RAVELLI, L. ; RESCH, L. ; RIENÄCKER, B. ; RØHNE, O. M. ; ROTONDI, A. ; SACERDOTI, M. ; SANDAKER, H. ; SANTORO, R. ; SCAMPOLI, P. ; SMESTAD, L. ; SORRENTINO, F. ; SPACEK, M. ; STOREY, J. ; STROJEK, I. M. ; TESTERA, G. ; TIETJE, I. ; VAMOSI, S. ; WIDMANN, E. ; YZOMBARD, P. ; ZMESKAL, J. ; ZURLO, N.: Laser excitation of the $n = 3$

level of positronium for antihydrogen production. In: *Phys. Rev. A* 94 (2016), Jul, S. 012507. `http://dx.doi.org/10.1103/PhysRevA.94.012507`. – DOI 10.1103/PhysRevA.94.012507

[51] VAN VEEN, A ; SCHUT, H ; DE VRIES, J ; HAKVOORT, RA ; IJPMA, MR: Analysis of positron profiling data by means of VEPFIT. In: *4th International workshop on: Slow-positron beam techniques for solids and surfaces* Bd. 218 AIP Publishing, 1991, S. 171–198

[52] EATOUGH, Delbert J. ; CUI, Wenxuan ; HULL, Jeffery ; FARBER, Robert J.: Fine particulate chemical composition and light extinction at Meadview, AZ. In: *Journal of the Air & Waste Management Association* 56 (2006), Nr. 12, S. 1694–1706

[53] CONSOLATI, Giovanni ; FERRAGUT, Rafael ; GALARNEAU, Anne ; DI RENZO, Francesco ; QUASSO, Fiorenza: Mesoporous materials for antihydrogen production. In: *Chem. Soc. Rev.* 42 (2013), S. 3821–3832. `http://dx.doi.org/10.1039/C2CS35454C`. – DOI 10.1039/C2CS35454C

[54] MARX, Lisa: Positronium production in porous materials for antihydrogen production, Master thesis at University of Technology, Graz. (2016)

[55] ČÍŽEK, J ; PROCHÁZKA, I ; CIESLAR, M ; STULIKOVA, I ; CHMELIK, F ; ISLAM-GALIEV, RK: Positron-Lifetime Investigation of Thermal Stability of Ultra-Fine Grained Nickel. In: *physica status solidi (a)* 191 (2002), Nr. 2, S. 391–408

[56] DRYZEK, J ; CZAPLA, A ; KUSIOR, E: Positron annihilation studies of the multilayer system. In: *Journal of Physics: Condensed Matter* 10 (1998), Nr. 48, S. 10827

[57] BRAUN, Tibor: *Nuclear and Radiation Chemical Approaches to Fullerene Science.* Bd. 1. Springer Science & Business Media, 2013

[58] MARIAZZI, S ; MACCHI, C ; KARWASZ, GP ; BRUSA, RS ; LAIDANI, N ; BARTALI, R ; GOTTARDI, G ; ANDERLE, M: Amorphous carbon thin films deposited on Si and PET: Study of interface states. In: *Acta Physica Polonica-Series A General Physics* 107 (2005), Nr. 5, S. 842–847